Lysosome-related organelles: an investigation into clinical disorders of endothelial cells and platelets

David Westmoreland

A thesis submitted to University College London for the degree of Doctor of Philosophy

MRC Laboratory for Molecular Cell Biology
University College London
Gower Street
London
WC1E 6BT

Declaration

I David Westmoreland, confirm that the work presented in this thesis is my own. Where information has been derived from other sources, I confirm that this has been indicated in the thesis.

December 2016

1 Abstract

Lysosome-related organelles (LROs) are a heterogeneous group of organelles that have important functions in a number of specialised cell types. LROs, despite their distinct features and morphology, have been grouped together due to the observation that they are simultaneously functionally perturbed by single mutations in a number of genetic disorders, yet as a group they are still poorly understood.

Firstly, it was investigated whether the genes that are important for the formation/maturation of other LROs can also affect Weibel-Palade bodies (WPBs) an endothelial LRO that is critical to haemostasis and inflammation. In the genetic disorder Hermansky Pudlak syndrome (HPS) a number of LROs are affected, but the effect of these mutations on WPBs is not yet established. It was investigated whether these genes are indeed important for the biogenesis and function of WPBs, potentially revealing a new aspect of the disease phenotype. siRNA ablation in human endothelial cells of genes identified as involved in LRO biogenesis proved to give inconclusive results as to their importance in WPB formation and function.

Secondly, the understanding of LRO-related genetic disorders would be aided by an improvement in diagnostics. The diagnosis of platelet storage disorders (PSDs) is currently limited to the observation of symptoms (e.g. a bleeding disorder or albinism) that are often shared with other, more common diseases. Most HPS patients are initially misdiagnosed and many see 4 to 6 specialists before being correctly identified. I investigated whether Super Resolution Microscopy, allowing images to be taken with a higher resolution than the diffraction limit (<200 nm), has the potential for improving the imaging of platelet granules and thereby the diagnosis and characterisation of LRO-related disorders. The use of structured illumination microscopy, coupled with

automated image analysis bioinformatics allowed for a highly efficient differentiation between control and patient platelets.

Table of Contents

List of Figures

List of Tables

List of Abbreviations

ARC – Arthrogryposis, Renal dysfunction and cholestasis

BEACH – Beige and Chediak Higashi

BLOC – Biogenesis of Lysosome Related Organelle Complex

BSA – Bovine Serum Albumin

CHS – Chediak-Higashi Syndrome

ELISA - Enzyme-linked immunosorbent assay

GFP – Green Fluorescent Protein

GPS – Grey Platelet Syndrome

HPS – Hermansky Pudlak Syndrome

KD - Knockdown

KO – Knockout

LTA – Light Transmission Aggregometry

LROs – Lysosome Related Organelles

LYST - Lysosomal trafficking regulator

MKs - Megakaryocytes

MVBs –Multi Vesicular Bodies

NBEAL2 - neuro beachin-like 2

PBS – Phosphate-buffered Saline

PSD – Platelet storage pool disorder

RT-PCR – Reverse Transcription Polymerase Chain Reaction

SIM – Structured-illumination Microscopy

SDS - Sodium dodecyl sulphate

SRM – Super Resolution Microscopy

TGN – Trans Golgi Network

vWD – von Willebrand's Disease

vWF – von Willebrand's Factor

WPBs – Weibel Palade Bodies

WT – Wild Type

2 Introduction

2.1 **Lysosome-related organelles**

Lysosomes are membrane-bound cytoplasmic organelles containing hydrolytic enzymes that are primarily involved in intracellular protein degradation (*1*). Lysosome-related organelles (LROs) are distinct types of cytoplasmic organelles, they are related to lysosomes, yet are functionally, morphologically and/or compositionally distinct both from lysosomes and from each other (Table 1). Whilst many properties of LROs are shared with lysosomes, LROs are defined by the fact that they perform specific functions unrelated to degradation.

What LROs have in common is that some, if not all, of their content is derived from the endosomal system (*2*) and all LROs progressively mature from precursors by acquiring specialised cargoes and generating a lumenal environment conducive to their function. Within their host cells, LROs can produce completely novel morphological features (Figure 1) such as the proteinacious tubules of Weibel-Palade bodies (WPBs) and the lipid swirls within lamellar bodies (*1*).

Figure 1 LRO Morphology

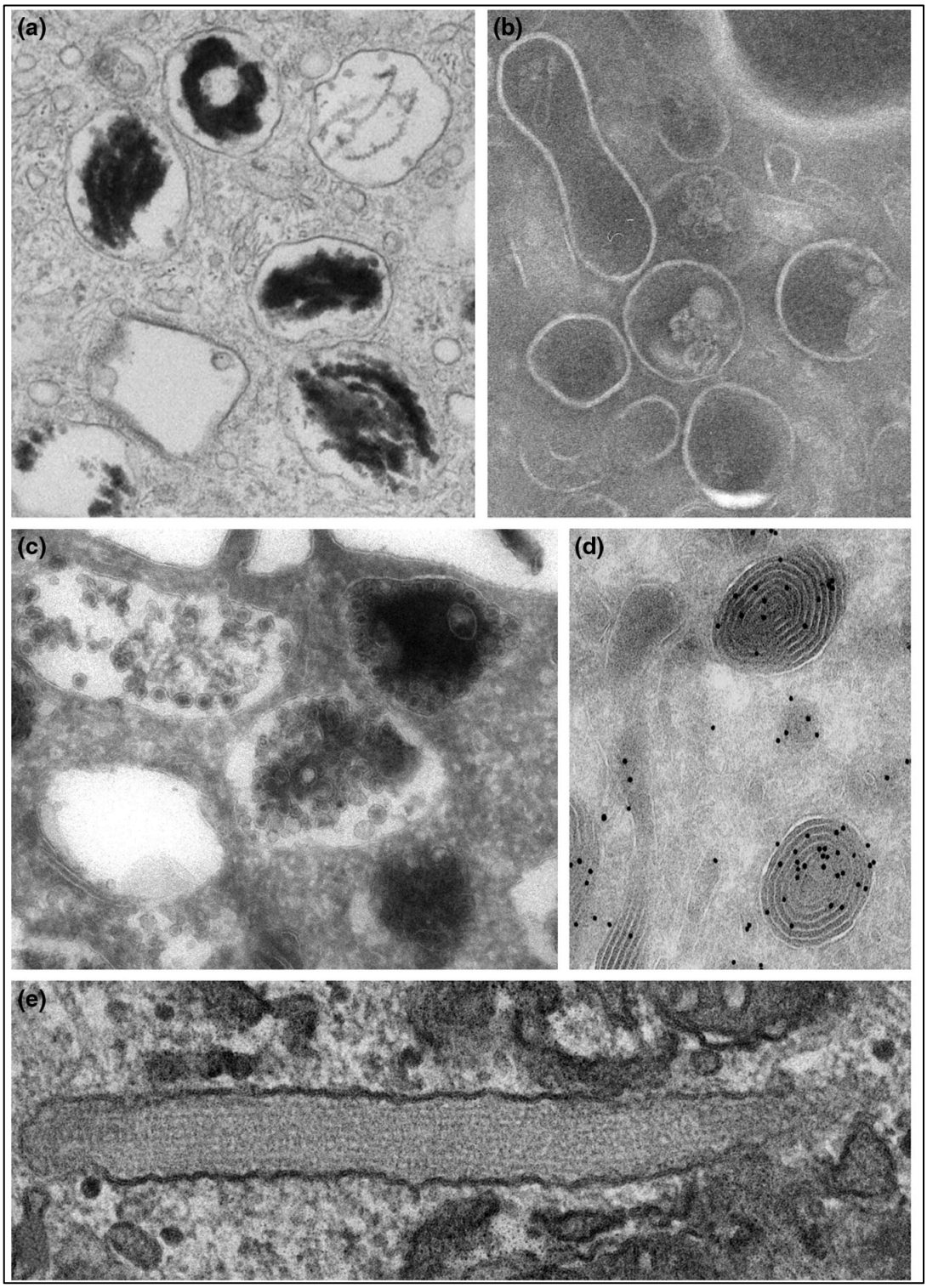

Despite their shared machinery and links to genetic disorders, LROs exhibit a variety of morphological features. (a) Melanosomes; (b) Azurophilic granules; (c) Cytolytic granules; (d) MHC class II compartments (here MIICs are immunogold labelled for MHC class II molecules) and (e) WPBs. Figure from (*2*)

Table 1 LRO Tissue Distribution and Physiological Function

Organelle	Tissue Distribution	Physiological function
Lytic Granules	Cytotoxic T lymphocytes, NK cells	Destruction of virally infected or cancerous target cells
Dense Granules (also known as dense bodies or delta granules)	Platelets, megakaryocytes	Release of ATP, ADP, serotonin and calcium for blood clotting
Alpha Granules	Platelets, megakaryocytes	Fibrinogen and von Willebrand factor release for platelet adhesion and blood clotting
Basophilic granules	Basophils, mast cells	Triggered release of histamines, other inflammatory stimuli
MHC class II compartments	Antigen presenting cells (dendritic cells, B lymphocytes, macrophages)	Processing and presentation of antigens to CD4+ lymphocytes for immune regulation
Lamellar Bodies	Lung epithelial type II cells	Storage and secretion of surfactant
Weibel Palade Bodies	Endothelial cells	Storage and regulated release of haemostatic and pro-inflammatory factors into blood
Melanosomes	Melanocytes, retinal and iris pigment epithelial cells	Intracellular melanin biosynthesis and storage and transfer to keratinocytes
Osteoclast Granules	Osteoclasts	Bone resorption and remodelling
Pigment Granules	*Drosophila melanogaster* eye cells	Eye Pigmentation
Acrosomes	Sperm Cells	Fertilisation, fusion of sperm and egg
Fat Storage Organelle	*Caenorhabditis elegans* gut cells	Fat Storage
Inhibitory Lysosomes	Dendritic cells	Control the pH of the phagosome

The cell types in which LROs are located in the human body and their functions within those tissues are displayed. Table adapted from (*2*)

Historically, research on LROs has been focused on their specialist functions as opposed to the similarities within this group as a whole. However, the observation that single mutations are capable of disrupting the biogenesis of many of these organelles simultaneously has sparked interest within the cell biology community. An example of this is shown by Hermansky Pudlak Syndrome (HPS), in which mutations that affect components of the cell's membrane trafficking machinery are capable of disrupting the function of a number of LROs (*3*). The characterisation of these organelles was facilitated by research on the coat-colour mutants of mice that were shown to exhibit the same cluster of pigment and bleeding disorders as their human counterparts (as well as with the *Drosophila melanogaster* eye colour variants and genetic studies in yeast) (*4*). These discoveries have emphasised the similarities between LROs, yet despite this, the molecular and cellular basis for the LROs relationship to lysosomes and their diversity still remain poorly understood.

Because the study of LROs has been historically allied with an interest in coat colour genetics (*5*), a major focus of research has been melanosomes; the LRO

found in the melanocytes of the eye and skin and pigmented epithelial cells of the retina (iris and ciliary body of the eye) in which melanin pigments are synthesised and stored. The pigments formed by melanosomes are the key determinant of skin and hair colour in mammals, as well as providing photo-protection against ionising radiation (*1*). Initially the research that focused on the melanosome not only drove "LROs" as an area of research (*6*) but also, after observations involving the whole group of LROs had been collected, these organelles became once again the reference and focal point for studies in this area (7). Much of what we know today about LROs has thus been due to efforts to further understand the mechanisms behind the biogenesis and maturation of the melanosome and they therefore provide a natural reference/start point for any LRO-related investigation.

2.2 Melanosomes

In a typical cell (and in melanocytes) the early endosomes (EE, Figure 2), consist of tubular domains and vacuolar domains. Intralumenal vesicles (ILVs) form from the vacuolar domains by membrane invagination in regions immediately adjacent to bilayered clathrin and Hrs-containing coats (black arrows, Figure 2). These vacuolar domains can mature to form late endosomal multi-vesicular bodies, the lumenal contents of which are degraded upon fusion with lysosomes.

Figure 2 Melanosome Biogenesis

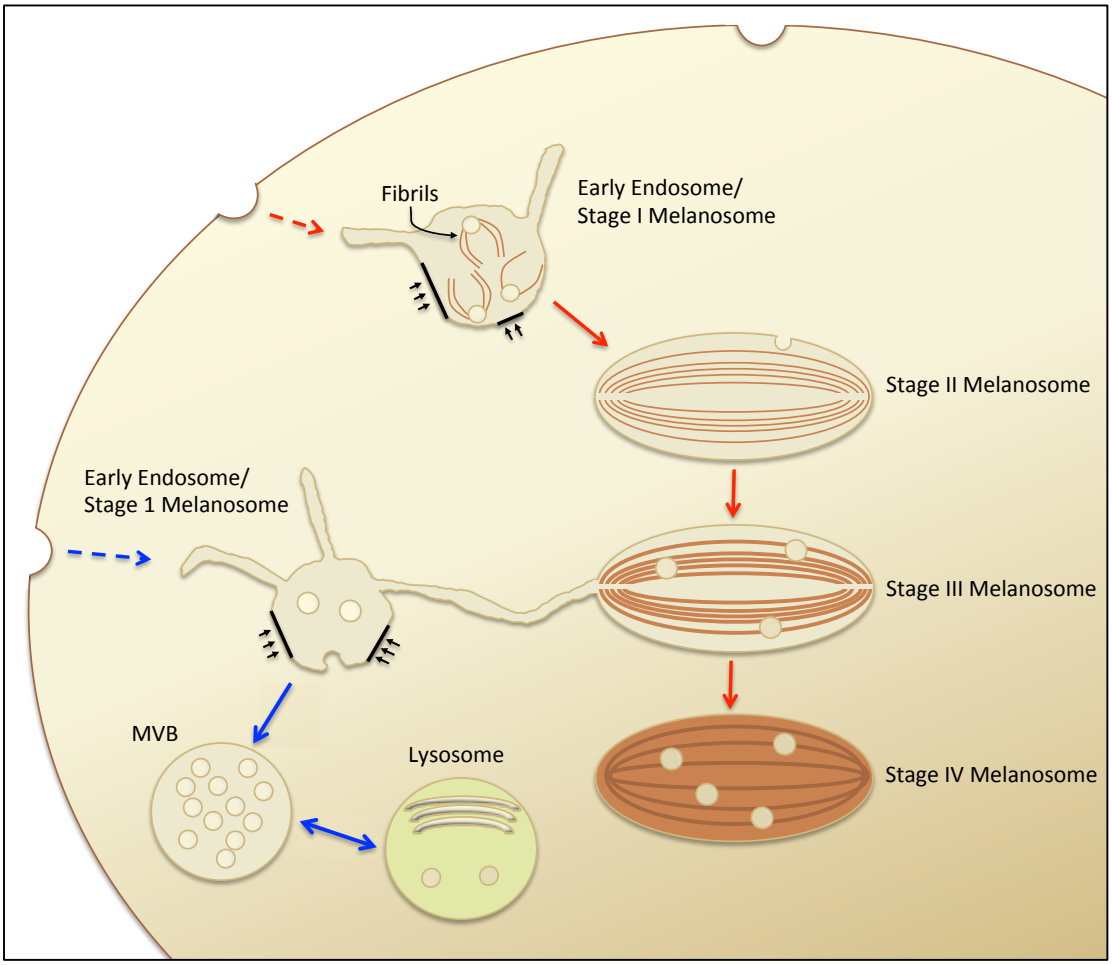

Maturation stages of Lysosomes (blue arrows) and Melanosomes (red arrows) from early endosomes/stage 1 melanosomes. Early endosomes (EE) form from membranes derived by internalisation from the plasma membrane (dashed arrows red and blue) and also from membranes formed by the secretory pathway (not shown). EE are comprised of tubular domains and vacuolar domains; from which internal vesicles form by the invagination of the limiting membrane in regions adjacent to bilayered clathrin-and Hrs-containing coat regions (black arrows). These vacuolar domains mature into late endosomal multi-vesicular bodies (MVBs). The lumenal contents of the MVBs degrade after fusion with lysosomes. In pigment cells, the vacuolar domains of EEs can also be categorised as Stage I melanosomes. They are unique from vacuolar early endosomes of other cells as they contain fibrils that protrude from internal vesicles. The fibrils elongate and assemble into sheets (Stage II Melansomes). The delivery of contents to Stage II melanosomes by tubular intermediates from EE (as shown) or recycling endosomes (not shown) results in the deposition of melanins on the fibrils in Stage III melanosomes. The continuation of this process leads to the formation of Stage IV melanosomes. Figure adapted from (*8*).

Melanosomes share a number of features with lysosomes, including the presence of lysosomal proteins, an acidic luminal environment, accessibility to endocytic tracers, and the ability to fuse with phagosomes (*1*). The maturation of melanosomes takes place in four distinct stages (Figure 2), beginning with the development of the vacuolar domains (stage I) into nonpigmented stage II pre-melanosomes, in which the ILVs scaffold the polymerisation of amyloid fibrils by the pigment cell-specific protein PMEL (*9*). *Pmel*$^{-/-}$ mice form round melanosomes that lack characteristic striations, yet still remain segregated from

the endosomal system (*10*). The delivery of cargo to stage II melanosomes results in the deposition of melanins on the fibrils in stage III melanosomes and finally in stage IV melanosomes, this continued deposition of melanin masks internal structure. Not only do melanosome biogenesis pathways involve complex early endosomes, which sort cargo to multiple destinations via multiple exit routes but also multiple parallel pathways. As a result, it has proved complex to separate the effects of mutations on melanosome cargo delivery from mutations that effect the recycling pathways that retrieve key components from melanosomes to supply further rounds of cargo delivery (*11*). Melanin synthesis in stages III and IV requires the selective targeting of integral membrane melanogenic enzymes, such as tyrosinase and tyrosinase-related protein 1 (Tyrp1), and other components that regulate enzyme activity, from early endosomal intermediates to stage II melanosomes (*12*) via recycling endosomes (*13*). Defects in the trafficking of melanosomal cargoes such as Tyrp1 to melanosomes during melanosome biogenesis underlie oculocutaneous albinism in HPS (*14*). The ability to sort these macromolecules correctly is only found in a sub-set of specialised pigment host cells and to achieve this, these cells must correctly distinguish macromolecules that are destined for conventional lysosomes from those destined for the melanosome (*15*). The need for this sorting can be demonstrated when melanosomal proteins are expressed ectopically in non-pigment cells (*16*–*18*) where they localise to late endosomes and lysosomes.

Research on LROs, though initially focused on the melanosomes, progressed further to include a larger group of specialised organelles in host cells. The LROs that are the focus in this thesis are the WPBs, platelet dense granules and platelet alpha granules, all of which are primarily involved in the process of haemostasis.

2.3 Haemostasis

Haemostasis is a complex physiological process that involves the tightly regulated processes of blood clotting, platelet activation and vascular repair (*19*). Following damage to the cell layer that lines the vascular walls, endothelial

activation leads to the exocytosis of the WPB in which vWF is stored. This, together with any vWF bound to the subendothelial matrix exposed by damage, recruits platelets from the blood. This capture and adhesion of platelets in the blood flow causes them to change their shape and to form pseudopods. The signalling initiated by platelet activation also causes activation of integrin αIIbβ3 and the secretion of bioactive molecules (*20*) from their preformed LROs, cytoplasmic dense and alpha granules, which amplify aggregation. Multiple flowing platelets then aggregate via fibrinogen bridges through the action of thrombin and contract to form a tightly packed thrombus termed the platelet plug (21). The accumulated platelet plug temporarily functions to prevent bleeding, however, it is easily dislodged from the vessel wall and thus, a secondary haemostatic response is required (*22*). After the platelet plug is formed, the proteolytic coagulation cascade leads to the deposition of insoluble fibrin that strengthens and stabilises the thrombus and in turn acts as adhesion sites for coagulation factors. This process of fibrin generation occurs simultaneously to platelet aggregation (*23*) and is activated within seconds of an injury, is tightly regulated and importantly is localised to the site of injury (*24*). This process of haemostasis is critical to cover a break in the vessel wall (*25*) and is reliant on LROs such as platelet granules and WPBs, which are discussed in detail below.

2.4 Platelet granules

Platelets are small (2-5 μM) anuclear secretory cell fragments that originate from megakaryocytes (MKs). During maturation, MKs grow in size and replicate their DNA without cytokinesis (polyploidy) through a process called endomitosis. As MKs mature, they develop a highly invaginated demarcation membrane system whilst their cytoplasm concurrently becomes filled with platelet granules. They have an average lifespan of about 10 days before removal by the spleen (*26*) and each day an adult produces about 100 billion platelets (*27*). Platelets play a vital role in regulating haemostasis.

The contents of platelets include an open canalicular system, a dense tubular system and secretory granules, from which bioactive molecules are released and in turn most platelet functions are mediated. Platelet granules originate from multi-vesicular bodies (MVBs)/late endosomes in MKs, but little is known about the exact mechanisms by which granule cargo is sorted and trafficked (*20*). In the MKs, granules are formed from the budding of small vesicles containing granule cargo from the trans-Golgi network (*28*, *29*). This cargo is delivered directly to MVBs, where the proteins are sorted and packaged into granules (*30*). Historically, platelet granules have been classified into distinct groups based on their content and appearance by electron microscopy (EM); dense granules, alpha granules, MVBs, lysosomes (*25*), and more recently, T granules (*31*)**.** Alpha granules and dense granules are both categorised as LROs as they derive from similar precursors and share fusion machinery important for secretion, but their formation is differentially regulated (*32*).

The critical role played by platelets in haemostasis is dependent on platelet granule integrity; deficiencies in these organelles, including abnormalities in granule number or size, are associated with bleeding symptoms (*33*). Most inherited platelet storage pool disorders (PSDs) disrupt the function of either alpha or dense granules, but not both, suggesting the existence of distinct granule biogenesis pathways for the two subtypes. For example, in genetic disorders such as HPS and Chediak-Higashi Syndrome (CHS) the absence of dense granules (*1*, *3*, *34*–*36*) significantly slows the rate of effective haemostasis at the site of an injury (*37*), and in Grey Platelet Syndrome (GPS) patients similarly suffer from a bleeding disorder which is caused by an underlying defect in the ability of platelets to store alpha granule proteins (*38*).

2.4.1 Alpha Granules

Alpha granules have the properties of both secretory organelles and late endosomes, which qualify their characterization as an LRO. Alpha granules are the major storage and secretory organelle in the platelet, being the most abundant granules; numbering around 50-80 per platelet (*39*). Formed from

multi-vesicular precursor organelles, alpha granule contents are acquired from both the endocytic and biosynthetic routes (*30*).

Alpha granules contain over 300 distinct molecules, which makes up the bulk of the platelet secretome (*40*). These include haemostatic factors, angiogenic factors, anti-angiogenic factors, growth factors, proteases, necrotic factors and other cytokines (*40*). Little is known about the mechanism of alpha granule biogenesis (*41*), which is affected in three inherited human disorders: Quebec Platelet Disorder, GPS and arthrogryposis, renal dysfunction and cholestasis (ARC) syndrome. In GPS the amount of protein synthesised in MKs is significantly reduced, although endocytosed alpha granule content is less affected. It has recently been demonstrated that mutations in the Neurobeachin-like 2 (*NBEAL2*) gene cause GPS (*42*) and these mutations appear to be involved in the packing of endogenously synthesised secretory proteins into developing alpha granules (for a continued platelet alpha granule introduction also see 6.1.1).

2.4.2 Dense Granules

Dense granules are around 150 nm in size, originate from endosomal precursors and belong to a secretory compartment from which content is released during platelet activation (*29*). Dense granules are typically identified using Electron Microscopy (EM) and are recognizable by the presence of a very electron-dense core, which is caused by their high calcium and phosphate content. Dense granules are acidic and therefore accumulate acidic dyes such as mepacrine (*43*) and acridine orange (*44*). Their content is simpler than alpha granules and contains a variety of important haemostatically active substances. Platelet dense granules release their contents into the extracellular medium upon activation, these include; serotonin, histamine, catecholamines (*45*), adenosine 5′-diphosphate (ADP), adenosine 5′-triphosphate (ATP), polyphosphate (*46*), magnesium pyrosphate and calcium (*47*). ADP secreted from platelet dense granules stimulates platelets arriving at the site of injury, amplifying the response of platelets to primary agonists and facilitating the formation of the platelet plug (*48*). Dense granules also contain the lysosomal membrane proteins

CD63 (*35*) and LAMP1/2 (*49*), but also non-lysosomal proteins such as P-selectin, GPIb and αII-β3 integrin (*50*); which are translocated to the cell surface upon platelet activation. Dense granules also carry Rab27a and b (*51*, *52*) which are required for content release (see also 2.6.2), Rab proteins are defined as Ras-like monomeric GTPases and have been implicated in the control of protein trafficking as regulators of vesicular transport such as vesicle budding, movement, and docking/fusion (*53*) (for a continued platelet dense granule introduction also see 6.1.2).

Melanosomes and platelet granules are closely related and are both formed from endosomes that are transformed by the delivery of specialised cargo. However, there are other LROs, such as WPBs, that are more distantly related. WPBs carry proteins such as P-selectin, Rab27a and CD63 common to other LROs however, unusual for an LRO, they do not originate from the endosome but are formed at the Golgi.

2.4.3 Weibel-Palade Bodies

Figure 3 Weibel-Palade Body biogenesis

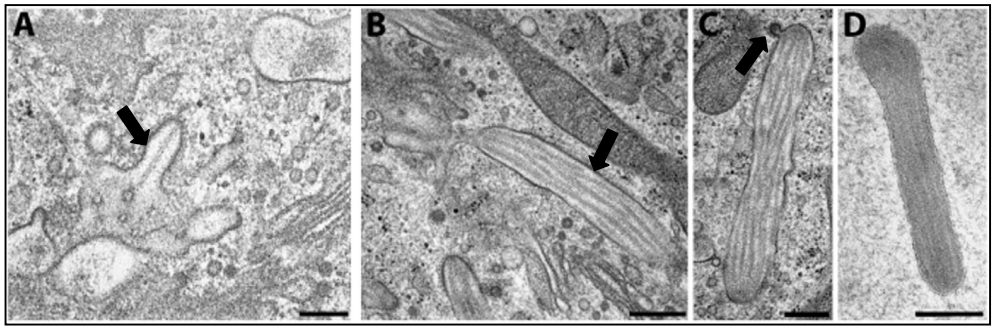

Biogenesis of WPBs in cultured human endothelial cells seen by high-pressure freezing/freeze substitution. (A) Tubule formation in the Trans-Golgi Network (TGN). (B) Immature WPB with electron-lucent interior. (C) Immature WPB with Clathrin- coated bud (D) Mature WPB demonstrating an increase in electron density that occurs during maturation. Bars, 200 nm. Figure from (*54*).

Ewald Weibel and George Palade first described WPBs in 1964 (*55*), as 'an unknown rod-shaped cytoplasmic component, which consists of a bundle of fine tubules, enveloped by a tight fitting membrane'. In 1982, WPBs were identified as the storage organelle for von Willebrand factor (vWF) protein (*56*).

Deficiencies, either quantitative or qualitative, in vWF are responsible for von Willebrand's disease (VWD), which is the most common inherited bleeding disorder in humans, occurring in approximately 1 out of every 100-1,000 people and affects both males and females (*57*).

Figure 4 vWF Domain Structure – formation and maturation of WPBs

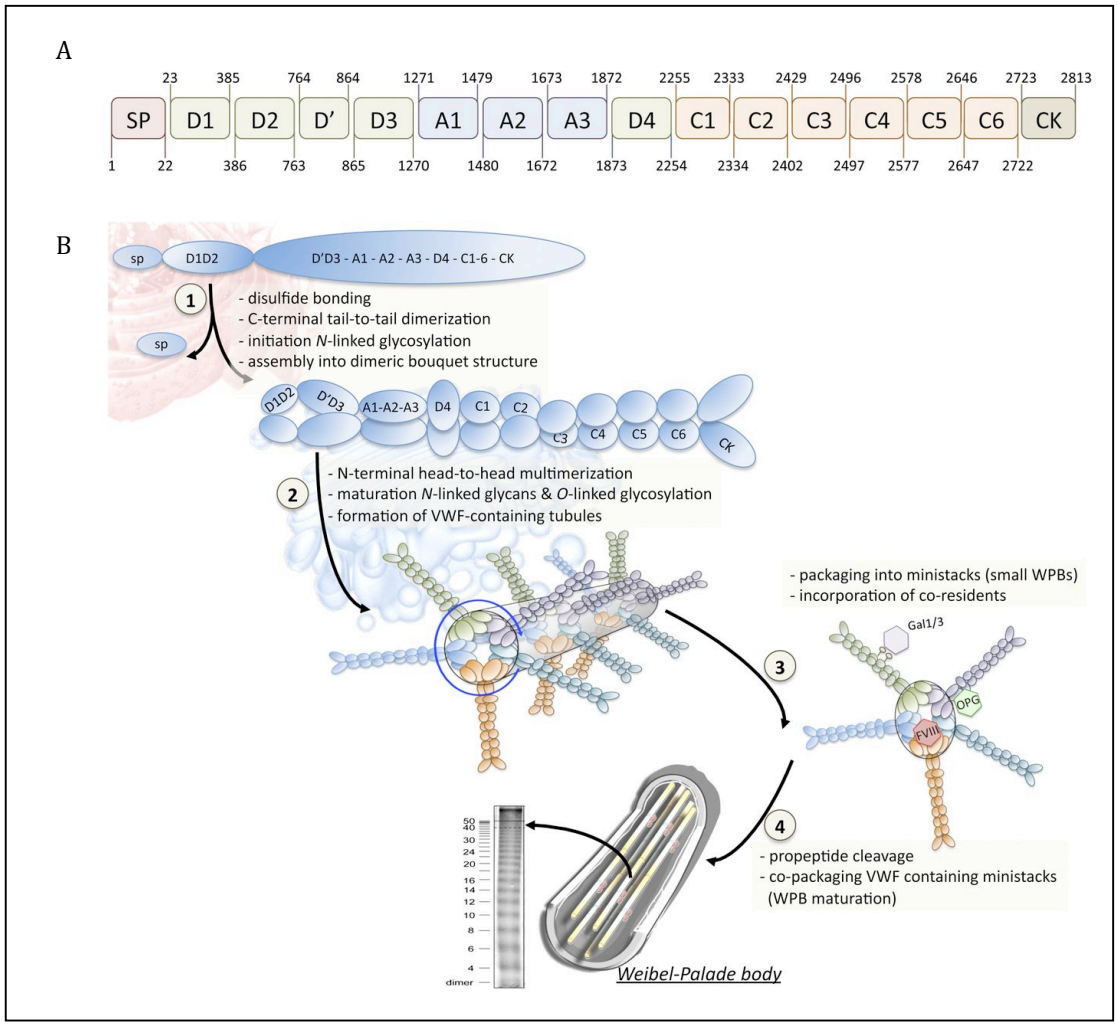

(A) Schematic representation of the domain arrangement of vWF. vWF is a mosaic protein composed of many types of domains. Many of these domains have specific functions in haemostasis; others function in formation during biosynthesis and give vWF the length and flexibility that enable a transition that activates haemostasis, The different domains are arranged in the order: D1-D2-D′-D3-A1-A2-A3-D4-B1-B2-B3-C1-C2-CK, with the D1-D2 domains representing the propeptide and the remainder corresponding to the mature VWF subunit (*58*). (B) Step 1: Dimerisation, Step 2: Multimerisation, Step 3: Packaging into Ministacks, Step 4: Co-packaging. (Final black arrow) A multimer Gel can be used to determine multimers formed and can be an indicator of vWD (see 4.7.3 for method) Figure from (*59*)

vWF is synthesised as 350 kDa monomers, which are co-translationally translocated into the Endoplasmic Reticulum where they dimerise (*54*). Upon arrival in the Golgi apparatus, the presence of an acidic pH and relatively high calcium concentrations promote the organisation of the pro-dimers into a dimeric bouquet structure (*60*), in which the dimers are aligned into a side-by-side manner (Figure 4, step 1) and organise into a right-handed helical structure,

which enables a 100-fold compaction of the protein. In this helical structure, the wall of a hollow tube is formed by the pro-peptide (D1-D2 domains) and the D′-D3 domains. The remaining A1-CK domains project out from the helical structure, and are located in the area between the tubules (Figure 4, step 2). The assembly into tubules allows for controlled formation of disulphide bonds between the dimers, and thus concatamerisation of the vWF into much larger assemblies- "multimerisation" (*61*). vWF is capable of forming multimers of up to 20 million Da, or 50-mers of dimers (*62*). On a macro level, this set of biochemical transformations are being carried out on quanta of vWF (*63*), boluses of material that are sized by the transfer of this protein through the ministacks that are linked within the Golgi ribbon. In parallel, as vWF passes through the Golgi, maturation of the *N*-linked glycans proceeds while *O*-linked carbohydrate structures are also added to the protein (Figure 4, step 3) Finally, in a late but poorly defined stage, the proteolytic separation of the pro- peptide from mature vWF subunits is mediated by Furin (Figure 4, step 4). Once delivered to the TGN, where they are present within a continuous lumen, the adjacent quanta now become transformed into tubules/multimers that can be co-packaged together into forming organelles, where the number of quanta that become co-packaged define WPB length (*63*).

Acidic pH is required for the conformational changes that lead to compaction (*60*), tubulation (*64*) and multimerisation of vWF (*65*). The importance of this is demonstrated by introducing a weak base such as ammonium chloride, which raises the pH in the Golgi, leading to a complete halt in WPB formation (*63*). The formation of WPBs is completely dependent on the N-terminus-driven tubulation of vWF subunits and the oxido-reductase activity of the pro-peptide but surprisingly, is not dependent on high levels of multimerisation. Tubulation and multimerisation are independent processes and this is highlighted when these processes are differentially inhibited. Treatment with monensin, which disrupts the interaction between the pro-peptide and mature vWF has no effect on the formation of disulphide bonds, disrupts tubulation and subsequently post-Golgi WPBs are dramatically rounded (*66*). When cells are treated with dithiothreitol (DTT), which conversely disrupts disulphide bridge formation yet does not affect

interactions between the pro-peptide and mature vWF, the elongation of WPBs is not reduced (*67*). Yet if dimerisation is prevented, by the expression of vWF lacking the CK domain, rod-shaped granules containing vWF tubules are still formed. Both dimerisation and multimerisation require an interaction of the pro-peptide with the mature protein, which can explain why mutations that appear to affect multimerisation can also affect tubulation (*67*).

WPB biogenesis and the trafficking machinery involved

Figure 5 WPB biogenesis and the trafficking machinery involved

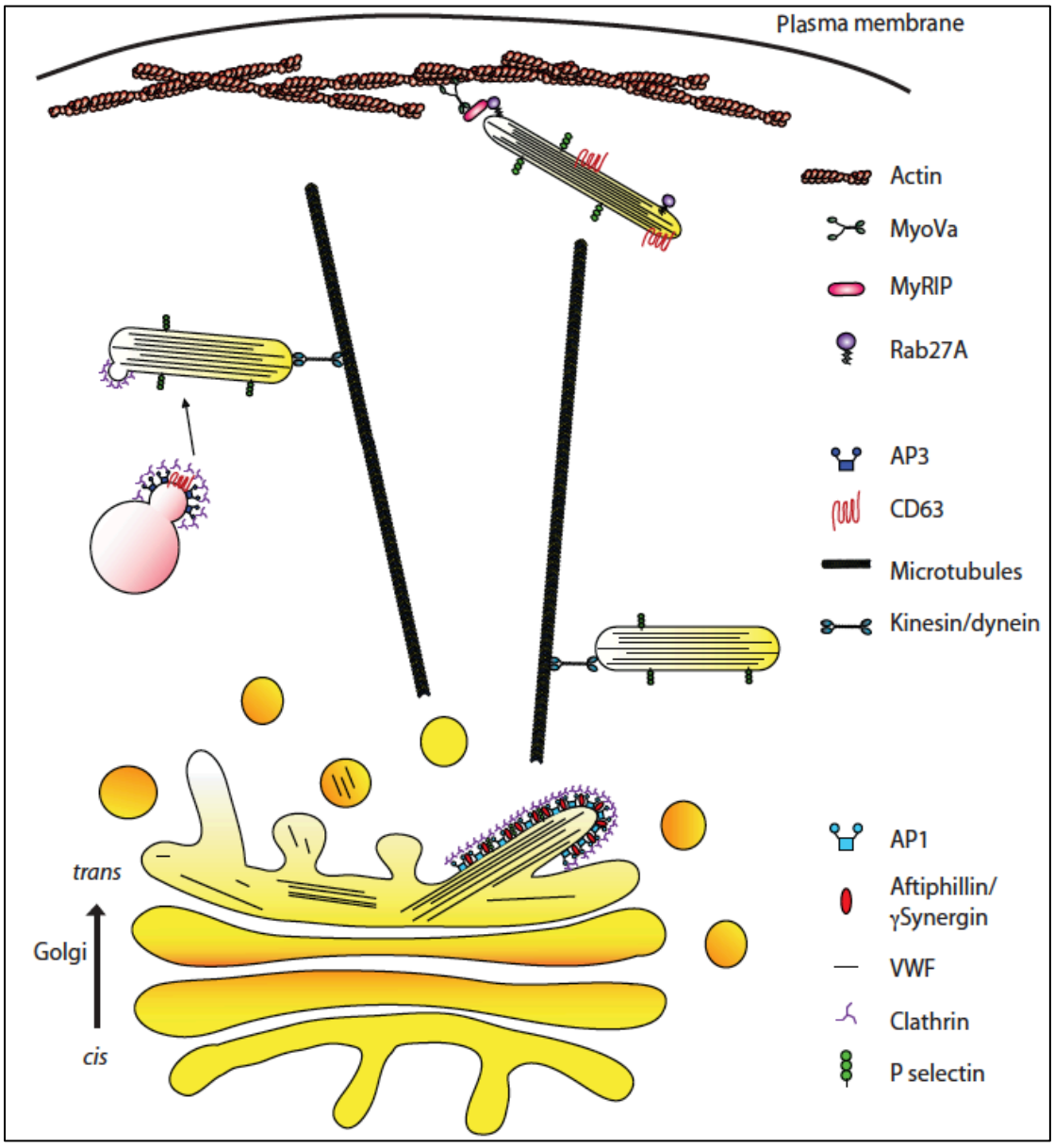

WPB formation and maturation. WPB associated machinery displayed in right panel and their location within the process of WPB biogenesis from the Golgi to the plasma membrane. Figure from (*68*)

To achieve the correct formation of WPBs at the TGN, Clathrin (a molecular scaffold protein) and the AP-1 adaptor are required and likely act as an external scaffold (*69*). The depletion of the AP-1 effectors aftiphilin/γ-synergin in HEK293 cells leads to the production of pseudo-WPBs that are morphologically indistinguishable from controls and show normal acquisition of all the known components of WPBs, including P-selectin, CD63, and Rab27a (an isoform of Rab27) (*70*). These organelles, however, fail to respond to secretagogue, releasing their content in an unregulated manner (*70*). Further, in contrast to AP-1 knockdown (KD), aftiphilin/γ-synergin depletion leads to an increase in the release of highly multimerised vWF (a feature unique to mature WPBs) in the absence of secretagogue (*70*).

Microtubules are thought to be principally responsible for WPB long-range motion, and treating cells with nocodazole, an antineoplastic agent that disrupts the polymerisation of microtubules, prevents WPB transport over long distances (*71*). Unidirectional transport to the cell periphery is induced by aurintricaboxylic acid treatment, which inhibits kinesin motor proteins, suggesting that microtubule-dependent transport of WPBs is a balance between kinesin and dynein (Figure 5), the plus and minus end directed motors (*71*).

Upon fusion with the plasma membrane, the shift in pH (from around the 5.5 found within the organelles to the 7.4 of the extracellular environment (*72*)) prompts the dissociation of pro-peptide from the mature vWF, uncoiling of the tubules and release of this cargo, that then appears as vWF strings that can be up to 1 mm long (*73*). These strings are anchored to the endothelial surface, where they recruit platelets, contributing to the formation of a haemostatic plug, and thus reducing bleeding (see 2.3).

A correct biogenetic process is required for a fully functional organelle; therefore, the number of WPBs, the size distribution of WPBs, the amount and the multimeric composition of vWF secreted in the absence or presence of agonists can all be used as indicators of defects in proteins important for biogenesis. In addition to vWF, a number of proteins are recruited to WPBs at the

TGN. The best studied of these is the transmembrane cell adhesion molecule, P-selectin. At the TGN the leukocyte receptor P-selectin is sorted into forming WPBs by direct physical interaction with vWF multimers (*74*). Upon WPB exocytosis, P-selectin rapidly diffuses into the plasma membrane to initiate leukocyte recruitment (*75*–*77*). Leukocytes bind to P-selectin molecules on the inner wall of the vessel, this causes the leukocytes to slow down and begin ''rolling'' along the vessel wall.

All LROs progressively mature from precursors, although the origin of these precursors differs (*9*). The observation that WPBs are capable of acquiring new components by post-Golgi trafficking, a typical characteristic of LROs, adds to the suggestion that WPBs should fall within this classification. The two best-known examples of this are the recruitment of Rab27a (and its effectors) and CD63.

Rab27a is recruited to mature WPBs (*78*) and other LROs (see 2.6.2) and is important for controlling exocytosis (*79*). Rab27a is required for the formation of a complex with MyRIP/MyoVa that peripherally anchors WPBs (Figure 5) to actin stress fibres (*80*). Rab27a siRNA ablation results in an increase in both basal and stimulated secretion of vWF; however, in these circumstances, the number of high molecular weight multimers of vWF is reduced and vWF string length is shortened (*81*).

CD63 is a tetraspanin, so called because of their common feature of four membrane-spanning regions. They are involved in a number of cellular processes including cell adhesion and differentiation (*82*) and have been described as 'molecular organisers' (*83*), acting within the plane of the bi-layer on other membrane proteins. Besides its universal localisation to endosomes and lysosomes, CD63 has been found in mature WPBs (and other LROs such as melanosomes and platelet granules) to where it is recruited in an AP-3-dependent manner, thus distinguishing it from P-Selectin which is recruited to forming WPBs at the TGN (*74*). Silencing of CD63 affects P-selectin-dependent leukocyte rolling, revealing that CD63 is an essential cofactor for P-Selectin

receptor function at the cell surface (*84*), acting by clustering the leukocyte receptor to increase its avidity.

Even though the cargo delivered to LROs can be used to help define this group, it is often difficult to define whether an organelle is indeed an LRO or not. The identification and classification of these organelles has also been facilitated by the observation that most are affected by a small cluster of genetic disorders

2.5 LRO associated disorders

2.5.1 Grey Platelet Syndrome

Clinical features of GPS include a mild to moderate bleeding syndrome, enlarged platelets in fewer numbers, myelofibrosis (a disorder of hematopoiesis), emperipolesis (an intact cell within the cytoplasm of another cell) of leukocytes by MKs and splenomegaly (enlargement of the spleen) (*85*). GPS was given its name due to the grey appearance of patient's platelets in a peripheral blood smear (38). GPS platelets are hypogranular (*86*) and highly variable in their size and morphology. Immuno-electron microscopic analysis has shown that alpha granule numbers appear significantly reduced and lacking content (*87*), however dense granules, lysosomes and peroxisomes are present in typical numbers (*88*) . In GPS, the alpha granule cargo is deposited primarily into the bone marrow; the granule membrane constituents including P-selectin remain but are abnormally distributed in MKs (*89*). The empty alpha granules have been shown to be able to re-distribute and fuse with the platelet cell surface membrane upon activation, reinforcing the idea that GPS is not a secretion problem but a storage deficiency (*90*).

Next generation sequencing techniques recently identified the genetic basis for GPS; mutations in the *NBEAL2* gene, which encodes a BEACH/ARM/WD40 domain protein. This family of proteins have highly conserved regions that are crucial for protein-protein interactions, membrane dynamics and vesicle trafficking (*42*). NBEAL2 is predicted to regulate platelet alpha granule

biogenesis given their aberrant features in GPS, however, the underlying mechanism is still unknown. *Nbeal2(-/-)* mice display the characteristics of human GPS, with defective alpha granule biogenesis in MKs and their absence from platelets (*91*). The presence of P-selectin and the normal levels of the Sec1/Munc18 protein VPS33B and it's binding partner VPS16B (proteins required for alpha granule biogenesis (*92*)) in *Nbeal2(-/-)* mouse platelets suggests that NBEAL2 acts independently of these and at a later stage of the biogenesis of alpha granules (*93*). *NBEAL2* belongs to the same gene family as *LYST* (or *CHS1* gene) the target gene for mutations leading to platelet dense granule deficiency in CHS (*89*). Other LROs, such as melanosomes and those in the immune system, are also defective when this close relative, LYST, is defective, further reiterating the classification of LROs as a group. The prototype syndrome by which LROs were initially clustered was, however, HPS.

2.5.2 Hermansky Pudlak Syndrome

Hermansky Pudlak Syndrome (HPS), the main focus of the work in this PhD, is an autosomal recessive disorder affecting a number of proteins related to LRO function. It was discovered by Hermansky and Pudlak in 1959 (*94*) and yet relatively little is understood about the mechanisms of this genetic disorder. The largest groups of patients with HPS originate from the north-western region Puerto Rico, where its frequency is estimated to be 1:1800 (*37*) probably due to a founder effect. The overall frequency of HPS in the human population is speculated to be around 1 in 500,000 (*95*), however as many patients are misdiagnosed, the actual numbers are suspected to be higher.

Figure 6 HPS patient - albinism and platelet granule deficiency

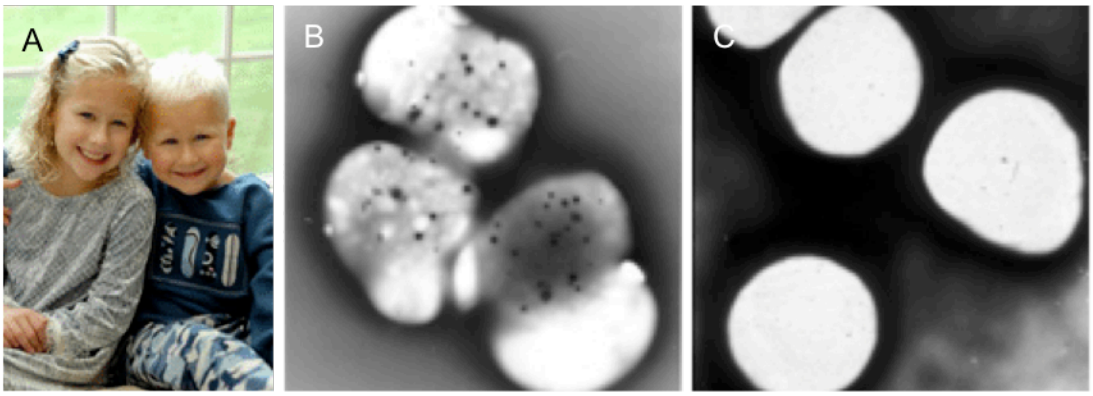

A) HPS patients displaying albinism as seen by pale hair colour B) All HPS patients demonstrate a reduction in dense granules in platelets as observed by whole mount microscopy, an example of a HPS1 patient (C) with a dramatic reduction in dense granules, note the absence of dense spots compared to the control (B). Images from hpsnetwork.org (*95*).

The symptoms of HPS typically include; eye and skin albinism, visual impairment, a bleeding disorder, inflammatory bowel disease and lung fibrosis (Figure 7 (*37*)). In rare cases, immunodeficiency has also been observed (*96*). It is common for HPS patients to be misdiagnosed with Oculocutaneous albinism and Ocular Albinism as the criteria for diagnosing these disorders is indistinguishable from the albinism seen in HPS (*97*). In 2013 it was reported that 76% of patients with HPS were initially misdiagnosed and 28% of patients had to see between four and six specialists before receiving the correct diagnosis (*98*).

The broad range of symptoms exhibited by HPS patients are suggestive of HPS proteins functioning in a diverse set of cellular processes, including the biogenesis, secretion and trafficking of LROs such as melanosomes and platelet granules. Indeed, platelets in HPS have been shown to have a reduction in platelet dense granules as visualised by whole mount EM (*36*), yet despite the storage/release of serotonin and adenine nucleotides being defective, alpha granules are unaffected (*99*). It is still to be determined whether the only function of the HPS proteins is the regulation of the biogenesis of LROs; the fact that these genes are expressed ubiquitously throughout the body suggests that they may fulfil a number of other more general functions. Pigment deficient mouse models, that have been attributed to HPS (Figure 7) have not only been

proven useful for studies investigating the function of the HPS genes but also to further our understanding of the regulation and biosynthesis of LROs in general (*4*, *34*). There are currently 9 genes (a recent publication has suggested there may now be 10 (*100*)) that have been associated with HPS in humans (Figure 7). All HPS mutations result in albinism, visual impairment and a bleeding disorder (*37*). However, only HPS1, 2 and 4 have been associated with lung fibrosis, the most life threatening of the HPS symptoms. Biochemical studies have revealed that the genes HPS1-9 all encode proteins that can be grouped into the biogenesis of lysosome related organelle complexes (BLOCs) 1-3 (*101*) and the adaptor protein, AP-3 (Figure 7). The pigment deficient mouse models have also predicted and revealed a number of other potential HPS proteins that are not part of the BLOC or AP-3 complexes, such as Rab27a (*102*), RabGGTase (*103*) and VPS33a (a subunit of the class C core vacuole/endosome tethering (CORVET) complex and the mammalian homotypic fusion and vacuole protein sorting (HOPS) complex) (summarised in Figure 7) the characteristics of these complexes and associated proteins are discussed below.

Figure 7 HPS - nomenclature, complexes and symptoms

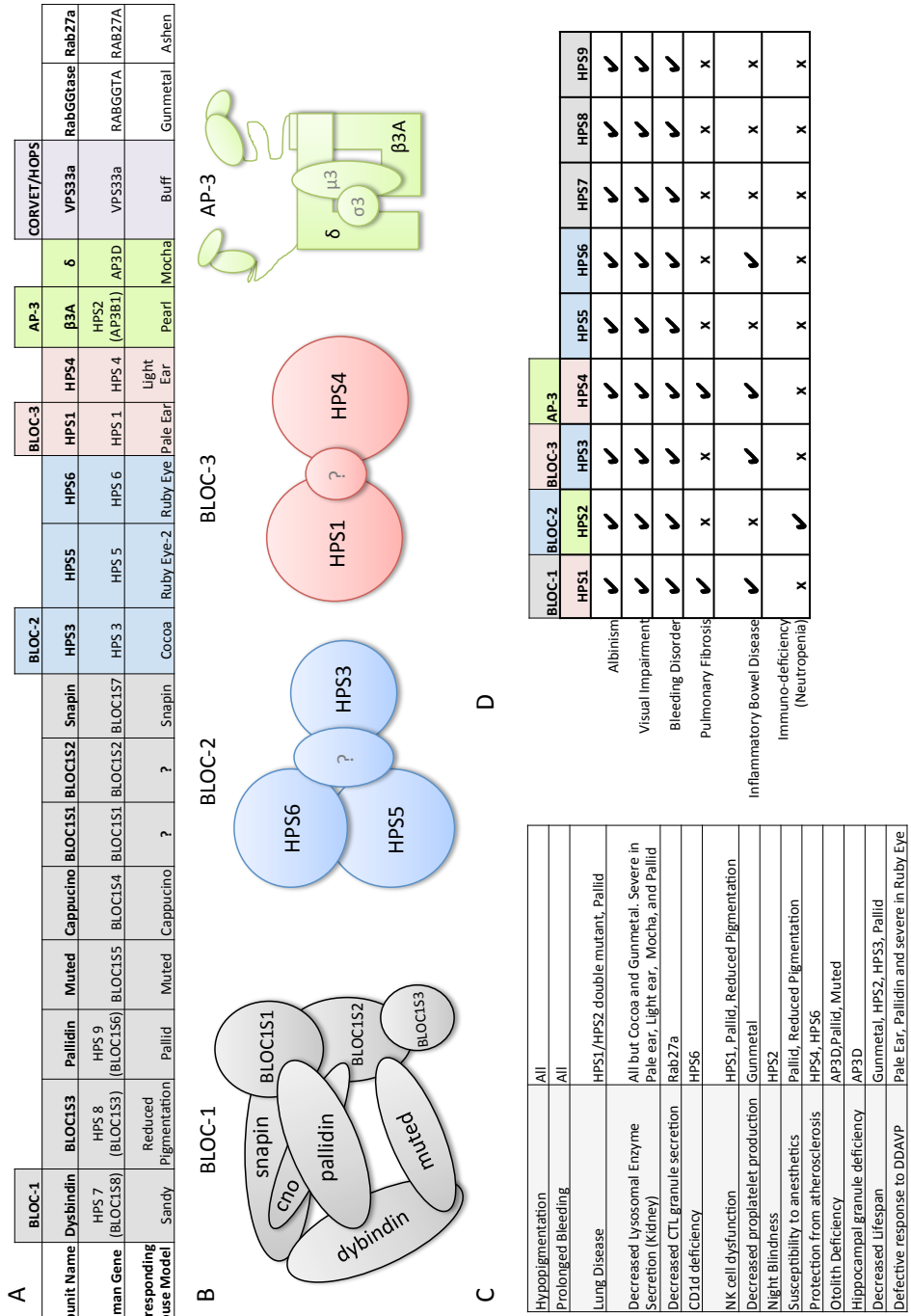

	BLOC-1								BLOC-2			BLOC-3		AP-3		CORVET/HOPS		
Subunit Name	Dysbindin	BLOC1S3	Pallidin	Muted	Cappucino	BLOC1S1	BLOC1S2	Snapin	HPS3	HPS5	HPS6	HPS1	HPS4	β3A	δ	VPS33a	RabGGtase	Rab27a
Human Gene	HPS 7 (BLOC1S8)	HPS 8 (BLOC1S3)	HPS 9 (BLOC1S6)	BLOC1S5	BLOC1S4	BLOC1S1	BLOC1S2	BLOC1S7	HPS 3	HPS 5	HPS 6	HPS 1	HPS 4	HPS2 (AP3B1)	AP3D	VPS33a	RABGGTA	RAB27A
Corresponding Mouse Model	Sandy	Reduced Pigmentation	Pallid	Muted	Cappucino	?	?	Snapin	Cocoa	Ruby Eye-2	Ruby Eye	Pale Ear	Light Ear	Pearl	Mocha	Buff	Gunmetal	Ashen

	BLOC-1	BLOC-2	BLOC-3	AP-3					
	HPS1	HPS2	HPS3	HPS4	HPS5	HPS6	HPS7	HPS8	HPS9
Albinism	✔	✔	✔	✔	✔	✔	✔	✔	✔
Visual Impairment	✔	✔	✔	✔	✔	✔	✔	✔	✔
Bleeding Disorder	✔	✔	✔	✔	✔	✔	✔	✔	✔
Pulmonary Fibrosis	✔	x	x	✔	x	x	x	x	x
Inflammatory Bowel Disease	✔	x	✔	✔	x	✔	x	x	x
Immuno-deficiency (Neutropenia)	x	✔	x	x	x	x	x	x	x

Hypopigmentation	All
Prolonged Bleeding	All
Lung Disease	HPS1/HPS2 double mutant, Pallid
Decreased Lysosomal Enzyme Secretion (Kidney)	All but Cocoa and Gunmetal. Severe in Pale ear, Light ear, Mocha, and Pallid
Decreased CTL granule secretion	Rab27a
CD1d deficiency	HPS6
NK cell dysfunction	HPS1, Pallid, Reduced Pigmentation
Decreased proplatelet production	Gunmetal
Night Blindness	HPS2
Susceptibility to anesthetics	Pallid, Reduced Pigmentation
Protection from atherosclerosis	HPS4, HPS6
Otolith Deficiency	AP3D,Pallid, Muted
Hippocampal granule deficiency	AP3D
Decreased Lifespan	Gunmetal, HPS2, HPS3, Pallid
Defective response to DDAVP	Pale Ear, Pallidin and severe in Ruby Eye

HPS summary - (A) HPS subunits, human genes and corresponding mouse models, (B) HPS complexes and representative structure (*3*), (C) Symptoms displayed in HPS mouse models, (D) Symptoms displayed in Human HPS and related HPS genes and BLOCs. (A,B,D) BLOC-1 Grey, BLOC-2 Blue, BLOC-3 Red, AP-3 Green.

2.5.3 BLOC-1

BLOC-1 is comprised of eight subunits named BLOS1, BLOS2, BLOS3 (HPS8), pallidin (HPS9), snapin, muted, cappuccino, and dysbindin (HPS7) (Figure 7) (*104–107*). The eight subunits appear predominantly alpha helical in structure (*108*) and appear as a linear chain of eight globular domain $\sim$300 Å long and $\sim$30 Å in diameter which localise to early endosomal tubules. Two stable sub-complexes have been identified, pallidin-Cappuccino-BLOS1 and dysbindin-Snapin-BLOS2 (*107*).

BLOC-1 expression is ubiquitous, yet disruption of BLOC-1 function has currently manifested itself with overt phenotypes in only a subset of cell types such as neurons, melanocytes and platelets (*14*). Although the mechanisms are still unclear, BLOC-1 is thought to have several interaction partners including 'Soluble N-ethylmaleimide-sensitive factor activating protein receptors' (SNAREs) (*109*), a large group of membrane-bound proteins that mediate fusion throughout the secretory and endocytic pathways and are also important in the biogenesis of LROs such as melanosomes and platelet dense granules (*110*). Despite its association with LRO function, BLOC-1 is not associated with lysosomes (*111*, *112*).

Mouse mutants defective in BLOC-1 components have the most severe phenotypes. Recently Delevoye et al. (*14*) confirmed the importance of BLOC-1's function in the formation of recycling endosomes and demonstrated its role in bringing together the actin and microtubule cytoskeletons to generate recycling endosomes in HeLa cells. BLOC-1 is also required for cargo-specific sorting from vacuolar early endosomes toward LROs (*113*) and BLOC-1-deficient fibroblasts have demonstrated an altered intracellular distribution or cell accumulation of endosomal proteins (*111*). It is clear that there is a link between BLOC-1 and AP-3 function (see also 2.6.1), as BLOC-1 alters the targeting of AP-3 cargoes such as LAMP1, phosphatidylinositol-4-kinase type II alpha and VAMP7-TI in neuronal

cells (*114*). Di Pietro et al. (*111*) demonstrated that not only can BLOC-1 interact physically and functionally with AP-3 to facilitate the trafficking of CD63 and of the melanosomal membrane protein Tyrp1 but it can also act independently of AP-3, interacting directly with BLOC-2 to facilitate Tyrp1 trafficking to melanosomes.

2.5.4 BLOC-2

BLOC-2 contains the proteins HPS3, HPS5 and HPS6 as subunits and is the least understood of the three BLOC complexes (*115*). BLOC-2 is thought to play more of a regulatory role in LRO biogenesis due to the lack of lung fibrosis seen in patients containing the relevant mutations (*116*). BLOC-2 deficient mice have a less severe pigment phenotype and platelet aggregation defects than other BLOC deficient mouse models. BLOC-2 complex proteins lack obvious structural features apart from the WD40 domains in HPS5 (*117*) and a potential clathrin binding domain in HPS3 (*118*). Interestingly, BLOC-2 has been shown to associate with other components required for LRO biogenesis such as the Rab GTPases Rab32 and Rab38 (*119*) and a number of the components of BLOC-1 (*111*, *114*, *120*). However, the precise role of BLOC-2 in LRO-related disorders is still unknown.

2.5.5 BLOC-3

BLOC-3 is a complex comprised of only two proteins, HPS1 and HPS4. An interaction between HPS1 and HPS4 was demonstrated by co-immunoprecipitation of endogenous proteins in either soluble or membrane-associated forms and by co-migration on a sucrose gradient (*121*). The size of the BLOC-3 complex is ~175 kDa as calculated from sedimentation velocity and gel filtration analyses, this also corresponds to the combined molecular mass of one copy of each of the HPS1 and HPS4 polypeptides (*122*). BLOC-3 has been shown to function as a guanine nucleotide exchange factor, stimulating the release of guanosine diphosphate (GDP) to allow binding of guanosine triphosphate (GTP) for the Rab GTPases Rab32 and Rab38 (*123*), which are important in regulating the fusion of vesicles delivering cargo to maturing dense granule-like

compartments in a MK cell line (*122*). An interaction screen also revealed a specific and strong interaction of BLOC-3 with the GTP-bound form of the endosomal GTPase, Rab9 (*124*). Despite these findings, the function of BLOC-3 in MKs and platelets is largely unknown (*32*).

2.6 Other HPS-related complexes and proteins

2.6.1 Adaptor Protein-3

The Adaptor Protein (AP) complexes are heterotetrameric protein complexes that mediate intracellular membrane trafficking along endocytic and secretory transport pathways (*125*). Five AP complexes have been identified (*126*), AP-1-5, each composed by two large subunits (one each of γ/α/δ/ε/ζ and β1-5, respectively), one medium-sized subunit (μ1–5) and one small-sized subunit (σ1–5).

Deficiency of the AP-3β3A subunit in AP-3, results in HPS2 (*127*, *128*) and in a recent publication, mutations in AP-3δ1 have been proposed to cause a new HPS subtype, HPS10 (*100*). AP-3 has been shown to play an important role in the budding of vesicles from early endosomal compartments and marks the exit site for lysosomal membrane proteins from endosome-associated tubules (*129*). A common feature of all HPS patients is that the lamellar bodies, LROs found in type II pneumocytes and keratinocytes, are enlarged and have increased phospholipid content (*130*). This enlargement of lamellar bodies has been shown to be even more pronounced in HPS2 patients compared to other HPS subtypes and also in the corresponding mouse model (Pearl) in which AP-3 is significantly reduced in the surfactant-secreting alveolar type 2 cells. AP-3 has also been shown to have a role in WPB biogenesis (*74*). In most cells, intracellular CD63 is predominantly associated with late endosome and lysosomal membranes, however, in endothelial cells approximately 30% is trafficked to WPBs in an AP-3-dependent manner (*131*). When AP-3 is depleted in HUVECs using siRNA, this dramatically reduces the delivery of CD63 to the WPBs (*74*) demonstrating that AP-3 functions in the delivery of cargo to LROs.

2.6.2 Rab27

Rab27 has two isoforms Rab27a and Rab27b, is widely expressed (*132*, *133*), and is involved in the functioning of several LROs (*134–136*) as well as secretory granules (*137–139*), as already discussed in the context of WPBs (see 2.4.3). A single point mutation in the mouse orthologue of Rab27a (*102*) is responsible for the phenotypes of ashen mice, including hypopigmentation, prolonged bleeding times and a PSD. The Ashen mouse has been used as a model for HPS (Figure 7) and for a subset of Griscelli syndrome patients. Platelets of mice with the ashen mutation have greatly reduced amounts of dense granule components such as serotonin and adenine nucleotides though near-normal numbers of dense granules. Thus, essentially normal numbers of platelet dense granules are produced but the granule interiors are abnormal (140). In melanocytes the actin-based migration of melanosomes to the cell periphery is affected when depleted of Rab27a (141).

2.6.3 Gunmetal (Rab geranylgeranyl transferase)

Another mouse model that has been associated with HPS is the *gunmetal* mouse (*Rggtagm*). These mice possess a mutation in the alpha subunit of Rab geranylgeranyl transferase (RGGT), a heterodimeric enzyme that adds prenyl groups to the carboxyl termini of Rab GTPases (*103*). This mouse model is defined as having a HPS-like phenotype due to the fact that the reduced level of RGGT activity affects only a few LROs, in particular melanocytes and platelets. The bleeding disorder in these mice involves macrothrombocytopenia (*142*), a reduction in platelet dense and alpha granule contents, and morphological defects in MKs that affect platelet maturation (*143*). In platelets, a few Rabs, such as Rab27a (see also 2.6.2), are affected by the reduction in functionality of the enzyme. Both Rab27a and Rab27b are found associated with the limiting membrane of platelet dense granules and to a lesser degree with alpha granules (*53*). Due to the Rab involvement in protein trafficking, decreased association of Rab27a or other Rabs with membranes likely results in impaired delivery of proteins to LROs (*1*).

2.7 Morphometric Analyses

Having discussed the machinery and the biological context in which it is operating, it is important to introduce the technical advances that underpinned the results achieved in this thesis. The analysis of LROs and their defects has been transformed in recent years by two technological advances; firstly, advancements in quantitative image analysis and secondly, the breaking of the diffraction barrier in light microscopy. A brief introduction to these rapidly evolving areas follows.

2.7.1 Quantitative image analysis

In relation to an organelle such as platelet granules or WPBs, morphology refers to the form and structure of said object. Using mathematical tools it is possible to gather a vast amount of information from images by extracting morphometric data from segmented objects (identified by a unique feature such as a fluorescent tag). This allows detection of subtle phenotypes that are unlikely to be apparent by eye. Advantages of this approach are that; automated computational analysis does not suffer from subjective bias, image analysis is relatively quick and multiple features can be analysed in parallel. These tools were essential in the quantitative analysis of LRO defects observed by microscopy.

To extract morphological features, a number of steps are typically performed to reduce noise and enhance contrast, to maximize the isolation of a given feature and obtain quantitative data. Methods of analyses prevalent in this thesis include the collection of information related to the feret diameter (defined as the longest diameter across a WPB in 2D projection) of WPBs (see Figure 24), the number of exocytic sites detected at the cell surface (see Figure 23) and the successful development of a novel tool to facilitate the automated detection of the number and location of fluorescently labelled proteins within platelets using 'Super Resolution Microscopy' (SRM) (see Chapter 2).

2.7.2 Super Resolution Microscopy

For a greater part of the 20th century scientists believed that, in optical microscopes, it would never be possible to be able to observe things smaller than roughly half the wavelength of light (200 nm) as described by Ernst Abbe in 1873 (*144*) . In reality, a microscope's resolution (as defined by the point spread function) is dependent on the numerical aperture of the lens and the wavelength of light used to illuminate the sample; this typically restricts resolution to 200-300 nm laterally and 500-700 nm axially (*145*). To resolve and count platelet granules (around 50-200 nm in diameter) a sub-diffraction limit approach was required. In recent years, principally 3 techniques have made sub-diffraction limit resolution a reality; Stimulated depletion microscopy (STED) (*146*), Structured illumination microscopy (SIM) (*147*) and Single Molecule Localization Microscopy (SMLM) (*148*); the latter two of these were employed in this study (see Chapter 2) and are introduced below.

2.7.2.1 Super Resolution – Localisation microscopy

If a number of molecules are close enough together that the diffraction-limited spots between them overlap, then the ability to resolve individual molecules in the sample is impaired. However, the purpose of localization microscopy is to find a way in which the diffraction-limited spots are different from each other, once this is achieved it is then possible to isolate them in a higher dimensional space. Once they are isolated it is possible to find the centre of each of the diffraction-limited spots with a much greater accuracy than the width of the spot. This allows the ability to plot the co-ordinates of all the molecules with a precision greater than that of the diffraction limit. There are a number of localisation microscopy techniques that have been developed to achieve this, including Photo-activated Light Microscopy (PALM) (*148*, *149*) and Stochastic Optical Reconstruction Microscopy (STORM) (*150*, *151*). During my PhD the

localisation technique used was Direct Stochastic Optical Reconstruction Microscopy (dSTORM).

Figure 8 dSTORM imaging of fixed COS-7 cells.

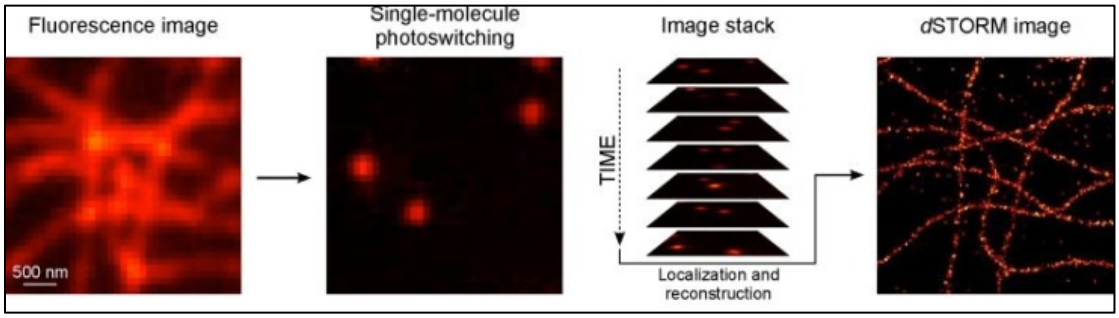

Microtubules stained with Alexa Fluor 647 labelled antibodies and imaged using dSTORM. Temporal separation of single emitters localised precisely by data modelling enables image reconstruction with superior resolution. Light-induced reversible photoswitching is achieved in the absence of an activator fluorophore in aqueous buffer and in the presence of millimolar concentrations of a reducing thiol compound such as DTT, glutathione, or mercaptoethylamine. The reducing thiol compound efficiently quenches the fluorophore's triplet state and generates a stable non-fluorescent reduced state (dark state) and requires high laser power. Figure from (*152*)

dSTORM utilises fluorophores that can be operated as reversible photoswitches. The localisation of individual fluorophores can be identified because the fluorophores will blink and thus can be separated temporally. dSTORM relies on the transfer of the majority of fluorophores to a non-fluorescent dark state for several seconds and precise localisation of individual fluorophores. The resolution that can be achieved depends not only on the brightness of the fluorophores, but also on the labelling density and the stability or lifetime of the non-fluorescent dark state (*153*). Using this method, a large number of fluorophore positions can be localised over thousands of frames. These localised positions can be used to build up an image of the sample with a resolution of below 30 nm in the xy plane (*148*).

2.7.2.2 Structure-illumination microscopy

Figure 9 Concept of resolution enhancement by structured illumination

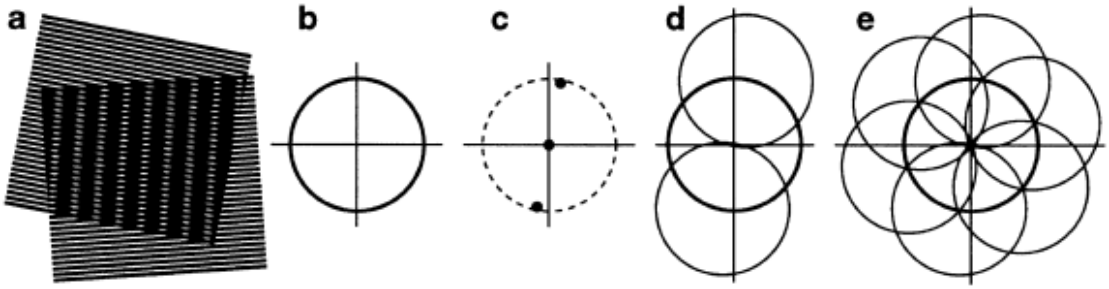

A fine grating is placed in an intermediate image plane of a widefield microscope, or is created using a spatial light modulator (*147*, *154*). If the sample is illuminated with such structured light, moiré fringes will appear (a), which represent information that has changed position in reciprocal space. The amounts of that movement correspond to the three Fourier components of the illumination (b). The position of the two side components (c) is restricted by the same circle (dashed line) that defines the observable region. The observable region will thus contain, in addition to the normal (lower spatial frequency) information, moved information that originates in two (higher spatial frequency) offset regions (d). Multiple images are taken across different grating angles and phase positions (e). Adapted from Gustafsson et al. (*147*)

Structured-illumination microscopy (SIM) is a technique that utilises both widefield imaging and the illumination of a sample with a known pattern of excitation light (*155*). SIM has an advantage over other SRM techniques, as sample preparation is relatively simple and the acquisition time of SIM as a comparable imaging method is substantially shorter than localisation methods. Standard fluorophores can be used, no switching buffer is required and slides that are prepared for typical light microscopy can be imaged without any additional preparation. A series of images are recorded where the light pattern is moved along the sample laterally and rotated in a number of different angles (Figure 9). A SIM image is reconstructed using the higher frequency information gained from moiré fringes after imaging with structured light. By using an algorithm that carries out frequency shifting and deconvolution, high frequency information gained from moiré fringes can be extracted and a sectioned image with typically double the resolution in x,y and z can be produced (*154*). The maximum spatial frequency which the objective can transmit will, along with the wavelength of light used, determine the resolution of the system (*156*) and the improvement is typically double in the xy plane (around 100 nm) than that of diffraction-limited techniques (*147*).

3 Aims

This thesis focuses on investigating LROs, a group of organelles for which the relationship with each other, and function is still not fully understood. Two LROs were the main focus of this work, the WPBs of endothelial cells and platelet granules. This thesis has three key aims -

1. To investigate if the mutated genes that disrupt LRO function in HPS are also important to the biogenesis and function of WPBs in endothelial cells.

2. To develop an SRM-based methodology to image platelets that will significantly improve our ability to gather quantitative data about platelet granules as compared to current commonly used techniques.

3. To test whether SRM is a viable tool for diagnosing patients with a PSD.

4 Methods

4.1 Preparing Platelet and HUVEC cultures

4.1.1 Preparing HUVECs from primary stocks

HUVECs pooled from multiple donors (Lonza) were grown on 1% (w/v) porcine gelatin-coated 15 cm dishes (Nunc) at 37°C and 5% CO_2. For the preparation of working stocks, HUVECs were thawed onto 15 cm dishes coated with 1% (w/v) porcine gelatin (Sigma) and grown in TCS Large Vessel Endothelial Cell Basal Medium with Amphotericin B/Gentamycin medium. Confluent dishes were split 1:6 and maintained in HUVEC growth medium (HGM, Medium 199 (M199) with Earle's modified salts (GIBCO) 20% (v/v) foetal bovine serum (FCS, BioWest), 30 µg/ml endothelial cell growth supplement and 10 U/ml heparin (Sigma)). Confluent dishes were trypsinised and centrifuged at 1000 rpm for 3 minutes. The cell pellet was resuspended in FCS plus 10% (v/v) dimethyl sulphoxide (DMSO) and 1 ml aliquots of HUVEC suspension stored in cryotubes at -80°C before being transferred to liquid nitrogen after 24 hours for long-term use (usually 3-6 months). Working stocks were thawed at 37°C in a water bath and added to 1% (w/v) porcine gelatin coated dishes containing 30 ml of 37°C HGM. Dishes were incubated at 37°C and 5% CO_2. To try and ensure reproducibility, all HUVECs in this PhD were only passaged once before starting any experimental protocol, i.e. grown to confluency from a working stock without any further splitting, cells stocks would be mixed to reduce any effect of heterogeneity between vials if more than one vial was required.

4.1.2 Preparing platelets from platelet rich plasma (PRP)

Platelet preparation protocol adapted from discussion with and protocols from Holly Smith (Paul Gissen Lab LMCB) and phlebotomy training undertaken at UCL hospital. Acid Citrate Dextrose (ACD) and HEPES Tyrode's Buffer were first kept at 37°C before starting the platelet isolation. All volunteers from the LMCB department at UCL or patients from the Royal Free hospital had their blood

taken by myself, or a nurse, using the phlebotomy technique taught at UCL Hospital and the Royal Free Hospital. For the purpose of immunofluorescence studies the following steps were undertaken; using a syringe and vacutainer, blood was taken by venepuncture from the antecubital vein; if at first the venepuncture was unsuccessful the other arm was used. The first vacutainer was discarded to ensure the absence of tissue contaminants and following this the minimum amount of blood was taken that was required for the experiment. Each volunteer/patient's blood was taken with a minimum of three months between each sample taken. Blood was either taken into ACD containing vacutainers or 7 ml of whole blood was immediately transferred into a 10 ml Falcon tube containing 1 ml of ACD. Blood was then centrifuged at 180xg for 17 minutes and the PRP was collected using a 1 ml Pipette. The PRP was then left for 30 minutes at room temperature without any disturbance to minimise activation. After this the PRP was typically diluted at a concentration of 1:10, 1:50, 1:100 and 1:500 in HEPES Tyrode's buffer with 0.1% glucose and fixed with 4% Paraformaldehyde (PFA, TAAB Laboratories Equipment Ltd.) in PBS (phosphate buffered saline) at a final concentration of 4%. 10 minutes into the fixation the platelets were transferred to a 12 or 24 well dish containing Poly-L-Lysine coated coverslips and centrifuged at 600xg for 5 minutes in a Beckman-Coulter Allegra 6R at 4^{o}C. The remaining platelets and fixative were aspirated from each well, and without washing, fresh PBS was added to each well and the plate was left at 4^{o}C for at least 12 hours to allow the remaining platelets to further adhere. The coverslips were then removed from the dish and permeabilised with 0.2% TX-100 in PBS for 10 minutes. This was followed by incubation with primary and secondary antibodies (as described in 4.3.1) the samples were stored in the dark at 4^{o}C or imaged directly.

4.2 siRNA protocol

4.2.1 Nucleofection

For transient transfections, HUVECs were grown to confluency. Cells were rinsed with PBS and incubated with Trypsin‐EDTA (ethylenediaminetetraacetic acid)

for 3-5 minutes to lift cells. The trypsin was neutralised with HGM and the HUVECs counted using a ScepterTM automated cell counter and 60 µm sensors (Millipore). HUVECs were spun for 3 minutes at 1000 rpm and pelleted HUVECs were resuspended in nucleofection buffer at a concentration of 1 million cells per 100 µl. Nucleofection was performed using 200-1000 pmol of siRNA or 2-5 µg DNA construct and 100 µl cell suspension in a cuvette with an Amaxa Biosystems Nucleofector, program U - 001. Cells were immediately rescued after nucleofection with HGM and plated typically on 12 well plates (Nunc). The siRNA sequences used in this study are outlined below.

4.2.2 siRNA sequences

All sequences ordered from MWG Eurofins apart from Pallidin (Qiagen)

Table 2 siRNA sequences

No.		Target sequence 5' to 3'
0	*Luciferase* (Firefly)	CGUACGCGGAAUACUUCG
1	Pallidin	AAAAGTGCATGTACGGGAAAT
2	Pallidin 2	AACTGCAGCAGAAGAGGCAAA
3	Pallidin 3	AAGGAUUGCUUUCUCAUUAUU
4	Pallidin 4	GAAGGAGUUUGAAAGAGAA
5	HPS1.1	ACUAAGGUCUGGUCUCUGA
6	HPS1.2	CUUCCUGUAUGUCCUUCAC
7	HPS1.3	CTCCATGACGATGCTGGAGAA
8	HPS1.5	UGAAGUUCGGGCAGUCAGA

Figure 10 Gene locations targetted by siRNA sequences

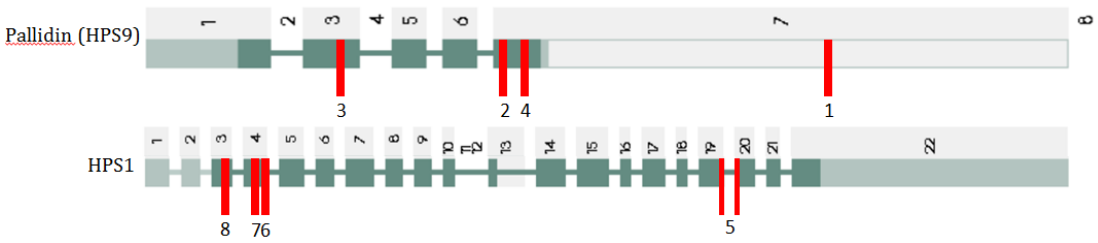

Gene structure for Pallidin (HPS9) and HPS1 with the location of the siRNAs (Table 2) used in this study. Numbers of siRNAs correspond to numbers in table 2.

4.3 Fluorescence Microscopy

4.3.1 Immunofluorescence microscopy

HUVECs were first permeabilised for 5 minutes using PBS/0.1% Triton with the cells ''face up'' sitting on a layer of Parafilm M® . PBS/0.1% Triton was aspirated using a glass pipette connected to a suction pump and blocked for up to 1 hour with filtered 2% BSA in PBS/0.1% Triton. Following this a primary antibody was added in 2% BSA/PBS/0.1% Triton for 45 minutes to 1 hour (50-100 µl per coverslip). After aspirating and washing 4 times with PBS/0.1% Triton the secondary antibody was added in 2% BSA/PBS/0.1% Triton for 45 minutes-1 hour at room temperature (50-100 µl per coverslip), secondary antibody was always added in a concentration of 1:500. Finally the secondary antibody solution was aspirated and cells were washed a further four times with PBS/0.1X Triton before mounting onto slides with around 3-10 µl of Prolong gold antifade solution and left to dry overnight at room temperature in the dark. The following day slides were transferred to a slide holder and kept at 4^{o}C until needed.

Table 3 Primary Antibodies used

Antigen	Raised in	Clone	Source	Dilution
vWF	Rabbit	Polyclonal	DAKO	1:10000
	Mouse	21-43	Serotec	1:500
	Sheep	Polyclonal	Serotec	1:1000
β Tubulin	Mouse	TUB2.1	Sigma	1:100
	Sheep	Polyclonal	Cytoskeleton	1:200
P-Selectin	Mouse	AK6	Serotec	1:100
	Sheep	Polyclonal	R&D Systems	1:100
CD63	Mouse	CLB 180	AbCam	1:100
TGN-46	Sheep	Polyclonal	Abcam	1:1000

Table 4 Secondary Antibodies used

Antibody	Raised in	Source	Dilution
Anti-rabbit-A488	Donkey	Invitrogen	1:500
Anti-rabbit-A568	Donkey	Invitrogen	1:500
Anti-rabbit-Cy5	Donkey	Jackson	1:500
Anti-mouse-A488	Donkey	Invitrogen	1:500
Anti-sheep-A488	Donkey	Invitrogen	1:500

For confocal imaging, cells were imaged on the Leica SPE3 or SP5 inverted confocal laser scanning microscope. All images within an experiment were acquired under the same laser conditions using a 63x objective, 1024 x 1024 pixel resolution and 1x zoom. Over 10 fields of view were typically taken per condition and images were analysed using Image J or Imaris software.

4.3.2 dSTORM

All dSTORM imaging was performed in collaboration with Dan Metcalf (National Physics Laboratory). Fluorescence and excitation lights were spectrally separated by a full multi-edge filter set (LF405/488/561/635-A-000, Semrock). A diode laser operating at 640 nm (iBeam smart, 150mW, Toptica Photonic AG) was fibre coupled, expanded and focused at the edge of the back focal plane of the objective (UAPON 100xOTIRF, NA=1.49). The beam size of the excitation laser was matched to the field of view of the imaging system limited by the detector chip size (16μm/pixel*512pixel). The power density of the excitation laser on the sample was approximately 2 kW/cm^2. For data acquisition, a ROI (128x128 pixels) was used. Image files of fluorophore "blinking" events (composed usually of around 20000 frames) were captured using a low-noise, highly sensitive electron-multiplying EMCCD camera (Andor iXon 897) at frames rates of 54 per second with 10 ms exposure times. The first 5000 frames were discounted to increase the chance of specific blinking events. The secondary antibodies Alexa 647 (for dSTORM imaging of CD63) and Alexa 488 (for widefield imaging of Tubulin) were used in a 1:500 dilution. Samples were imaged in a photo-switching buffer containing 50 μg/ml (5 units) glucose

oxidase, 1 μg/ml (40-60 units) catalase and 100 mM mercaptoethylamine-HCl (*157*). Images were reconstructed using the rainSTORM algorithm (*157*, *158*), software version 2-28, with super resolution pixel sizes of 20 nm. Mean localization precisions were around 25 nm, giving an estimated resolution limit of 50-60 nm (*159*). STORM data is displayed by histogram visualisation; i.e. accepted localisations were assigned to 20 nm pixels, each localisation corresponding to 1 grey scale intensity value. For clarity of viewing a "red hot" lookup table and a contrast enhancement were applied (0.01-0.1% pixel saturation) in ImageJ. dSTORM methodology from (*63*).

4.3.3 Structure Illumination Microscopy

All SIM imaging performed in collaboration with Mike Shaw (NPL). Imaging was carried out using an inverted widefield fluorescence microscope (IX71, Olympus) modified for SIM, as previously described (*160*, *161*). Each super resolution image was reconstructed from a sequence of raw images of the sample acquired under excitation with nine different sinusoidal illumination patterns as described (*154*). For comparison, widefield images were created by summing all nine raw images. Out of focus light in each image was suppressed by multiplication of the zero and first order SIM passbands by Gaussian and complementary inverted Gaussian functions (*161*). The two-colour images were acquired sequentially under excitation of the sample with laser light at 488 nm and 561 nm. Image *z*-stacks were obtained by axially translating the specimen in 0.2 μm steps using a piezoelectric translation stage (NanoScanZ, Prior Scientific).

4.4 Electron Microscopy

4.4.1 TEM imaging of sectioned platelets

All EM preparation performed in collaboration with Jemima Burden (Head of EM facility LMCB). PRP was prepared and an equal volume of 0.1% glutaraldehyde in 0.1 M Na cacodylate buffer added for 15 minutes at room temperature. Platelets were then spun at 1000xg for 6 minutes to pellet cells. The supernatant was

discarded and platelet pellet washed with 500µl Na cacodylate buffer. Supernatant removed and 3% glutaraldehyde added in Na cacodylate buffer. Platelets were incubated at 4°C for 30 minutes and then spun at 1000xg for 5 minutes. The supernatant was removed and 1% OsO_4 in 0.1M Na cacodylate buffer was added for 1 hour at 4°C. Platelets were then washed three times for 10 minutes with 0.1M Na cacodylate buffer. Samples then stored for a maximum of 5 days at 4°C if required. The pellet was then transferred into a 5 ml glass beaker. 70% EtOH was added for 10 minutes followed by addition of 80% EtOH for 10 minutes and 90% EtOH for 10 minutes, 96% EtOH for 10 minutes and finally three times with 100% EtOH for 10 minutes. Sample was covered with Epon and left for at least 2 hours at room temperature. The sample was then left to polymerise in the fume hood oven at 60°C for at least 3 days before sectioning using a Leica UCT ultramicrotome. Sections were collected on copper grids and imaged on a FEI T12 Tecnai Spirit with a SIS morada 11 megapixel digital camera.

4.4.2 TEM of platelets prepared by whole mount

All whole mount EM performed in collaboration with Jemima Burden (Head of EM facility LMCB). PRP was diluted in HEPES Tyrode's buffer and centrifuged at 600xg for 5 minutes in a Beckman Coulter Allegra 6R onto formvar coated mesh copper grids. The grids were washed twice in water, dried for 20 minutes and imaged directly by TEM without fixation (Tecnai Spirit, FEI). Images of whole mount platelets were randomised and counted by one analyst. All images were counted in one sitting to avoid variation in counting criteria.

Initial tests where neat concentrations of PRP were dropped on EM grids for around 5 seconds resulted in very few platelets attaching to the formvar grid. A considerable improvement in the concentration of platelets on the formvar grid was seen after centrifuging at 600xg. We subsequently used dilutions of 1:10, 1:20, 1:100 and 1:1000 (Figure 11) and the grid with the optimum density of platelets was selected and imaged.

Figure 11 Dilution Series of platelets after centrifugation on EM copper grids

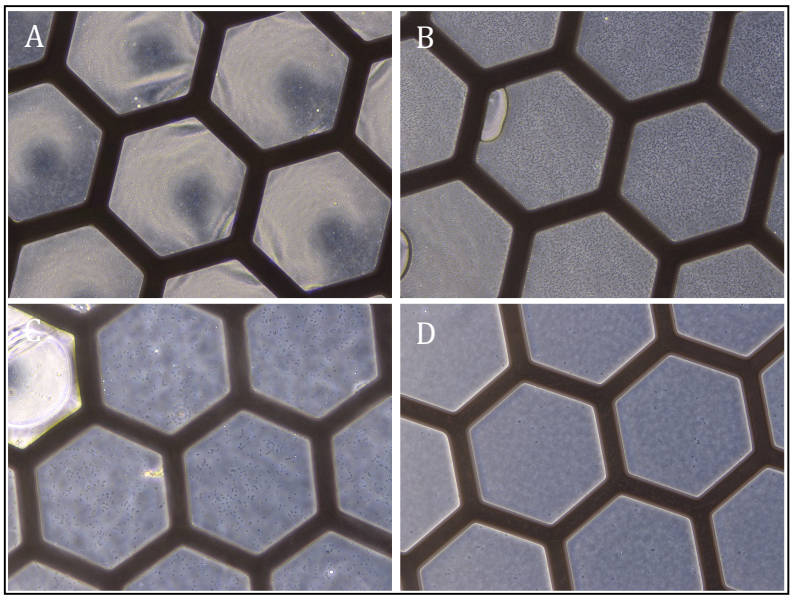

An improvement in analysing a larger number of platelets was achieved when platelets were centrifuged at 600g for 5 minutes in a Beckman Coulter Allegra 6R onto formvar coated mesh copper grids. Here, a dilution series is shown that enabled suitable working concentrations to be selected 1:10 (A), 1:20 (B), 1:100 (C) and 1:100 (D)

Images of platelets were then collected, and for the purpose of this study an extremely stringent criteria was used to analyse the images based on Hayward et al. (*162*). This was important as small differences in contrast could affect the counting of granules. Therefore, the only structures counted were large, dense and had a defined edge (see Figure 12 for an example of the criteria used); importantly alpha granules can look large but not as dense and have a less defined edge. I performed all the counting without knowledge of the origin of the platelets, in a full set of randomised images. An example of the criteria used is shown is shown below.

Figure 12 Whole mount EM counting criteria

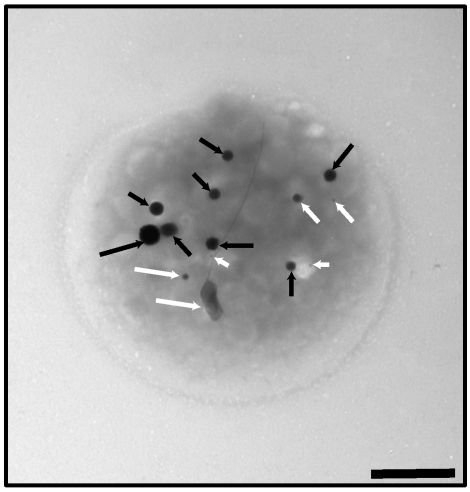

Whole mount EM of a control platelet demonstrating the counting criteria employed in this study. Only dense structures that were of a certain contrast with a defined structure and size were counted (black arrows). All counting was performed without knowledge of the origin of the platelet, in a full set of randomised images; stringent criteria were chosen, as there are many structures that resemble dense granules (white arrows) which were not counted but could affect the reliability of the results if included. Scale bars: 1 μm

To facilitate counting, the contrast of the image was manipulated to reveal dense granules from electron dense areas (Figure 13), this was performed by altering the brightness and contrast settings in ImageJ arbitrarily. As there is no immuno-labelling or segmentation of the image, this relies on the subjectivity of the individual.

Figure 13 Whole mount EM of platelets – manipulating contrast for counting

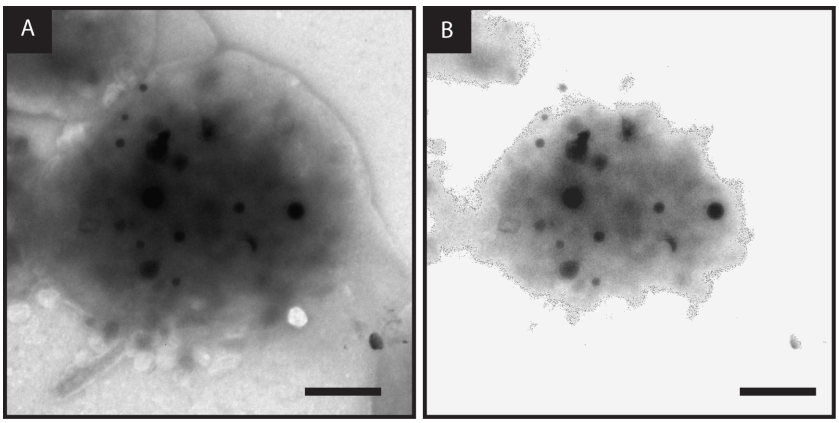

Two images demonstrating the advantage of changing the contrast and also the subjectivity required when counting dense granules in platelets. The original image (A) contains a few dense granules that are hidden by background electron density and are revealed when the contrast of the image was decreased (B). Scale bars 1 μm.

4.5 Image analysis studies

4.5.1 High throughput morphology of WPBs

All high throughput morphology analysis performed in collaboration with Janos Kriston-Vizi. Immunofluorescence prepared as in (4.3.1). Images were acquired using an Opera high-content screening system (Perkin Elmer) by using a 40X air objective (NA 0.6). At least eight wells per condition were analysed per experiment, with nine images per well. Maximum feret diameter of each vWF-positive object was measured. At least 10,000 vWF-positive structures were analysed (as in (*163*). A high performance bare-bone computer system equipped with 256 GB RAM and four dodeca-core CPUs running at 2.2 GHz, allowing parallelisation of computation was used for image processing. Image processing was performed using ImageJ. Flex format image files were converted to Tagged Image Format (TIF). The processing steps were executed as detailed in Ferraro et al. (*63*).

4.5.2 Automated image analysis of Platelet CD63 positive structures

An automated workflow written as an ImageJ macro in collaboration with William Grimes (see (*164*) for more detail) and was used to segment SIM images of CD63 granules and assign granules to their constituent platelets.

Platelets were segmented using the addition of the tubulin image to its corresponding CD63 image. Uneven background illumination was removed from this composite image using a rolling ball background subtraction with a radius of 20 pixels (*165*). Image noise was reduced with a Gaussian blurring with a sigma value not impacting the image resolution and finally a minimum error threshold was applied (*166*). The segmented tubulin-labelled structures in the binary image were filled and a watershed transform performed to separate touching platelets. To demarcate the interior of the platelet, the filled area was eroded to avoid any contribution of CD63 found at the platelet surface. Segmented structures with an area of less than 2.0 μm^2 (average diameter of platelets 2-3 μm (*167*), area ≥3.14 μm^2) or circularity (defined as $4\pi(\text{area}/\text{perimeter}^2)$ less

than 0.7 were removed (*168*), for the remaining foreground objects, morphometric measurements were taken.

Segmentation of CD63-positive structures for each of the seven control CD63 image data sets was performed according to a threshold value obtained from Moment-preserving thresholding (*169*). The three patient data threshold values were set according to control data that was acquired on the same day. Segmented CD63 granules that were overlapping were separated with a watershed transform and areas smaller than 0.01 μm^2 were considered background and removed (average diameter of dense granules 150 nm, area ≥ 0.018 nm^2). The platelet in which each CD63 granule was located was saved and morphometric features (including area) were measured.

4.5.3 CD63 distribution in platelets

CD63 distribution analysis performed in collaboration with William Grimes (see (*164*) for more detail). Platelets were selected with circularity > 0.85, this was in part to remove any platelets that were activated from the analyses but also to remove any tubulin-positive structures that had been incorrectly included. For the CD63 channel the radial profile plugin in ImageJ was used (*170*). The plugin creates concentric rings from the centre of the platelet (see Figure 49 for diagram) and in each ring calculates the normalised integrated density (the sum of pixel values in that ring divided by the number of pixels in the ring). From this it was possible to deduce a measure of both the distance from the centre and mean pixel intensity within each ring. In addition to this, the same radial profile information was generated for the tubulin channel, any radial integrated density values beyond that in the CD63 channel were removed from the data (these are considered to be outside the platelet). In order to compare spatial distributions across different segmented platelets, CD63 channel pixel values were normalised by the total integrated signal and the radial distance from the platelet centre was normalised to the maximum radius of the tubulin ring.

4.5.4 Exocytic site analysis

HUVECs were seeded and prepared for immunofluorescence as above. Before fixation, cells were prepared as for secretion assays (see 4.7.1), by washing three times with release media (RM). Cells were then stimulated with the desired secretagogue with a 1:1000 concentration of vWF rabbit primary antibody for 30 minutes in RM. The cells were then fixed with 4% PFA. Cells were prepared for immunofluorescence as above using a vWF sheep primary antibody at a concentration of 1:5000 to visualise total vWF. vWF at the cell surface was stained with a secondary anti-rabbit Alexa 647 antibody and total vWF stained with a secondary anti-sheep Alexa 488 antibody at a concentration of 1:500. Images were analysed in ImageJ as follows; a background subtraction was performed using a sliding paraboloid rolling ball analysis with a sensitivity of 1 pixel. A colocalised pixel map was then generated and exocytic sites identified by segmenting particles greater than 6 pixels and with circularity between 0.9-1.

4.5.5 Colocalisation study

To quantify colocalisation between fluorescent markers imaged using confocal microscopy, raw LIF files were analysed using ImarisColoc. The determination of intensities to include / exclude from the study, i.e. the threshold selection, was achieved by thresholding the source channels used in the analysis. This was performed by automatically selecting the thresholds to remove user bias, to do this ImarisColoc utilises the algorithms by Costes et. al (*171*) in the automatic colocalisation selection. ImarisColoc provides a number of statistical parameters, for this thesis the percentage colocalised and Pearson's correlation was used.

4.6 Molecular Biology

4.6.1 Primer design

Primer pairs were designed to be 18-25 nucleotides long, have a T_m of approximately 58^{o}C, have a G/C rich 5' end to assist annealing and to produce an amplicon of approximately 100-200 base pairs in length spanning an exon-exon

boundary to prevent amplification of genomic DNA. To identify exon/exon boundaries, gene sequences were obtained from http://www.NCBI.nlm.nih.gov /CCDS whilst http://www.basic.northwestern.edu/biotools/oligocalc.html was used to check for potential hairpin loops and primer dimers. Primers were ordered from MWG Eurofins. Successful sequences used in this study are listed below. Upon arrival, DNA was dissolved in sterile, RNase-free HPLC ultrapure water (Alfa Aesar) at a concentration of 100 µM and frozen at -20°C. (*68*).

4.6.2 RNA extraction

Cells were grown to 90-100% confluency and RNA extracted 24-48 hours post transfection using a QIAGEN RNeasy purification kit and a QIAGEN QIAshredder kit according to the manufacturer's instructions. cDNA was generated using an Invitrogen SuperScript™ III First Strand Synthesis System according to the manufacturer's instructions and DNA concentration measured by optical density at $Abs_{260/280}$ using a NanoDrop (LabTech, ND1000 spectrophotometer) and ND1000 v3.3 software. RNA and cDNA was frozen at -20°C. All steps were carried out on ice.

4.6.3 Reverse transcription

RNA was reverse transcribed using the SuperScript™ III First-Strand Synthesis System for RT-PCR (Invitrogen). 10µl of RNA was used for each reaction and random hexamers are used as primers in this reaction to ensure total DNA amplification. Incubation times were according to manufacturer's instruction.

4.6.4 qPCR

A DyNAmo™ SYBER© Green (quantitative polymerase chain reaction) kit (Thermoscientific) containing *T. brockianus* DNA polymerase, SYBER Green I dye, optimised PCR buffer, 5 mM $MgCl_2$ and dNTP mix including dUTP was used to quantify relative gene expression between samples. Sample cDNA was diluted to 150 ng/µl and a primer master mix generated with both forward and reverse primers present at a concentration of 1.2 µM, diluted in HPLC Ultrapure

RNase-free water. All reagents were prepared on ice. Each reaction was set up containing 6.25 µl 150ng/µl cDNA, 6.25µl 1.2µM primer pair master mix and 12.5 µl SyberGreen per well of a 96 well PCR plate (Star Lab). All reactions were carried out in triplicate and, for each sample used, amplification of actin mRNA was used as a housekeeping gene control. For each primer pair used, a no DNA control was also included. Plates were loaded on an Eppendorf Mastercycler® epGradient thermocycler and the PCR programme set up using Realplex software. Initially, plates were incubated at 95°C for 10 minutes to free up DNA binding sites and activate the SyberGreen. Reactions then progressed through 40 cycles of a 10 second melting step at 95°C, 15 seconds annealing at 53-57°C (5°C lower than primer T_m) and 15 seconds at 72°C to copy strands. In all cases, a melting curve was also generated using the final product with a maximum temperature of 95°C to check the specificity of amplification. The $2^{-\Delta\Delta C(t)}$ method (described (*172*)) was used to calculate expression levels of a gene of interest relative to actin mRNA levels by comparing the cycle number (C(t)) at which PCR product increases exponentially. The equations used are as follows;

ΔC(t) gene of interest = transfected sample C(t) – Mock C(t)

ΔC(t) housekeeping gene = transfected sample C(t) – Mock C(t)

ΔΔC(t) = ΔC(t) gene of interest -ΔC(t) housekeeping

Expression relative to mock = $2^{-\Delta\Delta C(t)}$

Method described as in (*68*), the gene specific primer sequences are detailed below;

Table 5 Gene Specific Primers sequences

Target Primer	Primer Sequences 5' to 3'
Actin forward	TGGTGGTGAAGCTGTAGCC
Actin reverse	GCGAGAAGATGACCCAGAT
Muted	Quantitech Primer assay QT00026831
Snapin forward	ATGAGGATAGAAGGTGGCC
Snapin reverse	ATTCCCGAATCCAGCATTGC
Pallidin forward	GCTTCTTCCCTGTGTTCCCA
Pallidin reverse	AGTGTCACTTAAACCAGGCGT
HPS1 forward	CCACAGTGCCAGCTCCCTGC
HPS1 reverse	GTCTGTCTCCTGAATGTCGT
HPS4 forward	GACAAGGTCTCTAGCATCTCCAGC
HPS4 reverse	GTTCTCCTTCCTGCCATCTG

4.7 Biochemistry

4.7.1 vWF secretion assay

After HUVECs were washed three times to remove any residual dead cells, the cells were left for 30 minutes before HGM was aspirated and gently washed three times with Release Media, RM (500 ml M199, 5 ml 1M HEPES Tyrode's buffer + 950 mg BSA , filtered with 0.2 µm filter). Cells were left for 15 minutes before one last gentle wash with RM, which was aspirated and 500 µl of RM added to each well for 60 minutes to measure constitutive secretion. Media was collected and cells incubated in RM with either histamine (100 µM histamine (Sigma-Aldrich) or phorbol 12-myristate 13-acetate (PMA, 100 ng/mL Sigma-Aldrich) for 30 minutes. Following this, media was collected and cells lysed in lysis buffer (10ml RM + 50µl TritonX100 + 20 µl protease inhibitor cocktail) on ice for 30 minutes. All samples were subsequently centrifuged at 10,000 rpm for 5 minutes and the supernatant transferred to new eppendorf tubes and stored at -20^{o}C.

For the purpose of this thesis the results gained are displayed from measuring the percentage of regulated secretion; any contribution to vWF secretion by the constitutive (vWF from non-WPB anterograde carriers) and basal pathways

(vWF secreted from WPBs that is independent of secretagogue) was removed by taking a baseline before any secretagogue was added (see 4.7.1). No significant difference in levels of vWF basal/constitutive secretion in any of the ablation studies was observed; however, the levels of basal/constitutive secretion are often relatively small and thus an ELISA-based secretion assay is often not sensitive enough to identify subtle changes.

The mock or *luciferase* control siRNA was always taken from the same vial of cells (after reaching confluency), if more than a vial was required, then multiple vials were mixed before the first nucleofection. HUVECs were counted and plated at the same density and HUVECs treated with the siRNA of interest were always plated within the same 12 well plates as the control to maintain consistency. All experiments were performed with cells taken without any further passaging from frozen stocks. Two rounds of siRNA treatment were performed, and the secretion assays and siRNA treatments were performed in the same intervals after initial transfection of the siRNA.

vWF secretion from WPBs in HUVECs has a number of contributory factors that can impact the consistency of results within and between experiments, including plate handling, cell confluency and inherent variability within primary cell stocks. Results demonstrated by Howell et al. (*173*) and unpublished analyses in the Cutler lab has shown that confluency will affect the number of WPBs per cell and subsequently the amount of vWF secreted from each cell, therefore, HUVEC confluency was carefully regulated by maintaining the same cell number between samples after each passage and nucleofection.

4.7.2 vWF ELISA

MaxiSorp plates (Thermo Fisher Scientific) were incubated with Rabbit anti-vWF antibody at a concentration of 1:600 in 50 µl of PBS for 1hr RT shaking (or 4^{o}C overnight). The antibody solution was then aspirated and 2X TXEB (0.4% Fish skin gelatine, 4% pH 8.0 EDTA and 10% Triton X100 in PBS) was added to block the plate for at least 1hr RT shaking (or 4^{o}C overnight). Wells were then washed

three times with 1X TXEB (dilute 2X TXEB in PBS). 200 µl of sample was added to each well in duplicates originating from triplicate (or quadruplicate) samples for each condition from a 12 well plate. Sample dilutions were prepared as follows; Constitutive secretion – neat, Regulated Secretion – 1:3 for PMA secretion and 1:2 Histamine secretion and Lysates – 1:10. A 1:2 serial dilution of human plasma diluted in 1x TXEB was also present on plates to provide a concentration standard, in addition to a 1x TXEB 'blank'. Samples were left for 1 hour at room temperature shaking (or 4^{o}C overnight). The wells were then washed three times with 1X TXEB and incubated with 100 µl of secondary antibody rabbit vWF-HRP conjugated at a concentration of 1:1000 in 1X TXEB for 1 hour at room temperature shaking. The wells were subsequently washed three times in 1X TXEB and washed twice in PBS before adding 200 µl of development solution (7.43 ml 100 mM citric sodium monohydrate, 14.56 ml 200 mM dibasic sodium phosphate, 22 µl Hydrogen peroxide, 132 µl o-phenylene-diamine (OPD) saturate in methanol). A kinetic ELISA was used, measuring absorbance at 450 nm and reading every 30 seconds and shaking just before each measurement for 30 minutes. Values for regulated secretion were calculated as a percentage of total secretion (constitutive and basal secretion was removed to give only the vWF secreted by regulated secretion).

4.7.3 Multimer gel analysis

To prepare 1.4% 1.5 mm agarose gels, high gelling temperature SeaKem® HGT agarose was dissolved in Tris/glycine buffer (200 mM Tris, 0.1 M glycine, 0.1% (w/v) SDS pH 9) and poured for use in Bio-Rad Mini Protean IIITM tanks, without a separate stacking gel, with a 10 well comb. Gels were refrigerated for at least an hour prior to use. Secretion assay samples were concentrated using a viva500 filter column, spun for 8 minutes at 13000 rpm to collect proteins larger than 100 kDa, and then diluted in sample buffer (20 mM Tris, 1 mM EDTA pH8.0, 2% (w/v) SDS, 8M urea and 0.01-0.02% (v/v) bromophenol blue). To provide a vWF standard, human serum was diluted 1:200 in sample buffer. All samples were then heated to 60^{o}C for 30 minutes prior to loading. Gels were run at 60V for 20 minutes then 40 V for several hours on ice using SDS-PAGE running buffer

(National Diagnostics). To improve efficiency, transfer gels were washed in 1 mM β-mercaptoethanol in PBS for 10 minutes prior to transfer. Gels were sandwiched between 4 pieces of Whatmann 3M filter paper and a layer of protran nitrocellulose transfer membrane, all soaked in transfer buffer (25 mM Tris-HCl, 192 mM glycine, and 10% (v/v) methanol, pH 8.3) and pressed to remove air. This was transferred to a Bio-Rad mini-trans blot cell wet transfer system and 10 V applied overnight at 4°C. The membrane was then blocked in 5% (w/v) milk powder, dissolved in PBS-0.2% (v/v) Tween®, overnight at 4°C. Blots were stained for one hour with Primary antibody, vWF primary antibody (DAKO, 1:5000) diluted in block, with agitation. Antibody was washed using two rapid washes with PBS then two washes for 15 minutes with PBS-0.2% (v/v) Tween. The membrane was then incubated with HRP-conjugated secondary antibody, donkey anti-sheep HRP conjugated secondary antibody (1:5000, diluted in block for 1 hour with agitation and washed as for primary). Antibody was detected using Luminata crescendo Western HRP substrate (Millipore) and exposed onto film (Amersham Hyperfilm™, GE Healthcare) using the X-OGRAPH compact X4 imaging system. (Method from (*68*))

4.8 Patients

4.8.1 Exome sequencing of HPS patients

Genetic analysis was performed by exome sequencing on the ThromboGenomics platform that includes HPS1-9 (see below). The results from this were given with the patients' permission by Dr. Keith Gomez (Royal Free Hospital).

Figure 14 Patient 1 HPS1 mutations

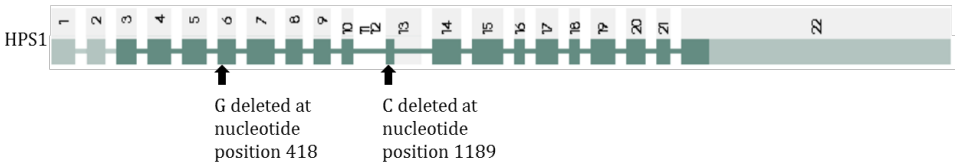

Patient 1 has a compound heterozygosity for two single nucleotide deletions resulting in frameshifts and introducing premature stop codons in the HPS1 gene: c.418delG and c.1189delC predicted to result in p.A140Rfs*34 and p.Q397Sfs*1. Human HPS1 gene consists of 22 Exons (green boxes) and 2103 Amino Acids. Gene structure adapted from (*174*, *175*)

Figure 15 Patient 2 HPS6 mutations

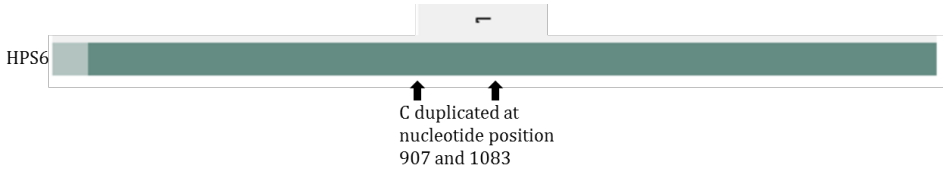

Patient 2 has a compound heterozygosity for two single nucleotide duplications resulting in frameshifts and introducing premature stop codons in the HPS6 gene: c.907dupC and c.1083dupC predicted to result in p.T303Hfs*64 and p.G362Rfs*5. Human HPS6 gene consists of 1 Exon (green box) and 2329 Amino Acids. Gene structure adapted from (*174*, *175*)

Figure 16 Patient 3 HPS5 mutation

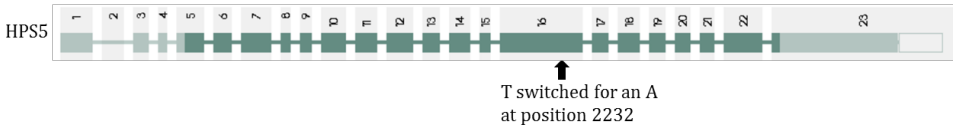

Patient 3 has homozygosity for a single nucleotide change introducing premature stop codons in the HPS5 gene: c.2232T>A predicted to result in p.Cys744Ter. Human HPS5 gene consists of 23 Exons (green boxes) and 3390 Amino Acids. Gene structure adapted from (*174*, *175*)

4.8.2 Controls and HPS patients for platelet studies

Controls were healthy volunteers. The relevant UK research ethics committee approved this work and all participants gave their written informed consent.

5 Chapter 1 Are genes associated with HPS important for WPB function?

5.1 Introduction

The LROs have historically been studied due to their specialist function. However, more recently the discovery that single mutations can affect a number of LROs concurrently has led to a renewed interest in the machinery that is common amongst this group (*1–3*, *110*, *176*, *177*). The grouping of these specialised secretory organelles was facilitated by the observation that a number of genetic disorders (and coat colour mouse models (*34*)) display symptoms that can be attributed to defects in more than one LRO. An example of this is HPS (see 2.5.2), where patients suffer from symptoms such as albinism, lung fibrosis and a bleeding disorder; all of which have or could be attributed to defective biogenesis and maturation of these specialised secretory organelles (*2*, *37*). Investigations into the functions of HPS-causative genes have revealed a number of important complexes in LRO biogenesis, such as the BLOCs (see 2.5). However, since this work largely began by studying the coat colour mouse models, most of the research has been focused on the roles of HPS-associated genes in melanosome biogenesis and trafficking (*1*, *4*, *15*, *34*, *110*, *178*). Consequently, the importance of these complexes in other LROs, such as WPBs, is yet to be determined.

The observation that LROs are related has been confirmed by the fact that single mutations in individual HPS proteins have been shown to have effects on a number of LROs. This highlights the importance of studying the effects of these mutations on the whole range of LROs, as they have been found to be responsible for similar functions in different cell types. For example, AP-3, a HPS-related protein complex has been demonstrated to be important in the delivery of cargo to a number of LROs (*9*) including; OCA2 to melanosomes (*8*, *179*) , TLR4 to phagosomes in conventional dendritic cells (*180*), CD63 to WPBs (*74*), toll-like

receptor 9 to an IRF7-signalling LRO in plasmacytoid dendritic cells (*181*) and SLC35D3 likely to dense granules in platelets (*182*). AP-3 is also required for the biogenesis of eye pigment granules in *Drosophila melanogaster* and gut granules in *Caenorhabditis elegans* (*9*). Likewise, the HPS related protein Rab27a (see 2.6.2) is important for the exocytosis of multiple LROs including lytic granules, WPBs and melanosomes (*176*). However, there have been only a few examples of the effects of these mutations demonstrated in human cells (*127*, *183*) and the role of HPS-related proteins, though suspected, is yet to be investigated in a number of LROs.

One of the symptoms attributed to HPS is a bleeding disorder and this has been attributed to the genetic malformation of platelets and their granules (*184*, *185*). However, little is known about the role of WPBs and it is even unclear if they have a role in the bleeding phenotype seen in HPS patients. The lack of information in this area is surprising, given that quantitative and/or qualitative deficiencies in the secreted vWF multimers that are stored in WPBs lead to the most common bleeding disorder in humans, von Willebrand's disease (*63*). It was hypothesised that if HPS-associated proteins and complexes were important for the biogenesis of LROs and the secretion of LRO-related content, then they were likely to have an important role in the secretion of vWF from WPBs. In fact a common finding in the literature focused on HPS KD/KO mouse model cell studies has been the aberrant secretion of proteins that are carried by LROs; skin cells in HPS4 mice have been shown to have decreased basal secretion of lysosomal hydrolases (*186*), platelets from seven HPS mouse pigment mutants have abnormal thrombin-stimulated secretion of Serotonin, B-Glucuronidase and B-Galactosidase (*187*) and lamellar Bodies in lung alveolar type II epithelial cells in HPS1 and AP-3 mice have decreased basal and ATP-stimulated secretory capacity for surfactant protein and phospholipids (*188*). The secretion of vWF is in part reliant on microtubules that are required for the transport of WPBs from the perinuclear region to the cell periphery and have a role in the exocytosis of vWF (*73*, *80*, *81*). HPS1 mouse models have demonstrated defective microtubule-mediated organelle motility in lysosomes in fibroblasts (*121*) and HPS2 mouse

models have shown defective microtubule-mediated organelle motility for lytic granules in T cells (*189*).

Since there are instances of proteins associated with LRO biogenesis performing similar functions in different cell types and with different LROs, it is likely that HPS-associated proteins may perform important roles in WPB biogenesis and exocytosis. Whilst defects in patient platelets have been described, there may be an as yet undiscovered defect in endothelial cell function (as a result of defects in WPB biogenesis or exocytosis) in these patients, which could contribute to this bleeding phenotype. The aim in this chapter, therefore, is to determine whether the HPS-associated genes, which encode proteins that form the complexes BLOC-1 and BLOC-3 also have a role in the biogenesis of WPBs.

BLOC-1 deficient fibroblasts (obtained from *pallid* mice) have an increased surface accumulation of CD63 (*114*), a protein also found on the membrane of WPBs and other LROs such as melanosomes. BLOC-1 has also been shown to be located at tubular early endosomes that are in close proximity to the TGN, the site at which WPBs are formed (*63*). Mouse mutants that cause BLOC-1 or AP-3 deficiencies affect the targeting of PI4KIIα (also LAMP1 and VAMP7-TI) (*114*) and a siRNA ablation of *PI4KIIα* in HUVECs has been shown to lead to the formation of small, round, abnormally formed WPBs (*163*). *PI4KIIα* ablation does not affect the secretion of vWF but was shown to have an important role in the recruitment of AP-1 to the TGN as well for WPB maturation with a higher prevalence of lower molecular weight multimers.

A method in this chapter employed to destabilise BLOC-1 used an siRNA targeted to the mRNA of *pallidin* that is translated to form pallidin a member of the BLOC-1 complex. The pallidin protein is 20KDa in size with no homology to any known protein, and *pallidin* siRNA has been shown previously to be sufficient to destabilise the entire BLOC-1 complex and has been used as a tool to KD BLOC-1 function in the cell (*111*, *120*). The *pallidin* mutation in humans is known as HPS 9, and it's importance for the stability of the entire complex is highlighted as in a HPS 9 patient undetectable levels of pallidin were found and it was shown that

two other members of the BLOC-1 complex were also affected by its reduction. Cappuccino was undetectable and snapin was significantly reduced (*190*). Pallidin contains two highly alpha-helical coiled-coil regions which have been shown to be essential to binding to itself and to the SNARE, syntaxin 13 (*106*, *190*, *191*). Prekeris et al. (*192*) demonstrated using a transferrin recycling assay in permeabilised PC12 cells that syntaxin 13 is directly involved in the recycling of plasma membrane proteins and significant reduction in syntaxin 13 is seen in HPS 9 patient fibroblasts (*190*). Syntaxin 13 has also been shown to be involved with VAMP3 and SNAP23 dependent secretion of matrix metalloproteinases (*193*).

The BLOC-3 complex (comprising of HPS1 and HPS4) and its role in the biogenesis of LROs has yet to be elucidated. BLOC-3 is a guanine nucleotide exchange factor for the cell type-restricted rab GTPases RAB32 and RAB38, both of which have been implicated in the biogenesis of melanosomes and other LROs (*119*, *194–197*). Since the experiments in this thesis were completed, BLOC-3 has also been shown to have an important role in VAMP7 recycling, a v-SNARE that mediates fusion of melanosomes with tubular transport carriers that also carry the cargo protein TYRP1 and that require BLOC-1 for their formation (*198*)

5.1.1 Methodology employed

The secretion assay is an ideal tool to screen for WPB function, as levels of vWF released give an indication of WPB numbers and responsiveness, as well as the efficiency of exocytic machinery (*69*). As a suitable readout, the values of vWF secreted were calculated as a percentage of the total vWF measured within that sample (collected using a lysis buffer) as an internal control, and the basal/constitutive secretion (measured before secretion) was deducted from the stimulated secretion. The final value was divided by the control to give an indication of whether vWF regulated secretion was proportionally impaired (below 1) or increased (above 1). If the final value given (as in Table 6) was, for example 1.2, this would indicate that vWF secretion had increased by 20% as a proportion of the total vWF within that sample, compared to the amount of vWF

secreted as a proportion of total vWF secreted in the control under the same conditions; 0.8 would indicate a 20% reduction (see 4.7.1 for method).

Once an aberrant secretory phenotype was established, the next step was to identify if the formation of WPBs and the exocytosis and multimeric state of vWF was affected. The aim of this was to narrow down the stage at which the HPS-related protein of interest was acting.

To assess if the formation of WPBs had been affected, the size of the organelles was measured by their feret diameter using fluorescent microscopy and a morphometric analysis. Endothelial cell flatness forces WPBs to orient parallel to the substrate, this spatial constraint ensures that WPB lengths measured from 2D confocal images are a good approximation of actual organelle lengths (*63*). This method (see 4.5.1) was employed as WPB size, which is dictated by the general architecture of the Golgi apparatus (*63*), has been shown to be important in modulating the size of platelet-decorated vWF strings on the endothelial surface (*63*) and the adhesive activity of its vWF cargo (*199*).

To quantify if there was an effect on vWF exocytosis, the number of exocytic sites at the cell membrane was measured using an assay where HUVECs were incubated and subsequently labelled with a vWF antibody before and after fixation, the colocalisation of the two antibodies was used as a readout for the number of exocytic sites present at the cell surface after stimulation with a secretagogue (see 4.5.4 for method).

vWF multimers were analysed as the multimeric form of secreted vWF largely dictates its haemostatic efficacy, due to the fact that higher molecular weight vWF multimers have a higher binding affinity for platelets during haemostasis (*200*). A loss of high molecular weight vWF multimers has been associated with haemorrhagic disorders such as gastrointestinal bleeding, epistaxis or increased bleeding after dental procedures (*201–203*). To measure the multimeric state of vWF, multimer gels of secreted vWF were performed and analysed (see 4.7.3 for method).

5.2 Results - A potential role for BLOC-1 in WPB function

Previous work to investigate a potential role for BLOC-1 in WPB function used three siRNAs (against *muted*, *pallidin* and *snapin*) to target the complex in human embryonic kidney cells 293 (HEK293). As the levels of vWF secreted give an indication of WPB numbers and responsiveness to a secretagogue (and therefore the efficiency of exocytic machinery) the release of vWF in response to the secretagogue PMA was measured. The siRNA ablation of BLOC-1 complex proteins demonstrated a strong reduction in the amount of vWF released in response to PMA (Figure 17, unpublished data Tom Nightingale), it was concluded that 'BLOC-1 must play an important, but as yet undescribed role, in the biogenesis of WPB'.

Figure 17 BLOC-1 KD in HEK293 cells - vWF secretion assay

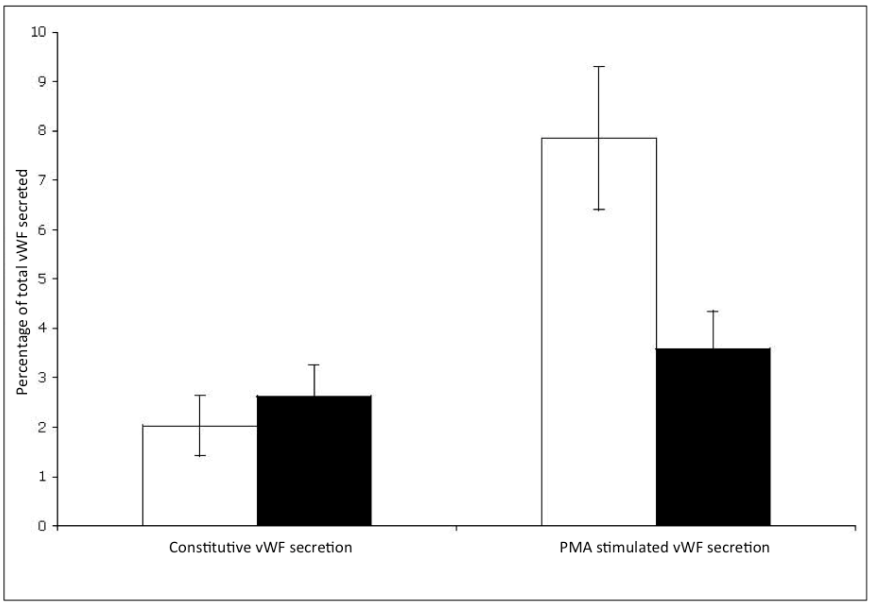

HEK 293 cells were either mock transfected or simultaneously depleted of three components of BLOC-1 (snapin, pallidin and muted) and cells stimulated with PMA. The amount of vWF released constitutively (cons) and in response to PMA (PMA stim) was calculated as a percentage of total vWF from control (white bars) and KD (black bars) cells. Experiment performed by and reproduced with permission from Tom Nightingale. Error bars are standard deviation. Figure adapted from Helen Zenner's PhD Thesis (October 2007).

5.2.1 vWF secretion assays in HUVECs depleted of BLOC-1

The secretion of vWF from BLOC-1 depleted cells was previously measured in HEK293 cells (see Figure 17), transient transfection of HEK293 cells with wild-type human vWF cDNA leads to the formation of numerous elongated organelles that very closely resemble WPBs. These "pseudo-WPBs" exhibit the internal structure, as well as the ability to recruit membrane proteins including P-selectin, of bona fide WPBs and have been used to study WPB biogenesis and function (*204*). To investigate a potential role for BLOC-1 in primary endothelial cells, which produce WPBs (and therefore remove the need to overexpress vWF), HUVECs were used and the BLOC-1 complex proteins depleted as a three. As no reliable antibodies against BLOC-1 complex proteins exist an indication of the efficiency of the KDs was provided by a Quantitative Polymerase Chain Reaction (qPCR) to measure the extent of reduction in the mRNA encoding the target protein.

Figure 18 BLOC-1 KD HUVECs – 100 pmol of siRNA - vWF secretion assay

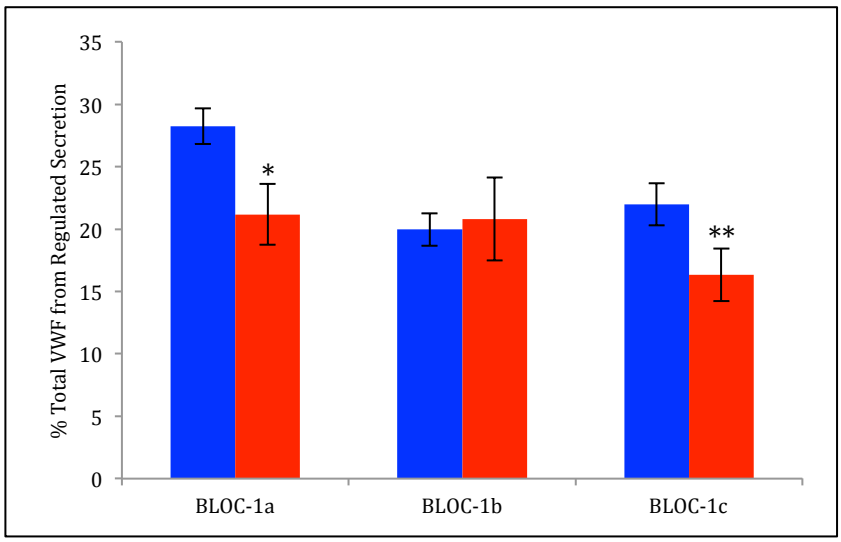

Three vWF secretion assays (three repeats termed BLOC-1a, BLOC-1b and BLOC-1c) measuring the percentage of vWF secreted over 30 minutes from HUVECs stimulated with 100 ng/mL of PMA. Mock nucleofected HUVECs used as a control (Blue) and BLOC-1 siRNA ablated HUVECs (Red) treated with 100 pmol of *pallidin*, *muted* and *snapin* siRNA. Mean percentage release is shown derived from four replicates per experiment. Error bars are standard deviation. T-Test used to measure significance, *; $p<0.05$, **; $p<0.01$.

Table 6 BLOC-1 KD in HUVECs – 100 pmol of siRNA

		vWF secretion		
siRNA	**mRNA remaining**	**Control**	**BLOC-1 KD**	**Fold change from control**
BLOC-1a	M. 10% P. 40% S. 40%	28%	21%	0.78
BLOC-1b	M. 35% P. 60% S. 75%	20%	21%	1.05
BLOC-1c	M. 10% P. 42% S. 38%	22%	16%	0.75

Table of results from Figure 18, three vWF secretion assay repeats (termed BLOC-1a, BLOC-1b and BLOC-1c) measuring the percentage of vWF secreted in 30 minutes from experiments shown in Figure 18. *Luciferase* (Ct) siRNA and *muted* (M) *pallidin* (P) and *snapin* (S) siRNA KD efficiency measured by qPCR in parallel with the secretion assay – mean of three qPCR measurements taken from pooled lysates from 2 confluent wells of HUVECs from a 12 well plate.

Two out of the three of these initial secretion assay repeats did display a significant secretory defect (repeat BLOC-1a and BLOC-1c), though less than previously observed in HEK293 cells (22-25% decrease as opposed to the 60% decrease seen initially). It was hypothesised that this may be due to a relatively poor KD efficiency (Table 6). A qPCR of the cell lysates was performed to determine the percentage of *muted, pallidin* and *snapin* mRNA silenced by the siRNAs (levels compared to the Mock control). The percentage fall in secretion of vWF in BLOC-1-depleted cells appeared to correlate with the degree of BLOC-1 KD. In order to improve KD efficiency the level of siRNA was increased to 200 pmol for each siRNA.

Figure 19 BLOC-1 KD HUVECs – 200 pmol of siRNA - vWF secretion assay

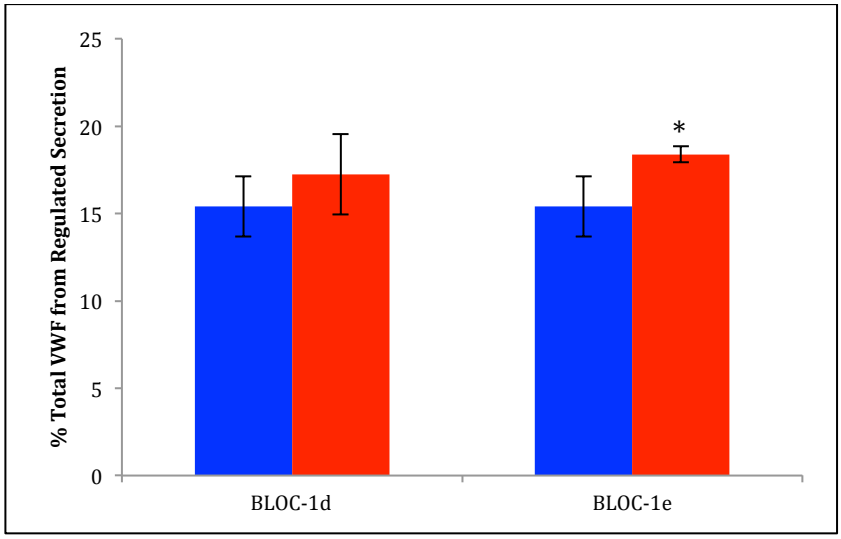

Two vWF secretion assays (repeats termed BLOC-1d and BLOC-1e) measuring the percentage of vWF secreted in 30 minutes by regulated secretion from HUVECs when stimulated with 100 ng/mL of PMA. Mock nucleofected HUVECs used as a control (Blue) and BLOC-1 siRNA ablated HUVECs (Red) treated with 200 pmol of *pallidin*, *muted* and *snapin* siRNA. Error bars are standard deviation. T-Test used to measure significance, *; $p<0.05$

Table 7 BLOC-1 KD in HUVECs – 200 pmol of siRNA

		vWF secretion		
siRNA	**mRNA remaining**	**Control**	**BLOC-1 KD**	**Fold Change from Control**
BLOC-1d	M. 35% P. 59% S. 77%	15%	17%	1.15
BLOC-1e	M. 36% P. 61% S. 73%	15%	18%	1.23

Table of results from Figure 19, two vWF secretion assays repeats (termed BLOC-1d and BLOC-1e) measuring the percentage of vWF secreted in 30 minutes as above. *Luciferase* (Control) siRNA and *muted* (M) *pallidin* (P) and *snapin* (S) siRNA KD efficiency measured by qPCR in parallel with the secretion assay – mean of three qPCR measurements taken from pooled lysates from 2 confluent wells of HUVECs from a 12 well plate.

The KD efficiency as determined by qPCR did not improve after increasing the amount of siRNA from 100 to 200 pmol. Unexpectedly, the regulated secretion of vWF by PMA in BLOC-1 KD cells actually increased (1.15 to 1.23 fold change compared to mock transfection (Figure 19 and Table 7). Therefore, after confirming that the KD achieved was not reproducible, or efficient enough, a different approach was taken. It was hypothesised that using lower concentrations (100-200 pmol) of three siRNAs was limiting the effect of the KD, also the effect of the KD was difficult to quantify as using three siRNAs may be introducing the potential of contrasting off-target effects. The literature had shown that only one siRNA targeted towards *pallidin* is sufficient to destabilise the entire BLOC-1 complex (*111*, *120*). Therefore, a new *pallidin* siRNA was

designed termed Pallidin 2 and used alone in an attempt to improve KD efficiency.

Figure 20 Pallidin 2 siRNA quantification

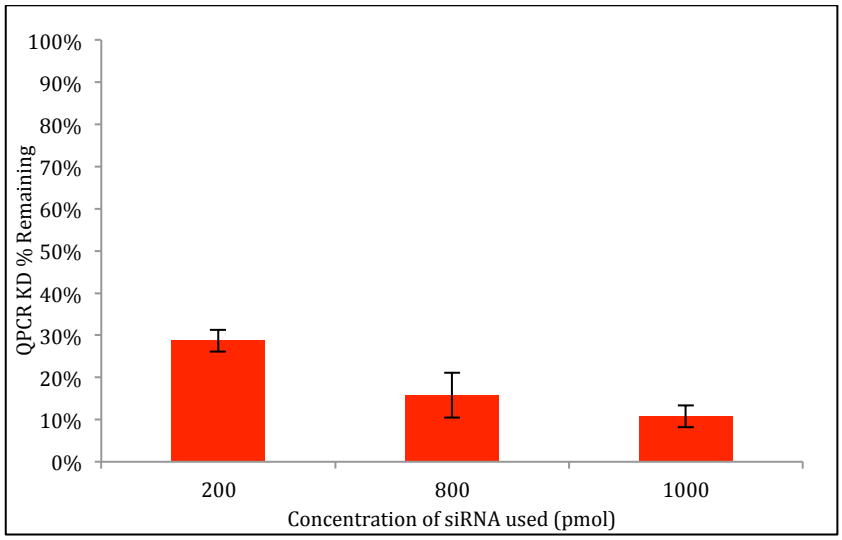

The percentage of *pallidin* mRNA after 200, 800 and 1000 pmol of Pallidin 2 siRNA treatment in HUVECs compared to *luciferase* siRNA treated HUVECs. Standard deviation is from three qPCR plate readings - mean of three qPCR measurements taken from pooled lysates from 2 confluent wells of HUVECs from a 12 well plate

A qPCR was performed of Pallidin 2 KD to measure efficiency with a series of siRNA dilutions (Figure 20) and it was determined that 1000 pmol of siRNA was producing the most efficient reduction of mRNA. The effect of Pallidin 2 siRNA (using 1000 pmol) on vWF secretion was then tested. The more physiologically relevant secretagogue, histamine was used to stimulate cells instead of PMA (Figure 17). A significant increase in the secretion of vWF was observed over three secretion assays (1.6-2.5 fold change from the control) and an efficient KD of *pallidin* by qPCR of 85% or more was achieved in each (Table 8).

Figure 21 Pallidin 2 KD in HUVECs - vWF secretion assay

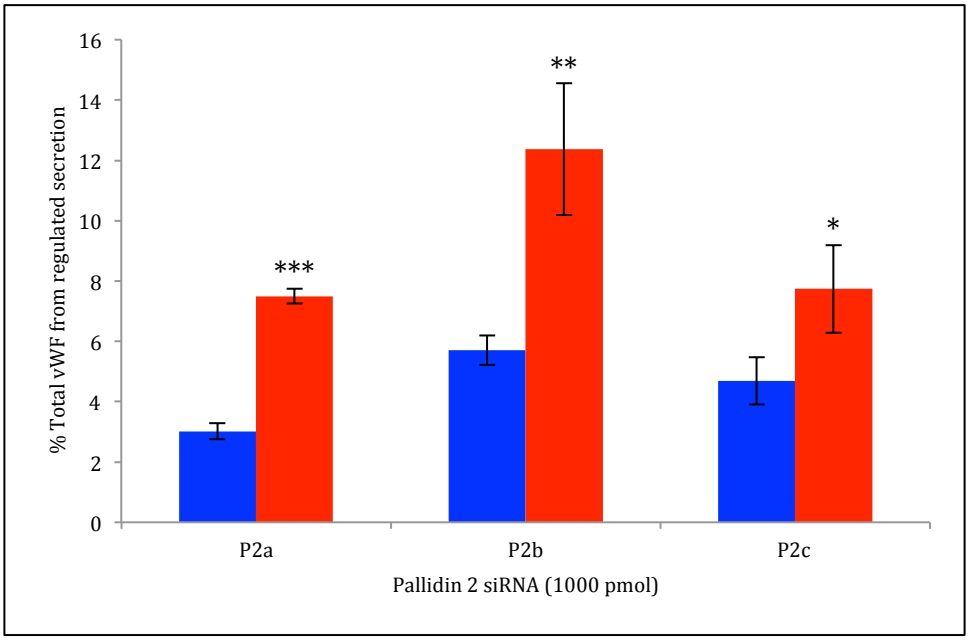

Three vWF secretion assays (three repeats within each experiment) to measure the percentage of vWF secreted in 30 minutes by regulated secretion from HUVECs when stimulated with 100 µM Histamine. *Luciferase* siRNA ablated HUVECs used as a control (Blue) and Pallidin 2 siRNA ablated HUVECs (Red) ablated with 1000 pmol of siRNA. Error bars are standard deviation. T-Test used to measure significance, *; p<0.05, **; p<0.01, ***;p<0.01.

Table 8 Pallidin 2 KD in HUVECs

		vWF secretion		
Experiment	**mRNA remaining**	**Control**	**Pallidin 2 KD**	**Fold change from control**
Pallidin 2a	15%	3%	7.5%	2.5
Pallidin 2b	11%	5.7%	12.4%	2.2
Pallidin 2c	15%	4.7%	7.7%	1.6

Table of results from Figure 17 - a vWF secretion assay measuring the percentage of vWF secreted in 30 minutes by regulated secretion from HUVECs when stimulated with 100 µM Histamine. Luciferase (Control) siRNA and *pallidin* siRNA KD efficiency measured by qPCR in parallel with the secretion assay – mean of three qPCR measurements taken from pooled lysates from 2 confluent wells of HUVECs from a 12 well plate.

To confirm this phenotype two additional siRNAs targeted towards *pallidin* were used (named here Pallidin 3 and Pallidin 4) and a secretion assay performed. An increase in vWF secretion was observed (1.6-2.2 fold change from the control) across all three siRNAs targeted towards *pallidin*, with the highest difference between the control and the KD being observed in the condition that achieved the highest KD of *pallidin* as determined by qPCR (Figure 18, Table 9).

Figure 22 Pallidin 2,3 and 4 KD in HUVECs – vWF secretion assays

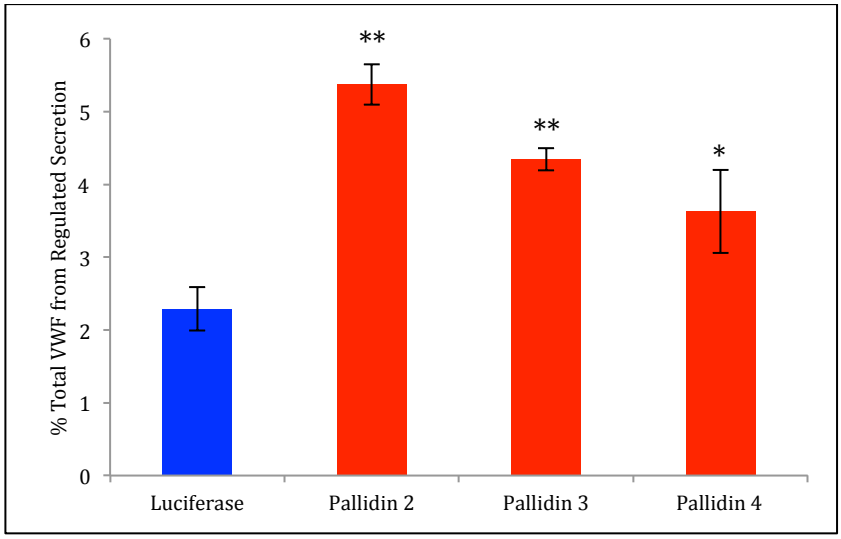

vWF secretion assay to measure the amount of vWF secreted in 30 minutes from HUVECs when stimulated with 100 µM Histamine. Regulated vWF secretion percentage displayed for HUVECs ablated with 1000 pmol of *luciferase* and Pallidin 2, 3 and 4 siRNAs. Error bars are standard deviation. T-Test used to measure significance, *; $p<0.05$, **; $p<0.01$.

Table 9 Pallidin 2, 3 and 4 KDs in HUVECs

		vWF secretion		
siRNA	**mRNA remaining**	**Control**	**BLOC-1 KD**	**Fold change from control**
Pallidin 2	27%	2.6%	5.5%	2.2
Pallidin 3	31%	2.6%	4.4%	1.7
Pallidin 4	44%	2.6%	4%	1.6

Table of results from Figure 18 - vWF secretion assay measuring the percentage of vWF secreted in 30 minutes by regulated secretion from HUVECs when stimulated with 100 µM Histamine. *Luciferase* (Control) siRNA and *pallidin* siRNA KD efficiency measured by qPCR in parallel with the secretion assay – mean of three qPCR measurements taken from pooled lysates from 2 confluent wells of HUVECs from a 12 well plate.

Since the siRNA ablation of *pallidin* appeared to increase the amount of vWF secreted, a second approach was sought confirm the phenotype. Control and *pallidin*-depleted cells were stimulated with secretagogue in the presence of a vWF antibody in order to visualise the amount of vWF present on the cell surface (*205*, *206*). The presence of the antibody in the stimulation medium inhibits the production of vWF strings (*206*) but leads to the retention of vWF at the exocytic site. The number of exocytic sites on the cell surface correlates well with vWF secretion as measured by secretion assays (*207*). The number of exocytic sites in control and *pallidin*-depleted cells was measured in a preliminary experiment (Figure 23). Indeed, the siRNA ablation of Pallidin 2 resulted in an increase in the

number of exocytic sites measured, further suggesting that the secretion of vWF is increased in these cells (see 4.5.4 for method).

Figure 23 Exocytic Site analysis in Pallidin 2 KD HUVECs

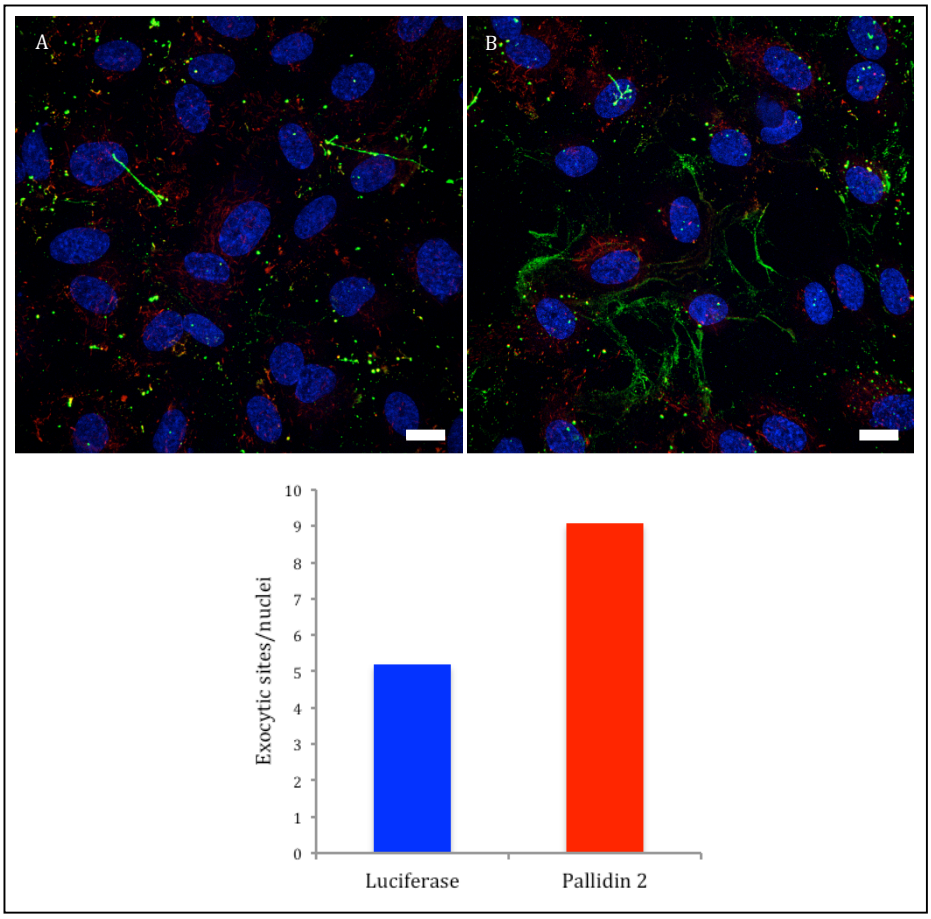

Two fluorescent confocal images of *luciferase* (A) and Pallidin 2 (B) siRNA ablated HUVECs with immunofluorescent labelling representing; internal vWF (red) external vWF (green) and nuclei (blue). A bar chart representing the number of exocytic sites per nucleus in *Luciferase* siRNA (5.19) and Pallidin 2 siRNA (9.06) treated cells, 10 images were taken for each condition (bottom right panel). Scale Bars 10 μm

After establishing that the secretion of vWF was increased when cells were treated with *pallidin* siRNAs, it was important to try and establish the mechanism and location at which pallidin is acting. As discussed, the storage granule of vWF in endothelial cells is WPBs. It has previously been demonstrated that WPB size effects vWF secretion from HUVECs (*63*). Therefore, WPB feret diameter was measured. For this, the siRNA with the best KD efficiency was selected (Pallidin 2). The control and *pallidin*-depleted cells were then stained for vWF, imaged, and a high throughput morphometric analysis performed (see 4.5.1). Over 10,000 WPBs were analysed for both *luciferase* and Pallidin 2 KD and a significant difference was observed (p value < 2.2 e-16). WPBs from cells

depleted of *pallidin* had significantly smaller WPBs, with an increase particularly in the 1 µm size (Figure 24).

Figure 24 Pallidin 2 KD in HUVECs – WPB morphometric analysis

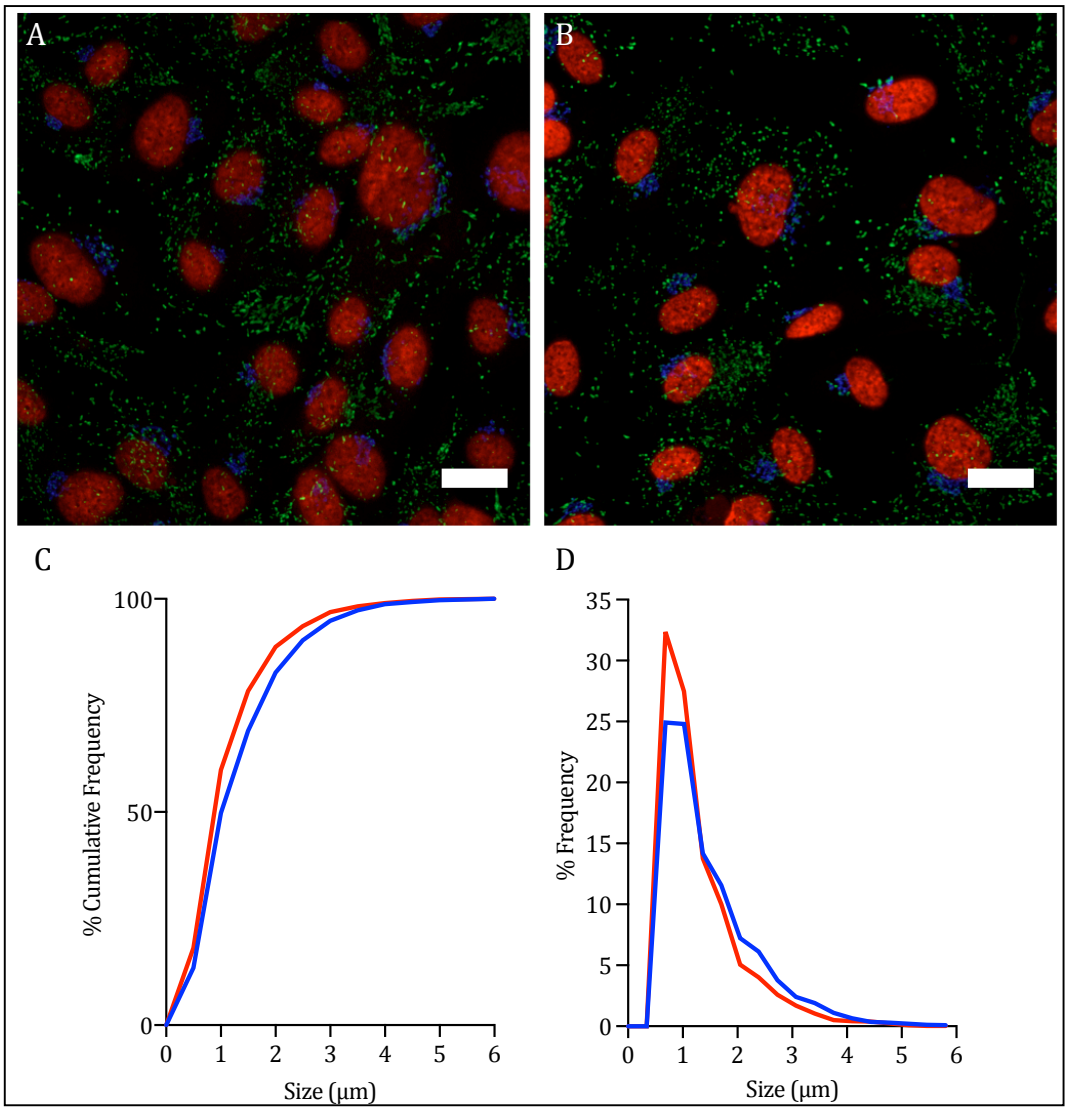

HUVECs were treated with siRNA against either *luciferase* (A) or *pallidin* (B) for 48 hours and fixed and stained for vWF (green), TGN46 (blue) and the nucleus (red). Images were acquired (Leica SP5 confocal microscope) using immunofluorescence protocol (4.3.1). Data from a representative experiment is shown (A,B). WPBs were segmented and feret diameter measured (C,D). The feret diameter of over 10,000 WPBs in *luciferase* control (red lines) and *pallidin* (blue Lines) siRNA treated cells was plotted with the cumulative frequency (C) and percentage frequency (D) displayed. Morphometry was measured using Image J (4.5.1) Significance was assessed using the Kruskal – Wallis Test p-value = 2.2e-16. Scale bars 10 µm

The next aim was to determine the multimeric state of vWF secreted from pallidin-depleted cells. Therefore, the vWF from the regulated secretion from HUVECs following a secretion assay were isolated from control and pallidin-

depleted cells and were run on a multimer gel to measure the multimeric composition of vWF (Figure 25). A reduction in the presence of high molecular weight multimers was observed in Pallidin siRNA treated cells. To analyse the distribution of bands, line profiles were drawn from bottom to top and plotted using ImageJ. Although this was preliminary data (n=1), it is suggestive of a reduction in high molecular weight bands as seen by the right hand side of the plot and the top of the gel.

Figure 25 Pallidin 2 KD in HUVECs – Multimer Gel

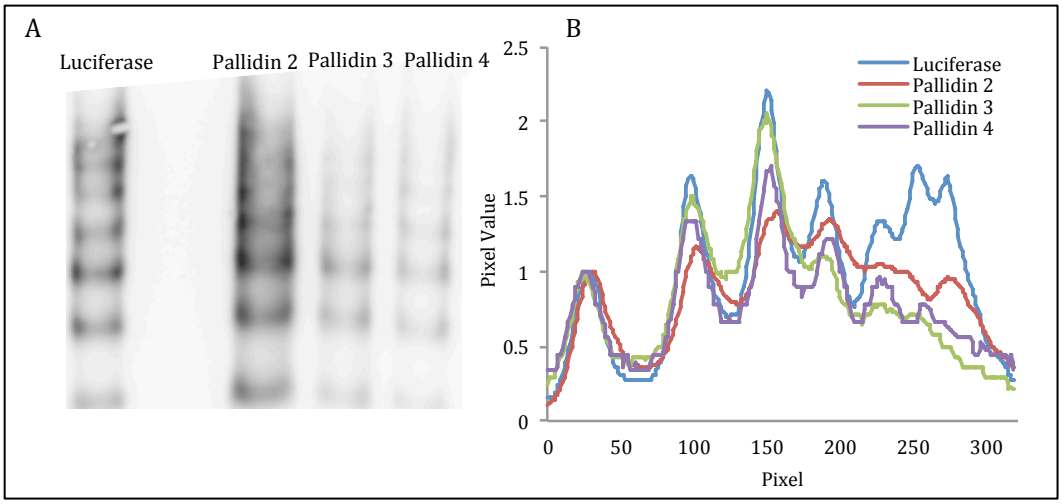

vWF multimer gel (A) and pixel value line plot performed in ImageJ (B) of *Luciferase*, Pallidin 2, Pallidin 3 and Pallidin 4. Plots normalised to the position and pixel value of the first band. A reduction in high molecular weight multimer band intensity as a proportion of the first band was observed.

Altogether, this data suggests that siRNA ablation of Pallidin leads to an increase in the secretion of vWF from HUVECs as measured by secretion assays. In three preliminary experiments there was a reduction in the size of WPBs, an increase in the number of vWF-positive exocytic sites and a decrease in higher molecular weight vWF multimers. These results are somewhat contradictory, as it has previously been shown that cells with smaller WPBs have a defect in vWF secretion (*199*), and the above results demonstrate the opposite. Therefore, additional siRNAs were used to assess the release of vWF measured by secretion assays in order to try and confirm this result. These (experiments number 5-7) however, gave contradictory results (Table 10) to the secretion assays performed before.

Table 10 Pallidin KD experiments summary

Experiment No.	siRNA sequence used	Pallidin KD	Fold change from control
1	Pallidin 2	15%	2.48
2	Pallidin 2	**11%**	**2.17**
3	Pallidin 2	15%	1.64
4	Pallidin 2	27%	2.12
	Pallidin 3	31%	1.69
	Pallidin 4	44%	1.54
5	Pallidin 2	16%	1.37
	Pallidin 3	**14%**	**0.82**
	Pallidin 4	30%	0.79
6	Pallidin 2	17%	1.82
	Pallidin 3	15%	1.01
	Pallidin 4	**28%**	**0.69**
7	Pallidin 2	32%	1.71
	Pallidin 3	41%	0.77
	Pallidin 4	68%	0.48

vWF secretion assay results using pallidin siRNAs treated cells with 100 µM histamine for 30 minutes. Luciferase siRNA was used as a control and Pallidin 2,3 and 4 to deplete pallidin. Fold change from control value coded green for an increase in vWF secretion and red for decrease over 15%, black for neither. The most efficient qPCR KD result for each pallidin siRNA sequence also highlighted in bold.

Experiment 5-7 did not demonstrate a consistent increase in the secretion of vWF that had been observed in experiments 1-4 (Table 10) and confirmed that off-target effects could not be ruled out. The three most efficient KDs by qPCR for the siRNA sequences Pallidin 2, Pallidin 3 and Pallidin 4 gave a 117% increase, 18% decrease and 31% decrease in vWF secretion respectively compared to the control. Only experiments 1-4 were in agreement that *pallidin* siRNA ablation resulted in an increase in vWF regulated secretion. To establish whether there was a significant relationship between KD efficiency and aberrant secretion, the amount of vWF secreted normalised to controls was plotted (Figure 26) against the percentage of *pallidin* mRNA remaining and the correlation was measured with pearson's coefficient.

Figure 26 Correlation between *pallidin* KD efficiency and vWF secretion in HUVECs

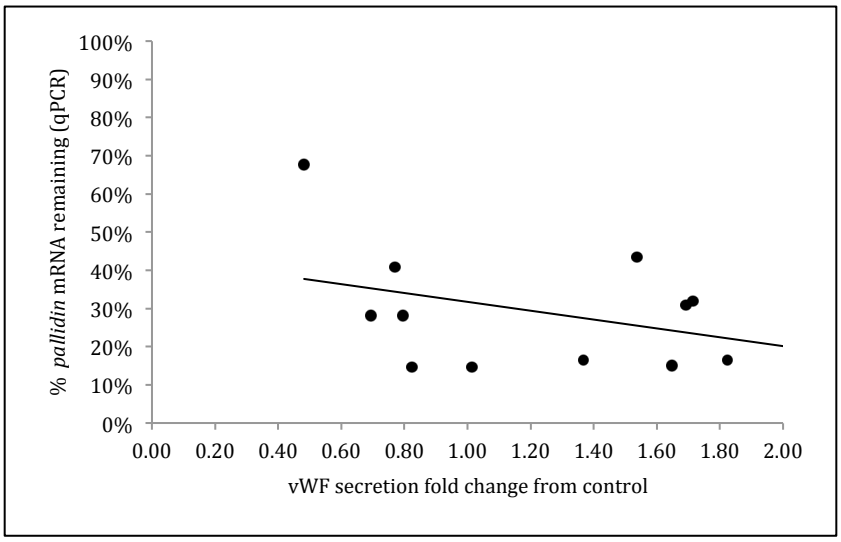

The percentage of pallidin mRNA remaining compared to control in each siRNA ablation experiment was measured and plotted against the fold change in vWF regulated secretion (includes histamine and PMA results) compared to control. Each experiment represented by a black dot, trendline shown in black. Pearson's coefficient R value = -0.4943. The result is not significant at $p > 0.05$.

There was only a weak correlation between the effect of the siRNA on secretion as expressed as a fold change from control HUVECs and the KD efficiency by qPCR ($p>0.05$). As the levels of pallidin protein in the cells and the efficiency of siRNA KD on reducing this could not be fully evaluated, due to a lack of reliable antibodies, it was decided to not continue with the exit site, multimer gel and WPB morphology analysis. If the *pallidin* siRNAs that were chosen had the potential to exhibit opposite significant secretory phenotypes then the likelihood that off-target effects would influence future findings would be probable. During the time that the BLOC-1 siRNA treatment experiments were performed, another project with the aim of investigating the effect of another HPS related complex, BLOC-3, on vWF secretion was also undertaken.

5.3 Results - A potential role for BLOC-3 in WPB function

BLOC-3 was selected as a potential complex to investigate in tandem with BLOC-1 as there is little known about its role in LRO biogenesis. Since there are only two proteins that form the complex (HPS1 and HPS4), it was hypothesised that

the effects of siRNA ablation on HPS1 would give a suitable indicator of whether this complex is important for WPB formation and function.

As with BLOC-1, there are commercially available antibodies available for HPS1 and HPS4, however, a western blot revealed that they were not specific enough (Figure 27) to quantify KD efficiency, therefore, an indication of the efficiency of the KDs was instead provided by a qPCR Reaction to measure the extent of reduction in the mRNA encoding the target protein.

Figure 27 Western Blot to measure HPS1 and HPS4 antibody specificity

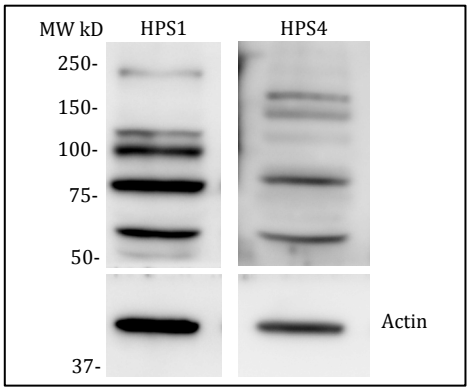

Antibodies against HPS1 (79KD) and HPS4 (90KD) were tested for specificity. A Precision Plus protein dual colour standard (Biorad) was also loaded as a molecular weight (MW) marker.

Two siRNA sequences targeting *HPS1* were tested for their efficiency in depleting HPS1 in HUVECs (Table 10).

Table 11 HPS1.1 and HPS1.2 KD qPCR

siRNA conc.	HPS1.1 mRNA remaining	HPS1.2 mRNA remaining
200 pmol	60%	51%
400 pmol	38%	58%
600 pmol	52%	28%
800 pmol	49%	25%

A series of *HPS1* siRNA concentrations 200-800 pmol were used to treat HUVECs to measure the depletion of HPS1 mRNA as determined by a qPCR. (For siRNA sequence see Table 2)

Neither of the siRNAs, named HPS1.1 or HPS1.2, achieved a KD efficiency (as quantified by qPCR) over 70%, apart from HPS1.2 at 600 and 800 pmol. Therefore, the siRNA named termed HPS1.2, was used at 1000 pmol to deplete

HPS1 from HUVECs and secretion assays performed with the cells treated with the secretagogue histamine for 30 minutes.

Figure 28 HPS1.2 KD in HUVECs – vWF secretion assays

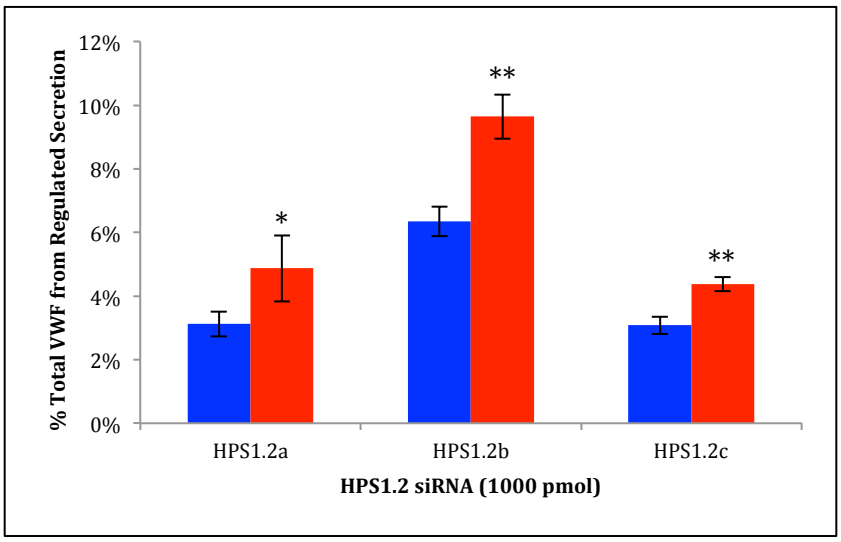

Three vWF secretion assay repeats to measure the amount of vWF secreted in 30 minutes from HUVECs when stimulated with 100 µM Histamine. Regulated vWF secretion percentage displayed for HUVECs ablated with 1000 pmol of *luciferase* (blue) and three repeats; HPS1.2a, HPS1.2b and HPS1.2c (red) siRNAs. Error bars are standard deviation. T-Test used to measure significance, *; $p<0.05$, **; $p<0.01$.

Table 12 HPS1.2 KD in HUVECs – vWF secretion assays

		vWF secretion		
Experiment	mRNA remaining	Control	HPS1.2 KD	Fold change from control
HPS1.2a	18%	3%	5%	1.38
HPS1.2b	17%	6%	10%	1.52
HPS1.2c	28%	3%	4%	1.42

Three vWF secretion assay repeats measuring the percentage of vWF secreted in 30 minutes by regulated secretion from HUVECs when stimulated with 100 µM Histamine. *Luciferase* (Ct) siRNA and *HPS1* siRNA KD efficiency measured by qPCR in parallel with the secretion assay – mean of three qPCR measurements taken from pooled lysates from 2 confluent wells of HUVECs from a 12 well plate.

There was no improvement in KD efficiency by increasing the secretagogue concentration to 1000 pmol. However, encouragingly the secretion of vWF in response to histamine in *HPS1* KD cells was significantly increased compared to control cells.

To confirm the secretory aberration observed, three other *HPS1* siRNAs were ordered from published sequences (*123*) where they had been successfully used on HELA and MNT-1 cells to demonstrate the mislocalisation of RAB32 and

RAB38 causing defects in melanosome maturation in MNT-1 cells. Two of these sequences, termed 'HPS1.3' and 'HPS1.5' achieved a KD over 75% at 800 pmol. Secretion assays were then performed with cells treated with 800 pmol of HPS1.2, HPS1.3 and HPS1.5 siRNAs (Figure 29).

Figure 29 HPS1.2, 1.3 and 1.5 KD in HUVECs – vWF secretion assays

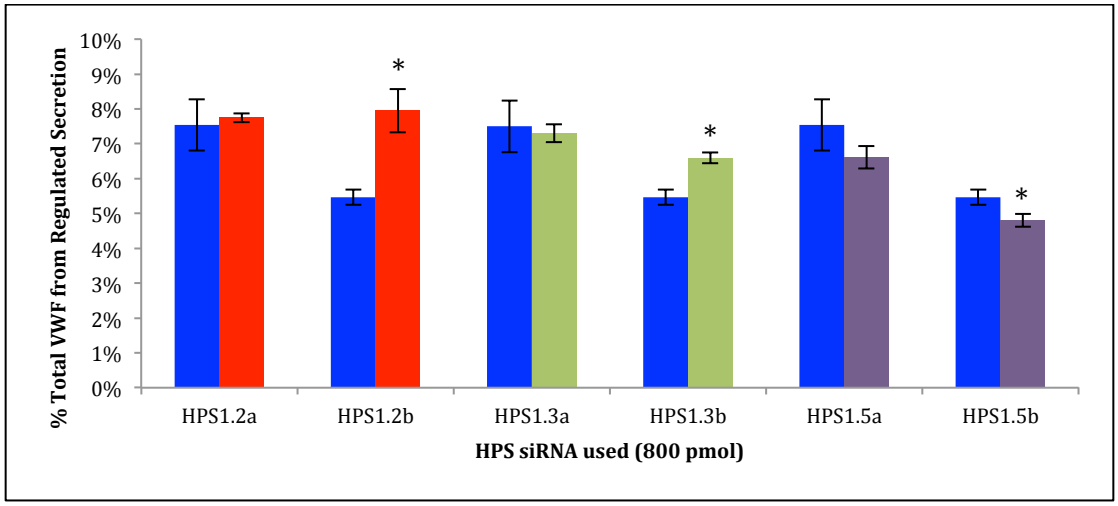

vWF secretion assays to measure the amount of vWF secreted in 30 minutes from HUVECs when stimulated with 100 µM Histamine. Regulated vWF secretion percentage displayed for HUVECs ablated with 800 pmol of *luciferase* (blue) and HPS1.2 (red), HPS1.3 (green) and HPS1.5 (purple), two repeats for each siRNA are shown (a and b). Error bars are standard deviation. T-Test used to measure significance, *; $p<0.05$.

Table 13 HPS1.2, 1.3 and 1.5 KD in HUVECs – vWF secretion assays

siRNA and experiment (a or b)	mRNA remaining	Ct Secretion	HPS1 siRNA Secretion	HPS1/Ct Secretion
HPS1.2a	7%	8%	8%	1.03
HPS1.2b	11%	5%	8%	1.45
HPS1.3a	21%	8%	7%	0.97
HPS1.3b	22%	5%	7%	1.21
HPS1.5a	23%	8%	7%	0.88
HPS1.5b	21%	6%	5%	0.87

Table of results from Figure 29 vWF secretion assays measuring the percentage of vWF secreted in 30 minutes by regulated secretion from HUVECs when stimulated with 100 µM Histamine. *Luciferase* (Ct) siRNA and *HPS1* siRNA KD efficiency measured by qPCR in parallel with the secretion assay – two experiments for each siRNA are shown (a and b) the mean of three qPCR measurements taken from pooled lysates from 2 confluent wells of HUVECs from a 12 well plate.

The two other *HPS1* siRNA sequences (HPS1.3 and HP1.5) did not replicate the secretion increase observed in HPS1.2 treated cells. Whilst a significant increase in vWF secretion was observed in cells treated with the *HPS1* siRNA termed HPS1.3, the converse result was seen in cells treated with the other comparative siRNA sequence HPS1.5, even though both sequences resulted in a KD efficiency of over 75%. Also, the highest qPCR KD, achieved by the HPS1.2 siRNA in

experiment HPS1.2a, with a 93% KD efficiency, displayed no significant aberrant secretion. Preliminary results with siRNAs targeted towards HPS4, the other BLOC-3 subunit, proved unsuccessful as a sufficient KD was not achieved (data not shown).

Conflicting secretion assay results with a similar KD efficiency, as measured by qPCR, lead to the conclusion that this work should not be continued, as the regulated secretion of vWF is a result of WPB formation and function, it was likely that the variation seen in secretory phenotypes would also be observed when studying other variables.

5.4 Discussion

In this chapter, siRNA ablation experiments were performed with the aim of determining the importance of HPS related proteins/complexes on WPB biogenesis and function in a primary human endothelial cell line. Proteins related to two HPS complexes, BLOC-1 and BLOC-3, were KD and the resultant regulated vWF secretion was measured. In the BLOC-1 KD experiments, the morphology of WPBs, the number of exocytic sites per cell and the multimeric composition of secreted vWF was also measured in a series of preliminary experiments.

HPS has been shown to affect LRO function in a number of studies. Apart from hypopigmentation, the one phenotype that unites all the 12 HPS mouse models is a bleeding disorder (Figure 7). WPBs have been shown to be critical to haemostasis due to the fact their primary role is to carry the protein vWF (see 2.4.3). Despite this, the effect of depleting HPS related proteins in human cells and the resulting effect of vWF secretion has not been investigated. It was expected that if a bleeding disorder was a common phenotype in HPS patients, then abnormal vWF secretion by WPBs might be a contributor to this.

WPBs are formed at the TGN (*63*) and one of the HPS complexes whose function is thought to act in this area is BLOC-1 (*113*), making it a good candidate for a HPS-related complex that may affect WPB biogenesis. The work in this thesis initially focused on the BLOC-1 proteins, specifically Muted, Pallidin and Snapin (see 5.1) due in part to the observation by a previous post-doc in the lab that knocking these three proteins down in HEK cells expressing exogenous vWF caused a three-fold reduction in vWF secretion (Figure 17). Although initial results did replicate a reduction in vWF secretion (around 30%), I was unable to replicate these results due in part to a poor KD efficiency and switched to a focus on ablation of *pallidin* (see 5.1), as the pallidin protein has been shown to be required to stabilize the BLOC-1 complex (*190*). The initial *pallidin* KD results were surprising, as I saw a dramatic increase in the secretion of vWF that

appeared to be proportional to the level of KD observed from the qPCR measurements. Preliminary data also suggested that the feret diameter of WPBs was also significantly reduced (p-value 2.2e-16) and an increase in the number of exocytic sites (5.19 in control and 9.06 sites in *pallidin* KD cells per nucleus). These were unusual observations as a reduction in WPB feret diameter after treatment with an *AP-1* siRNA or treating with nocodazole which disassembles the Golgi ribbon by depolymerising microtubules, results in a decrease in vWF secretion (*63*, *69*) and a reduction in the size of WPBs. Initial experiments appeared to suggest a reduction of high molecular weight vWF being secreted (Figure 25) and also an increase in the number of exocytic sites at the cell surface (Figure 23) when stimulated with a secretagogue as compared to controls. An increase in the vWF exocytic sites could be a possible explanation for the increase in secretion observed in the secretion assays and a lack of high molecular weight multimers suggests that WPBs were being released prematurely, however, this was not confirmed. It is also counter-intuitive that if BLOC-1 is a complex that is important for the biogenesis and formation of other LROs, that depleting endothelial cells of this complex would increase the levels of secretion of vWF from WPBs unless BLOC-1 was performing a regulatory function. A similarity can be seen with Rab27a ablation, where an increase in secretion, a reduction in higher molecular weight multimers and decrease in vWF string length is observed (*81*). As Rab27a is only found on mature WPBs, it could be possible that this is an indicator that the WPBs in the Pallidin 2 KD were undergoing typical maturation, but it does not explain the increase in vWF exocytic sites.

Critically, the initial increase in vWF secretion observed with an siRNA targeted to *pallidin* was not reproducible with other siRNAs targeted to the same sequence, despite a similar reduction mRNA being observed by qPCR. The HUVECs stocks used in experiments 5-7 were from the same batch of cells as experiments 1-4, however, the effect of the siRNAs was contrasting; it is unclear why this happened and could potentially be due to reproducibility issues within the experimental design, variability within HUVEC stocks and/or sensitivity within secretion assays, yet this seems unlikely. Due to these inconsistencies

between siRNAs it is more likely that the initial results seen with Pallidin 2 were due to off-target effects. As a poor KD efficiency was observed with lower concentrations of siRNA, the increase in siRNA used may have improved the KD of *pallidin* but this also increases the likelihood of off-target effects (*208*). The results that are demonstrated with these sequences in published literature do not report off-target effects and this could be due to the fact these siRNA sequences were employed in different cell lines and focused on the mislocalisation of proteins observed by fluorescent microscopy and thus the off-target effects affecting secretion were not observed (*111*). To investigate this further, a BLAST (*209*) search was performed on the siRNA sequence used for *pallidin* and this showed that there were no matches with a high similarity (over 70%). It is still possible that the effect on vWF secretion, size of WPBs, reduction in low molecular weight multimers in secreted vWF and the increase in the number of exocytic sites could be due to a *pallidin* KD, however, due to a lack or reliable antibodies, time constraints and contradictory results, this was not pursued and attention turned to promising early results using a *HPS1* siRNA to investigate the function of the BLOC-3 complex.

Despite early results suggesting that a *HPS1* KD was causing a significant increase in vWF secretion, when the secretion assays were repeated with additional siRNAs to KD HPS1, the secretion increase was not replicated, despite the sequences being taken from a publication where these siRNAs were successfully used to KD HPS1 in HELA and MNT-1 cells to demonstrate the mislocalisation or RAB32 and RAB38 and defects in melanosome maturation in MNT-1 cells (*123*). Like with the *pallidin* ablation studies, it is possible that the off-target effects were cell and assay specific.

Preliminary experiments used to KD *HPS4*, the other member of the BLOC-3 complex did not achieve a KD of over 50% as measured by qPCR (data not shown). Due to the contradictory results observed and an inability to test protein levels of HPS1 and HPS4 by a western blot, a conclusion about the role of BLOC-3 in WPB secretion was not possible.

Despite promising results with siRNAs against BLOC-1 and BLOC-3, it was not possible to achieve the original aim of conclusively answering the question of whether there is a role for the HPS proteins in the biogenesis and function of WPBs and thus this question was not taken further. It was surprising that an increase in secretion was observed, given that BLOC-1 and BLOC-3 related diseases have a bleeding disorder, however, it could not be discounted that the bleeding disorder seen in these patients may be as a result of defective platelet granule formation and the effect on WPBs could be secondary to this. In future, different approaches to achieve a stable KD of HPS proteins in human endothelial cells must be sought. These may include techniques such as producing blood outgrowth endothelial cells from HPS patients (*210*), or Crispr/cas9 gene ablations (*210*). Only when a reliable and quantifiable KD of HPS proteins is achieved can greater conclusions about the role of these proteins in WPB formation and function be drawn. During this research, a paper from Flaumenhaft and co-workers (*211*) using siRNA to KD *HPS6* in HUVECs (BLOC-2 complex) demonstrated impaired PDI secretion and exocytosis of WPBs; currently it is not clear why this study succeeded and the secretion assays highlighted in this chapter did not.

It is clear that to be able to assess the role of LROs in LRO-related disorders, new techniques must be developed to study and analyse them. To further this pursuit, efforts were turned to improve the diagnosis of disorders relating to another set of LROs, the platelet granules.

6 Chapter 2 A Super Resolution method to study Platelet Granules and their related disorders

6.1 Introduction

Platelets contain alpha granules, dense granules, multivesicular bodies, and lysosomes (*25*). In recent years, new methods have challenged the classical view that alpha and dense granules represent homogeneous populations (*9*, *25*, *212*, *213*) and consequently, the basis on which diagnosis and definition of their related disorders rests has come into question. In this chapter new techniques are investigated for analysing platelet granules, not only to revisit some of the uncertainty in their analysis, but also to potentially apply these new techniques to the diagnosis of genetic disorders. In this chapter steps taken to develop a new technique for analysing two LROs are reported; platelet alpha and dense granules, using two SRM techniques; dSTORM and SIM.

6.1.1 Alpha granules

Alpha granules are the major storage and secretory organelle in the platelet, they are also the most abundant granules numbering around 50-80 per platelet (*39*). Formed from multivesicular precursor organelles, they acquire cargo from both the endocytic and biosynthetic routes. Alpha granules contain over 300 distinct molecules (*40*) that comprise the bulk of the platelet secretome including haemostatic factors (e.g., Factor V, vWF, fibrinogen), angiogenic factors (e.g., angiogenin, VEGF), anti-angiogenic factors (e.g., angiostatin, PF4), growth factors (e.g., PDGF, bFGF, SDF1α), proteases (e.g., MMP2, MMP9), necrotic factors (e.g., TNFα, TNFβ) and other cytokines (*40*). Alpha granules, given their content, have the properties of both secretory organelles and late endosomes, which justify their characterisation as an LRO. Historically, morphological features observed

by EM have led to recognition of alpha granules as a distinct organelle. These identifiable features include; 1) the peripheral membrane of the granule, 2) an electron dense nucleoid that contains chemokines and proteoglycan, 3) a less electron-dense area adjacent to the nucleoid that contains fibrinogen, and 4) a peripheral electron-lucent zone that contains vWF ((*28*) see Figure 31 for an example TEM image). Absence of a particular alpha granule marker does not preclude classification of a vesicular structure as an alpha granule, as even the major storage proteins of alpha granules, vWF and Fibrinogen, have limited colocalisation by immunofluorescent confocal microscopy (*214*). Indeed, a colocalisation analysis by Kamykowski et al. found considerable variation in co-distributions and little cargo clustering with 15 separate alpha granule markers (*212*). Thus, the definition of alpha granules may yet undergo further refinement as we learn more about their formation, structure, and content. The conflicting functions (e.g., proangiogenic and antiangiogenic) of the proteins stored in alpha granules gives rise to the theory that there could be functionally distinct populations of these granules which are released differentially in response to their relevant stimuli.

Alpha granule biogenesis is affected in three inherited human disorders: Quebec Platelet Disorder, GPS and ARC (arthrogryposis, renal dysfunction and cholestasis) syndrome. In GPS the amount of protein synthesised in MKs is significantly reduced, although endocytosed alpha granule content is less affected (*42*). It has recently been demonstrated that mutations in the Neurobeachin-like 2 (*NBEAL2*) gene cause GPS (*42*) and these mutations appear to be involved in the packing of endogenously synthesised secretory proteins into developing alpha granules (see also 2.5.1 for GPS).

6.1.2 Dense granules

Dense granules are around 150 nm in size and also originate from endosomal precursors. There are typically 3-8 (*215*) of these organelles per platelet. Dense granules are acidic and therefore accumulate acidic dyes such as mepacrine (*216*) and acridine orange (*44*). In terms of content they are much more simple than alpha granules and contain serotonin, histamine, ADP, ATP, GDP, GTP, magnesium pyrophosphate (*47*) and polyphosphate (*46*). Dense Granules also carry the lysosomal membrane proteins CD63 and LAMP1/2 but also non-lysosomal proteins such as P-Selectin (*50*), GPIb (*217*) and αII-β3 integrin (*218*). Some structural information about dense granules can be obtained using the whole mount EM technique (*36*, *219*) and this is currently the gold standard for assessing the number of dense granules per platelet. Here, a patient's blood is spun in a centrifuge to form PRP and a drop of PRP is placed on a formvar-coated grid and visualised, without fixation, using EM (Figure 30).

6.1.3 Currently available PSD diagnostic tools

The established tools available to clinicians for diagnosing PSDs are currently limited, and discussion within the clinical community suggests that there is room for additional new techniques, for example as in recent reports (*220*, *221*) suggesting the further use of FACS-based assays as a diagnostic tool in this context. Currently, assays for diagnosing a potential dense granule disorder include aggregation in response to a panel of agonists, measurement of platelet nucleotides and/or ATP release and direct counting of dense granules using EM.

Platelet aggregation is measured by Light transmission aggregometry (LTA) and was developed in 1962 by Born (*222*) and O'Brien (*223*). It is still considered the gold standard for testing platelet function. The change in optical density of a rapidly stirred sample of platelet-rich plasma (PRP) at 37 °C is measured by a photometer and compared with normal values after the addition of platelet agonists such as arachidonic acid, thrombin, ADP, epinephrine, collagen and ristocetin (*37*). Despite its widespread use, there are a number of caveats

regarding LTA results. Primarily, it is not strictly comparable to physiological platelet aggregation as the separated platelets in PRP only form aggregates following the addition of soluble agonists under low shear conditions (stirring). LTA results are also difficult to interpret and different haematology centres (and often doctors) will only trust results taken from their own lab (conversation with Dr. Keith Gomez, Haematology consultant at the Royal Free Hospital, London). In 2013 a consensus of the working party from the platelet physiology subcommittee of SSC/ISTH concluded that; 'LTA is a time-consuming and technically challenging technique that is affected by many pre-analytical and analytical variables, and these must be carefully controlled for by expert personnel. For this reason, LTA should be performed only in specialised laboratories' (*224*). The test itself is inherently variable as LTA can be affected by a number of factors including the patient's medication. In an ideal situation the samples for platelet function studies should only be collected from fasting subjects who have refrained from smoking and caffeine for 24 hours before testing. If the patient is taking medication known to affect platelet function, e.g. antibiotics, anti-depressants, beta-blockers, non-steroidal anti-inflammatory drugs (*225*), then the test should be deferred for at least 10 days after the last dose. Herbal remedies, garlic, alcohol and certain foods may also cause acquired platelet dysfunction (*225*). In normal clinical practice it is often impossible to avoid all of these patient-related variables and so a practical approach is to proceed with the platelet function tests, but if they are abnormal, to then collect a new sample under stricter conditions (*224*).

Perhaps the major drawback of aggregometry and nucleotide measurement is that these tests tell us little about platelet structure. In genetic disorders such as HPS/GPS, characterised by a reduction in platelet granules, the ability to count the number of dense/alpha granules per platelet efficiently would immensely improve diagnosis. Using whole mount EM to resolve platelet granules is currently the gold standard for identifying a lack of dense granules but is rarely used due to a number of caveats. Quantitative EM analysis requires an electron microscope, specialised skills, is time-consuming, and is very difficult to automate. Without markers, granules are difficult to define and identification can

differ depending on the analyst (*12, 4.2.2*). An absence or reduction of dense granules, due to mutations in the cellular machinery used in granule formation, is found in patients with genetic disorders such as HPS and CHS (*36*) and is in keeping with a global effect on the biogenesis other LROs in these disorders (see 2.5.2). However, the contrast within the image is often variable and can lead to difficulties in classification. Other EM methods such as serial sectioning TEM or EM tomography are currently too impractical to perform in a clinical context or on a large dataset (*25*).

Figure 30 Dense Granule counting in a test sample

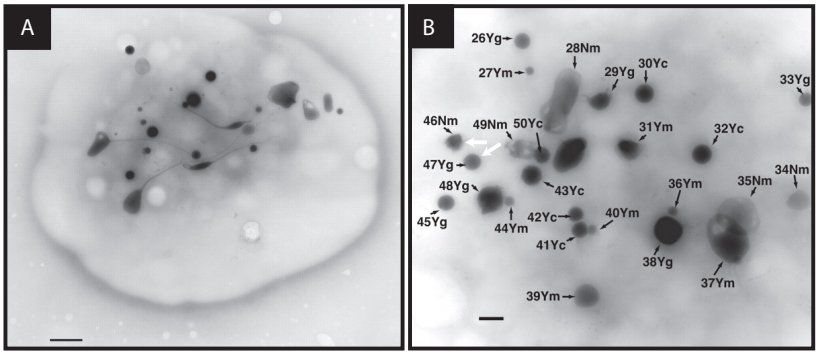

Images from Hayward et al. (*162*) A) Whole mount EM image of a normal platelet that was given to participants to estimate the numbers of dense granules contained in this platelet, estimates ranged from 6-24 dense granules. Bar indicates 500 nm. B) Whole mount EM image of a normal platelet with sequentially numbered, labelled structures that were provided to participants to indicate which structures they would count as dense granules. Structures counted (Y) or not counted (N) and the level of consensus (c, complete; g, good or 86%; m, moderate or 57%–71%) are indicated. White arrows highlight an example of two similar structures; 46 is moderately declared not a dense granule, whereas 47 is confidently determined a dense granule and highlights the difficulty in defining dense granules by this method. Scale bar in A 500 nm, Scale bar in B 200 nm.

An example of the variability seen in whole mount EM dense granule counting is discussed by Hayward et al. (*162*) where a number of sites across the North American Specialised Coagulation Laboratory Association were asked to evaluate the number of dense granules in one image of one platelet (Figure 30). The number of dense granules reported ranged from 15 to 24 for experienced sites and one 'inexperienced site' counted only 6 (*162*). It must be stressed that this variability was observed from counting a single image. It was discovered during the work in this thesis that different grids and even different areas of the same grid can potentially provide images with differing contrast (data not shown). Adding to this is the heterogeneity in the number of dense granules per platelet in the population, the variability when using different TEMs to image platelets

and the inevitable variation in the sample preparation at different sites, this means that a standardised methodology is almost impossible without centralised facilities. Therefore, new techniques are highly desirable for counting dense granules if conclusions about genetic disorders such as HPS are to be effectively drawn in a clinical context. To further complicate the diagnosis of these disorders the equipment and specialised techniques required for these analyses are not available in most hospitals, requiring patients with platelet disorders to travel long distances to a specialised centre, leading to these centres being oversubscribed and ultimately results in patients receiving limited care. The first aim is to speed up and provide a more efficient and accurate diagnosis, which will also in turn improve our understanding of PSDs and LROs.

As discussed above, alpha and dense granules have historically been defined by their appearance in EM, however, there is no current method for easily analysing both granules in one sample that does not require EM methodology which would not be appropriate in a clinical context. Given the difficulty in identifying these granules in their corresponding standard EM approaches, new techniques for defining and analysing these populations of both granules are needed. Platelets are 2 to 5 μm in diameter; their dense granules are around 150 nm and their alpha granules 200-400 nm (*226*). While confocal microscopy typically offers a lateral spatial resolution of 250 to 300 nm, the new SRM methods (*154*, *227*, *228*), use a variety of different strategies to overcome the diffraction limit and can resolve structures in the 10-200 nm range. It was hypothesised that their ability to resolve small objects would allow them to identify individual platelet granules and that this could prove a useful technique with which to study platelet granule morphology with a further aim of applying these methods to diagnose PSDs, such as GPS and HPS. Markers for alpha (vWF, P-Selectin) and dense (serotonin, CD63) granules could be analysed without the need for laborious EM techniques that relied upon subjective criteria for categorising granules. It was hypothesised that it would be advantageous therefore, to focus on the shared content between populations of granules as oppose to focusing on the identification of the granules themselves. Indeed, a reduction in the number of CD63 positive granules in HPS patients has been suggested (*35*) and similarly

vWF in GPS (*91*). However, these observations have relied upon subjective counting techniques and imaging methodology that cannot fully resolve a single granule. There are therefore, three main requirements for a new diagnostic technique; 1) A simple, robust protocol where samples can be taken easily at a local hospital and transported to a central facility for analysis and re-analysis if required 2) An imaging technique that has sufficient resolution to effectively image small objects such as platelet granules. 3) A method that is integrated with an unbiased analysis that can give clinicians clear quantitative data to diagnose a disorder.

To achieve these aims an SRM imaging approach was undertaken that would be analysed using an automated morphometric analytical workflow redesigned from similar methods applied by the Cutler lab to analyse WPBs (*63*, *163*). The aim was to introduce a non-biased, reliable method of assessing the numbers of organelles found in a sample of platelets, without the need to perform any laborious and/or subjective techniques.

6.2 Results

To validate our findings using new SRM immunofluorescence techniques it was important first, despite their limitations, to establish comparator protocols to analyse the platelet granules by the classical EM techniques. To visualise alpha granules, platelets were fixed, dehydrated and embedded in epon before sectioning (see 4.4.1) whereas to be able visualise/count dense granules the gold standard whole mount EM approach (see 4.4.2) was employed. It was important to set strict criteria for counting dense granules as seen in EM. This was particularly important given the variability in analysis observed in the literature (*162*).

6.2.1 Imaging platelet alpha granules by TEM

Figure 31 Thin Section TEM image of a Control Platelet

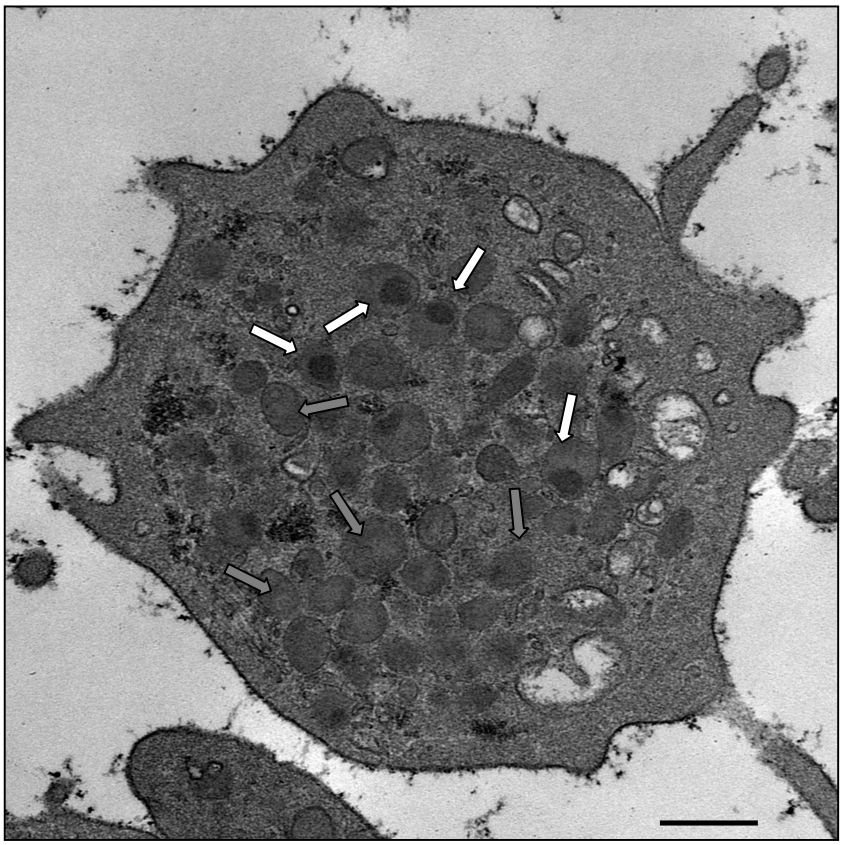

Thin section of platelet observed by TEM after fixation, dehydration and embedding in epon (see 4.4.1) White arrows mark the platelet alpha granules, other alpha granule-like structures are marked by grey arrows, although it is difficult to be completely sure of the classification. In this thin section no dense granules could be identified. Scale bar 500 nm

First platelets were prepared for TEM (Figure 31). Thin sections of Platelets (TEM) have contributed much to the present understanding of both platelet ultrastructure and have also been used to characterise disorders such as GPS, where patients' platelets display a reduction in alpha granules (*88*, *229*). Although the identification of alpha granules by thin section TEM images relies on the subjective identification of what is an alpha granule in a given image (Figure 31), we established a method for imaging alpha granules in a platelet sample to use as a comparator for new methods using immunofluorescent staining of alpha granules imaged by SRM.

6.2.2 Imaging platelet dense granules by Whole mount EM

Figure 32 Whole mount EM of platelets

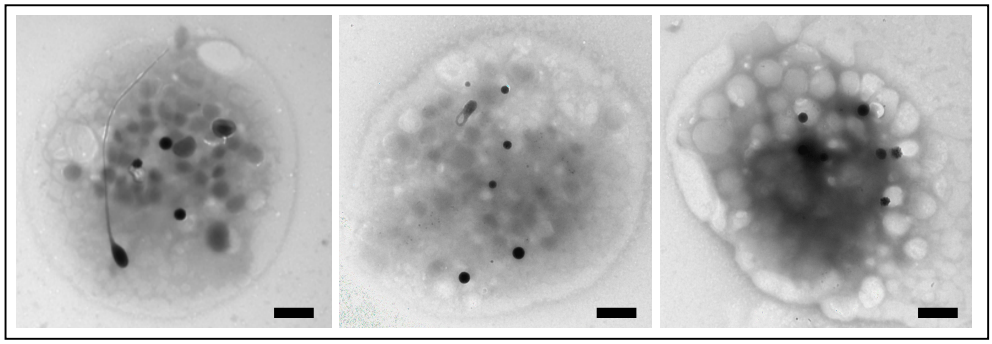

Three typical examples of control platelets imaged by Whole mount EM. Scale bars 500 nm. An inherent variation in granules morphology, contrast and size can be seen. Platelet granules are often difficult to define over similar structures in the platelet (left panel), can be small (middle panel) and in some cases are difficult to resolve due to high internal contrast in the platelet (right panel)

Whole mount EM imaging of platelet granules is still considered mainly a research tool and has not been thoroughly validated and standardised as a clinical test. However, despite this, it is still considered the gold standard for counting the number of dense granules in platelets (*230*). In initial attempts to perform this technique we found that very few platelets were attaching to the grid and this made the acquisition of quantitative data time-consuming and impractical. A large improvement in this was seen when centrifuging platelets, without fixation, onto formvar coated copper grids (see 4.4.2); three examples of platelets prepared in this way are shown (Figure 32). As discussed (see 4.4.2 for whole mount EM dense granule counting criteria), consistency in the counting of dense granules has a number of challenges. Despite this, we established a strict protocol for counting granules that improved reliability and proved a valuable comparator for new methods using immunofluorescent staining of dense granules imaged by SRM.

6.2.3 Imaging platelet alpha granules by dSTORM

For the purpose of applying SRM to image platelet granules we began with the methodology delivering the best resolution; localisation microscopy. A type of localisation microscopy (dSTORM) was the first technique used (see 2.7.2.1). Platelets were prepared and stained for vWF (a marker of alpha granules),

images were then acquired using both a widefield microscopy technique and dSTORM for comparison (Figure 33).

Figure 33 dSTORM image of platelet immunolabelled with vWF

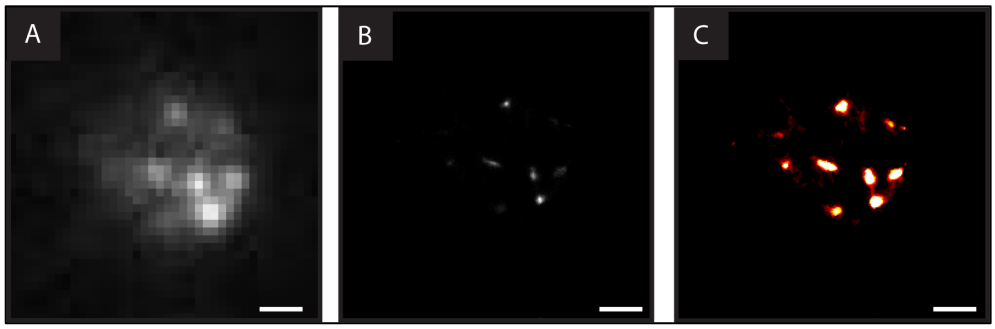

Widefield (A), dSTORM reconstructed image (B), dSTORM reconstructed – contrast enhanced and lookup table changed to red hot (C). The improvement in resolution and the signal to noise is immediately apparent. A typical resolution of 20-25 nm was achieved according to Rees et al. methodology to estimate SRM resolution (*159*) Scale Bar 1 µm.

The improvement in resolution and the signal to noise is immediately apparent when platelets are labelled with vWF and imaged by dSTORM imaging techniques (Figure 33) compared to widefield images.

Figure 34 dSTORM imaging of vWF in platelets

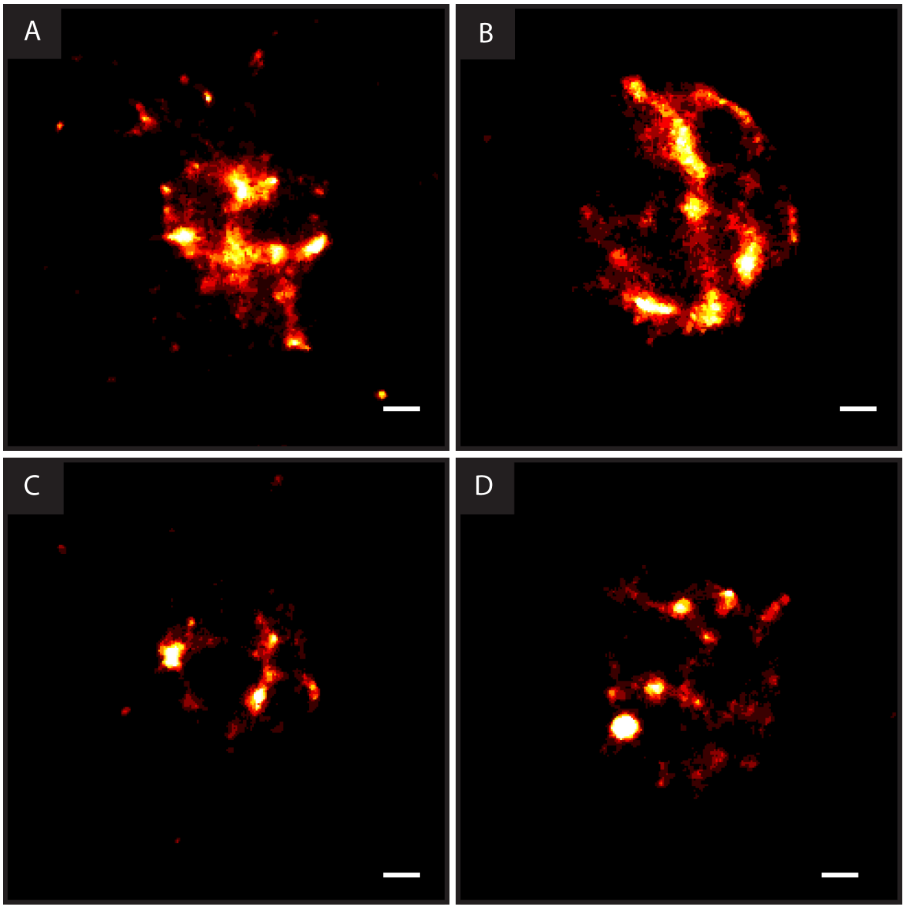

Representative dSTORM images of vWF in control platlelets. A typical resolution of 20-25 nm was achieved according to Rees et al. methodology to estimate SRM resolution (*159*). Scale bars 500 nm.

Despite a considerable improvement in the resolution achieved, there were two main problems with the initial attempts at imaging platelets by dSTORM. Firstly, the fluorescent signal appeared to be dispersed and a kind of connectivity between the large concentrations that we assumed represented platelet alpha granules within the platelets was visible; not simply contained within granule-like structures as expected. It was noted that dSTORM data can often be difficult to interpret as labelling density, the algorithm selected and the brightness and density of blinking events can change the appearance of the final image and have implications for image interpretation and analysis (*157*). Also without any other examples of localisation microscopy techniques used in this context it was difficult to confirm our observations. Secondly, only one colour imaging was available on this system at this time, with no labelling to demarcate the edge of the platelet, it was difficult to predict whether vWF signal was from the platelet

identified, from non-specific labelling on the coverslip or from another platelet nearby. Following these results, the dSTORM system used was updated and two-colour imaging is now available. Therefore, an antibody against β-tubulin (referred to here as tubulin) was used, as had been in the literature (*231*), as a label for the perimeter of platelets and a widefield image taken to locate individual platelets.

Figure 35 dSTORM imaging of vWF and tubulin in platelets

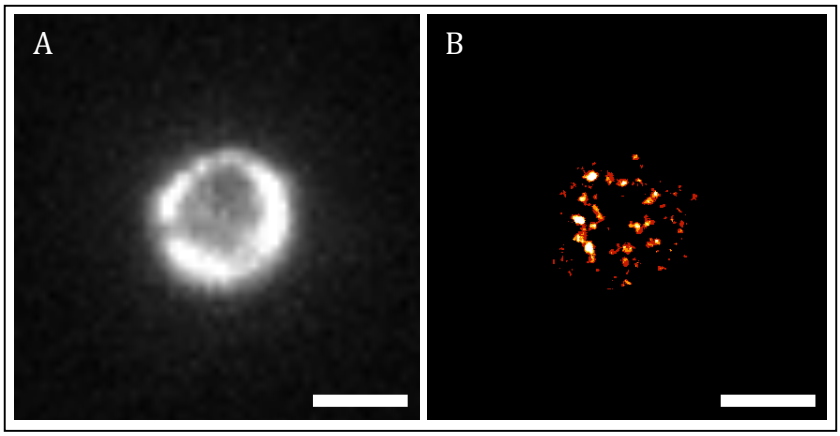

Widefield Tubulin (A) allowed identification of the location of platelet vWF (B). Scale bars 2 µm.

6.2.4 STORM imaging of platelets from patients with GPS

Although our SRM method was still in development, in order to see if this method could work we needed to test it on patients with a known PSD. Samples were obtained from patients with GPS, although this is only a preliminary data set (2 patients and 2 controls), it was used to test our hypothesis that a SRM methodology could be used to detect differences between a LRO-related genetic disorder (in this case GPS) and controls.

There have only been around 60 cases of GPS reported worldwide and through collaboration with Dr. Keith Gomez (Royal Free Hospital), I analysed the blood from two patients with GPS. These two patients would typically visit the clinic once a year (conversation with Keith Gomez) and were brother and sister, presenting with a mild thrombocytopenia and mild bleeding symptoms, their

father had been diagnosed with leukaemia which is what led to them to being screened, implying that he may also have had GPS.

We first processed the patient samples for TEM. Thin section TEM images of the patient's platelets compared with two controls (Figure 36) confirm the absence of alpha granules from both patient's platelets and suggest a disorganised canalicular membrane system. We next prepared samples to image with dSTORM (Figure 37) and stained for two markers of alpha granules, vWF and P-selectin.

Figure 36 TEM of Control and GPS platelets

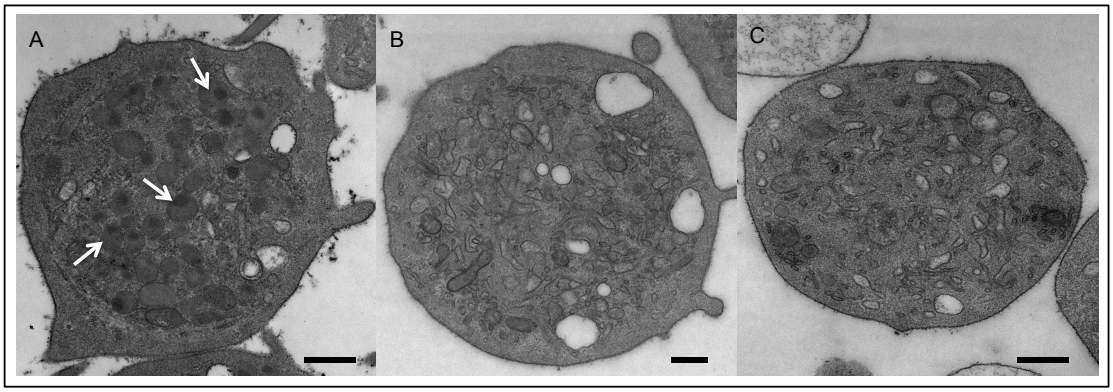

TEM thin sections of control (A) and two GPS patient's (B,C) platelets were prepared (as in 4.4.1) Granules assumed to be alpha granules can be seen in the control and absent from the GPS patients (white arrows). Scale bars 500 nm.

Figure 37 GPS patient platelets – dSTORM labelled with vWF and P-Selectin

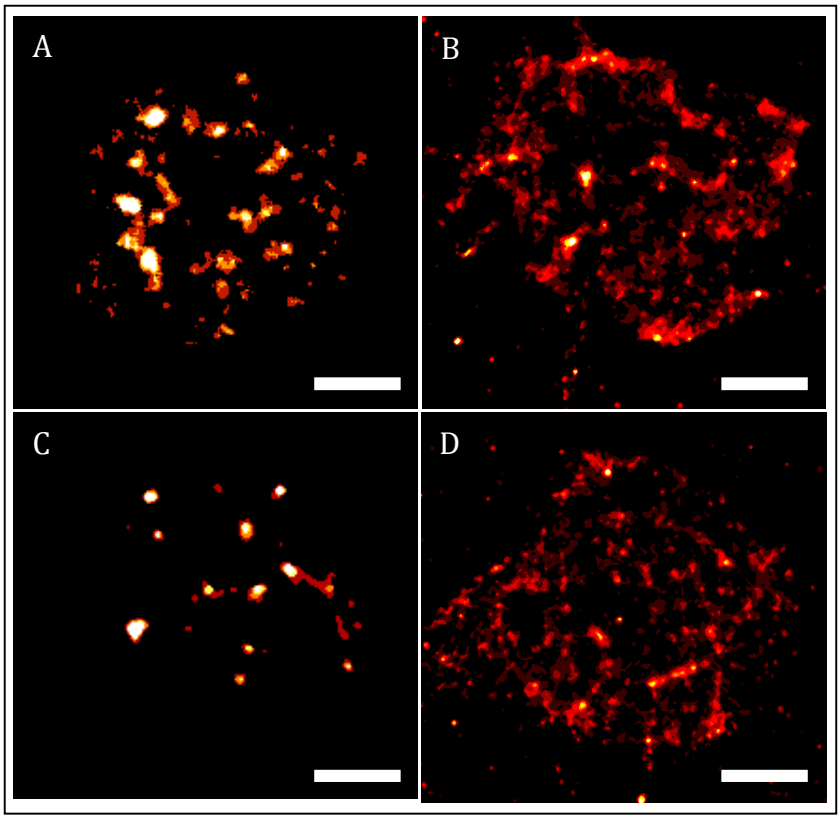

Representative dSTORM images from control (A,C) and GPS patient (B,D), immunolabelled for vWF (A,B) and P-Selectin (C,D). Scale bars 500 nm.

When analysed by dSTORM the antibodies targeted to vWF and P-Selectin were more diffuse in GPS patient platelets compared to controls (Figure 37). However, as discussed, the dSTORM technique and preparation methods limited the number of platelet images that were taken due to the time taken to acquire an image. To gain sufficient quantitative results more data was needed. These images, however, provided a first proof of principle that an SRM technique would be capable of distinguishing between controls and patients with a PSD that is characterised by a lack of granules (such as alpha granules in GPS); it also provided the first indication that the content of these granules may not be absent but diffuse/mislocalised within the platelet.

Because of the odd distribution of vWF, showing what appears to be connectivity between what we assumed to be the granules, we wondered whether this phenomenon was associated with alpha granules only, and whether this would also could be seen with a membrane protein marker of another LRO, the dense granule. Therefore, the potential of using immunofluorescence of a known marker of dense granules, CD63, was explored. CD63 is an itinerant integral membrane protein that traffics between post-Golgi organelles and has been found to be present on many secretory granules, endosomes and lysosomes, as well as LROs (*82*). Importantly, it has not only been shown to be present in dense granules but also has been reported to have fewer CD63 positive structures in HPS patients (*35*, *232*), a disorder characterised by a lack of dense granules. Given the diffuse staining observed in dSTORM images of vWF and with P-Selectin (Figure 32 and 33) a new SRM technique was employed, SIM. As platelet granules do not require the resolution achieved in dSTORM (around 25 nm in these images), SIM (which can achieve a resolution around 100 nm) could be a suitable technique. Furthermore, the images generated from SIM are not a result of post-processing localisation steps, therefore limiting the generation of potential artefacts and can produce images in a small fraction of the time taken to image by dSTORM.

6.2.5 Imaging CD63 in platelets by SIM

Figure 38 Imaging CD63 in platelets by SIM

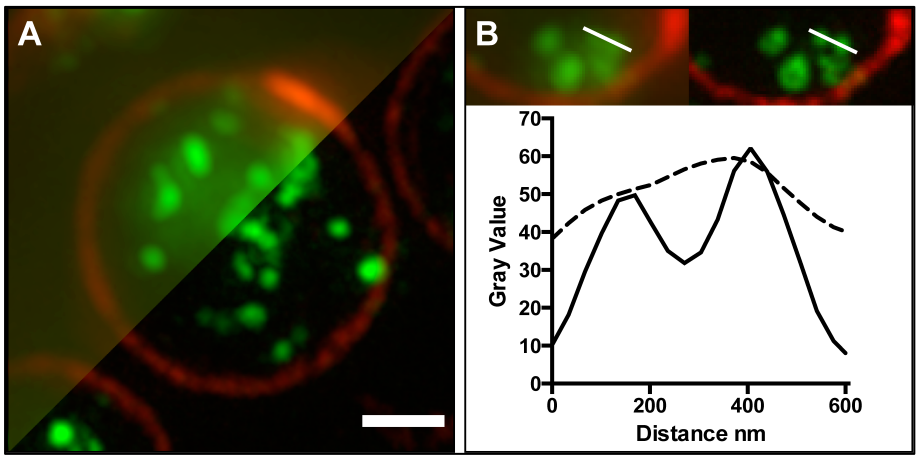

(A) Platelets were imaged by SIM (cut-away bottom right) with a diffraction-limited widefield microscopy image (cut-away upper left) shown for comparison. The images show the platelet perimeter (marginal band) labelled (red) with anti-tubulin and the internal structures (green), largely dense granules, labelled with anti-CD63 (B) The improved contrast and resolution in the SIM image (right) is clearly apparent from a 600 nm line profile (lower panel) taken through two closely adjacent structures. Scale bar: 1 µm

The improved spatial resolution and removal of out of focus background obtained by SIM is clearly apparent when compared to widefield microscopy (Figure 38). Platelets imaged using SIM and stained for tubulin and CD63 allowed us to clearly visualise granule-like structures within platelets (Figure 38). The resolution achieved with SIM meant individual granules could be clearly delineated. As such, we sought to develop an image-processing pipeline to segment CD63 positive-granules and platelets in SIM images.

Using a segmentation workflow established in collaboration with William Grimes (*164*) platelets were identified by their tubulin labelled structures and CD63 positive structures segmented. Examples of the outcome of these steps (Figure 39, Figure 40) are shown below (see also (*164*).

Figure 39 Platelet tubulin segmentation

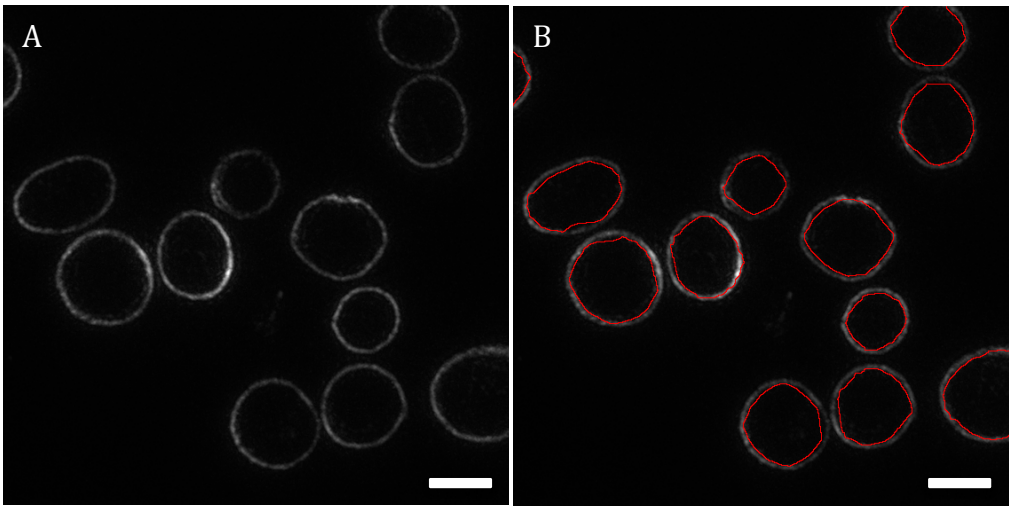

SIM image of tubulin labelled platelets (A) and image output with segmentation contours (B) that demonstrates the success of the segmentation protocol employed. Scale bars 1 µm.

Figure 40 Platelet CD63 segmentation

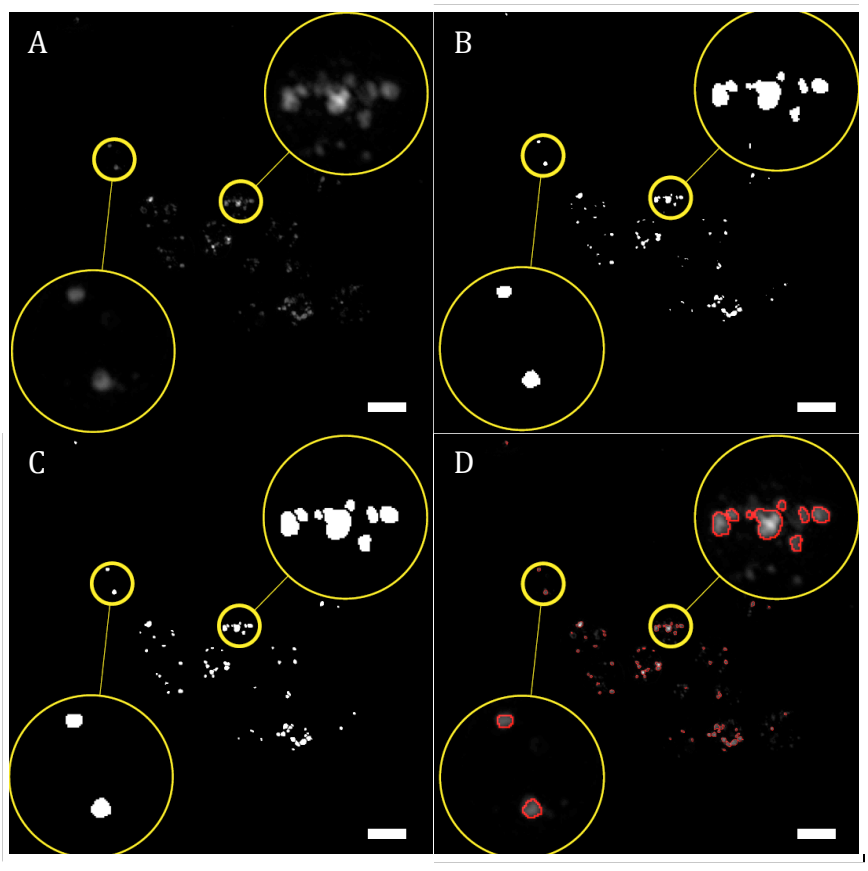

The major sequence of processes involved in segmentation of CD63-positive granules. A raw CD63 channel image (A) after moment-preserving thresholding applied in ImageJ (B). A watershed transform was used to distinguish overlapping structures (C). Segmentation contours applied over the original raw CD63 image (D), yellow magnified regions are used to demonstrate the accuracy of the segmentation. Segmentation protocol developed in collaboration with William Grimes, images from (*164*). Scale Bars 1.5 µm.

Once a protocol was established for identifying individual platelets and segmenting the CD63 positive granule content, an automated workflow was established (Figure 41) this allowed a bank of images of CD63 and tubulin labelled platelets to be rapidly analysed using an automated workflow that would automatically produce data regarding the number of CD63 positive structures per platelet.

Figure 41 SIM Segmentation workflow

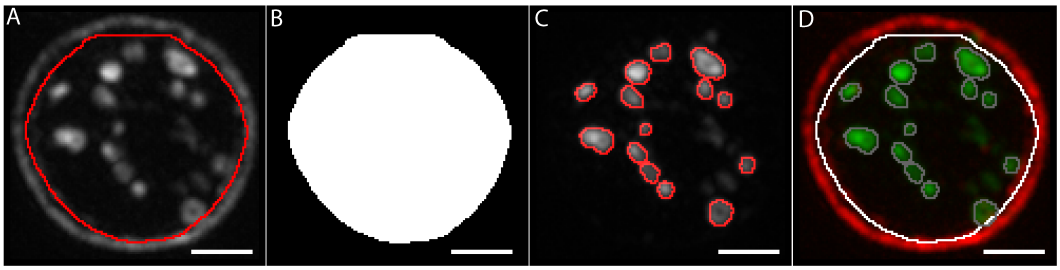

SIM images were analysed as follows; platelets were segmented using the image of the tubulin and corresponding CD63 image (A) and then filled (B). Platelets were distinguished from debris by their area and circularity. Granules within the filled area (B) were segmented according to a threshold value obtained from Moment-preserving thresholding (C). The platelet in which each CD63 granule is located was recorded (D) and morphometric features (including area) of each granule were measured. Scale bars: 1 µm.

Dense granules were identified by the presence of CD63 (*35*). As it has been reported that CD63 is present on dense granules, alpha granules and lysosomes (*25*, *35*), attempts were made to localise CD63 to dense granules by a correlative light and EM approach. Initially, it would have been attractive to simply compare CD63 immunofluorescent labelling, which relies on fixing and permeabilising the cells, directly with dense granules as visualised by the whole mount EM technique. However, a different approach was needed as dense granules as observed by whole mount EM were found to lose contrast after fixation (Figure 42).

Figure 42 Fixed Platelets imaged by Whole mount EM

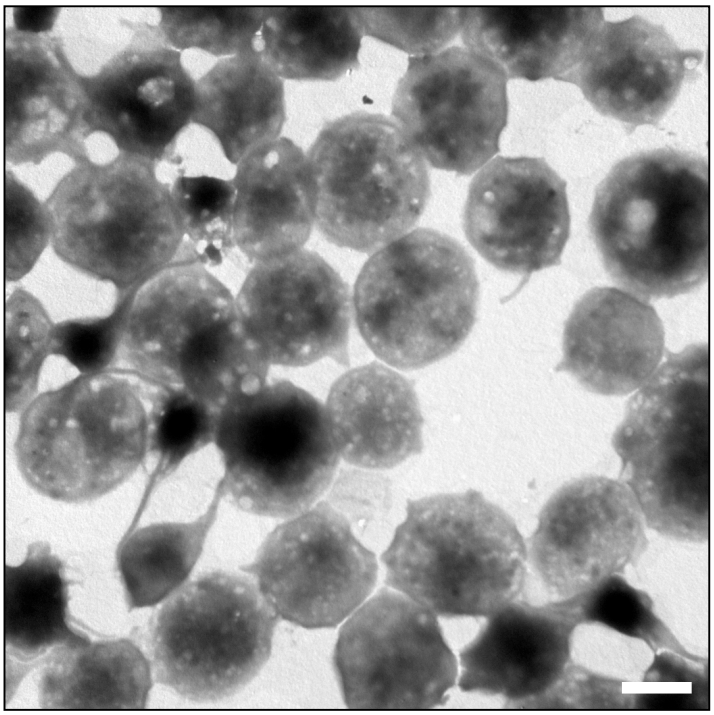

A representative image (n=10) to demonstrate that dense granules could not be identified by whole mount EM after fixation with 4% PFA for 15 minutes and centrifuged onto formvar coated copper EM grids. Scale bar 2 μm

A live-stain of dense granules, Mepacrine, was trialled as a potential comparator as it has been characterised as a label of dense granules when compared with whole mount EM detection of dense granules (*216*).

Figure 43 Mepacrine labelling of platelets

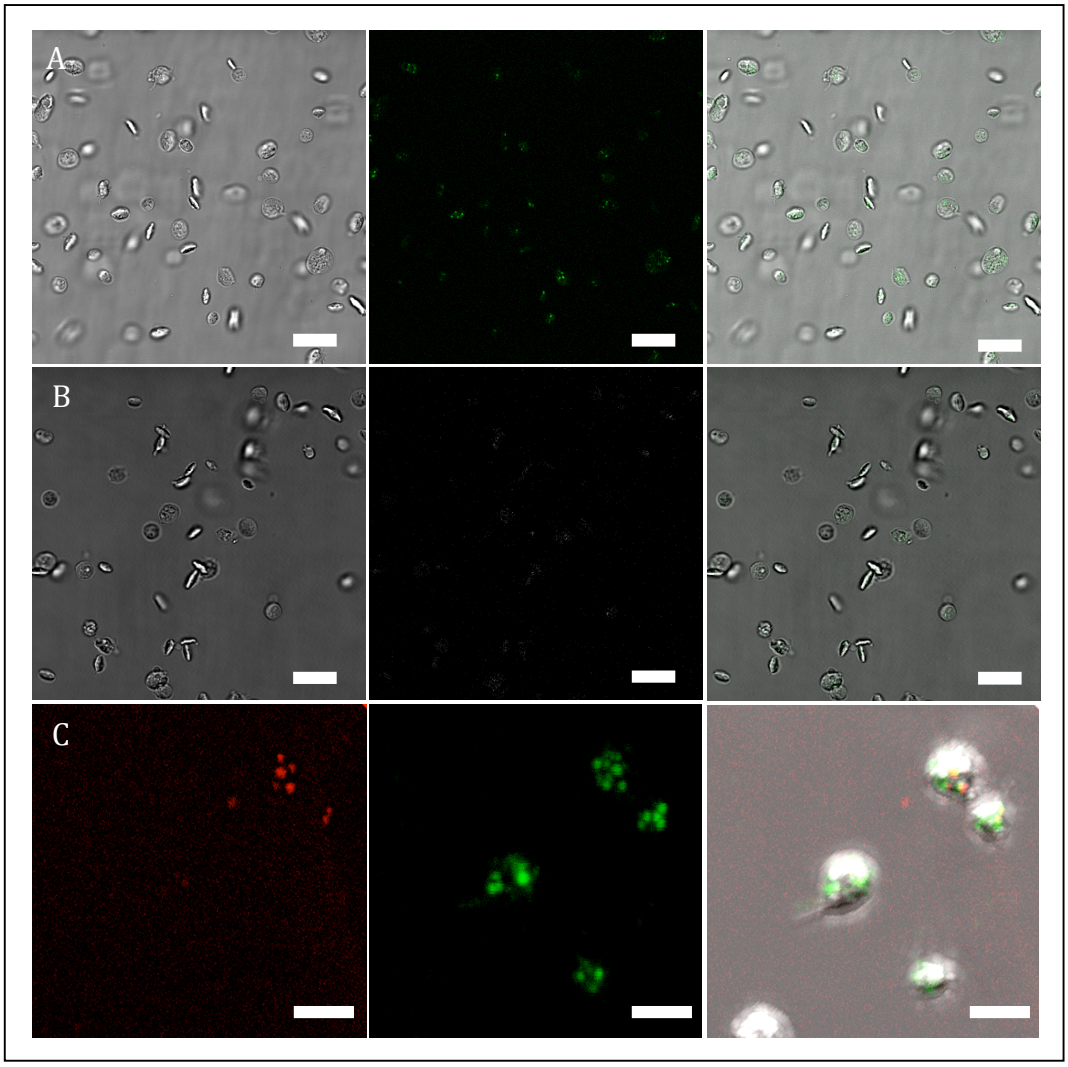

Mepacrine (green) labelled platelets (middle panel A, B) imaged within 1 hour (A) and 24 hours (B) of 15 minutes fixation with 4% PFA, images taken by fluorescent confocal microscopy and localization confirmed with transmission light images (left panel, A,B). Mepacrine labelled platelets (left Panel, C) colocalised with CD63 (middle panel, C) and combined image with transmission light (right panel, C) demonstrate that CD63 is labelling more structures within the platelet than mepacrine that has been labelled and imaged within 24 hours of fixation with 4% PFA. Scale Bars 10 um (Panels A and B scale bars 10 um, Panel C scale bars 2 µm)

Despite the widespread use of mepacrine in the literature, during this study it was found that fluorescent labelling rapidly bleaches and granules pop if looked at under the confocal microscope for more than around 10 seconds, and heterogeneous staining was also observed across the slide and between samples (data not shown). The mepacrine labelled fluorescence was also degraded after fixation (Figure 43A and B) and even though correlative images of CD63 and mepacrine labelled platelets were attempted (Figure 43C), the irregularity of the staining and the decay after fixation rendered this approach unusable.

As an alternative to characterise CD63 localisation a comparison between CD63 and other known granule markers by confocal microscopy was performed, to observe if there was any significant co-clustering between common granule markers reported in the literature. For this purpose the following antibodies were chosen; serotonin a marker of content in dense granules (*233*), vWF a marker of alpha granules (*40*) and P-Selectin which is found on the membranes of both alpha and dense granules (*217*).

Figure 44 Immunofluorescent colocalisation of CD63 in Platelets

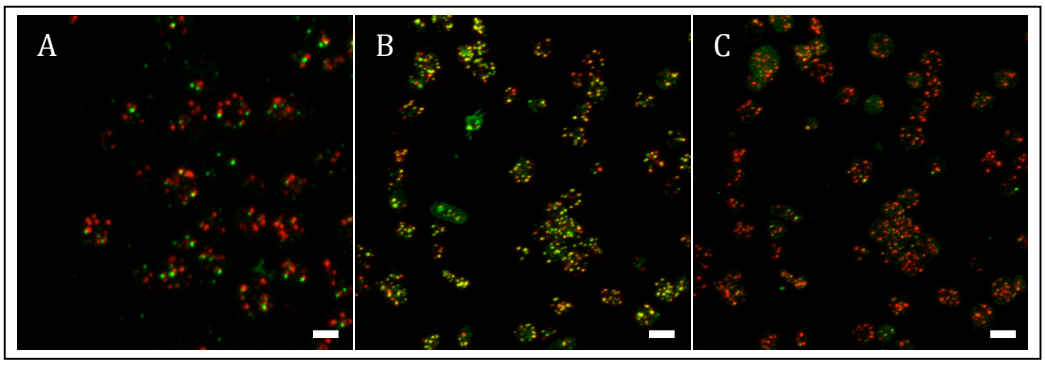

Representative images of platelet CD63 (A,B,C red) colocalisation imaged by confocal microscopy with vWF to mark alpha granules (A, Green), P-Selectin to mark alpha and dense granules (B, Green) and Serotonin to mark dense granules (C Green). Scale Bars 2 µm

Table 14 Colocalisation of CD63 with other platelet granule markers

	% colocalisation with CD63	% colocalisation of CD63 with
vWF	23%	7%
P-Selectin	60%	43%
Serotonin	39%	17%

The colocalisation of CD63 with a reported marker of alpha granules (vWF), dense granules (Serotonin) and both alpha and dense granules (P-Selectin) was explored. Using 'Imaris Coloc', automatic thresholds were set and the percentage colocalisation of three given markers (vWF, P-Selectin and Serotonin) was measured.

There was a weak positive correlation with vWF (Pearson's coefficient in dataset volume; 0.22), moderate with Serotonin (Pearson's coefficient in dataset volume; 0.54) and a strong correlation with P-Selectin (Pearson's coefficient in dataset volume; 0.72), correlation conclusions determined as in Dunn et al. (*234*). This may be explained by the fact that both CD63 and P-Selectin have been reported to be found on the membranes of alpha and dense granules (*30*, *217*). CD63 has historically been described as a dense granule marker (*35*), and a stronger

correlation with the dense granule marker serotonin was observed than with the alpha granule marker vWF. Since there was clearly some co-clustering with markers of both alpha and dense granule markers it was concluded that it was not possible to locate CD63 to a specific granule. However, it is likely that it is most similar to the distribution of P-selectin from the markers selected. This reaffirmed the belief that the focus on associating our analysis with which granule an antibody is labelling should be abandoned, and instead the distribution and number of granules relating to a given marker, regardless of which granules they were, was a more attractive and pragmatic method to characterise a PSD in this context.

6.2.6 Imaging CD63 in patients with HPS

The next aim was to use the segmentation protocol to image samples from patients with PSDs. To achieve the aim of diagnosing a PSD, SIM was chosen for its simplicity of sample preparation, compatibility with routinely used fluorescent labels and fast image acquisition rates. Platelet samples prepared by a simple robust protocol (see 4.1.2 for methods) were imaged on a custom-built SIM and, in parallel, by whole mount EM to provide a gold-standard diagnostic image-set for comparison.

Fixed platelets were centrifuged onto Poly-L-lysine coverslips to create a high density of platelets to analyse, since this dramatically reduces imaging time. Platelets were co-stained as before, using tubulin to demarcate the perimeter of individual platelets, within which segmented CD63-positive structures "granules" were individually located (Figure 43). This allowed the calculation of the number of granules per platelet, thus giving a more sensitive readout and allowed populations of individual platelets and content to be analysed.

Samples of platelets taken from three patients with HPS and from seven healthy volunteers were used to test the ability of SIM to differentiate between these groups. The three patients with HPS had a similar clinical phenotype, as all were

recorded as having oculocutaneous albinism from birth and a history of excessive bleeding after trauma. Patient 1 presented with pulmonary fibrosis but patients 2 and 3 did not. Platelet function assays performed by the Royal Free Hospital showed similar results between the patients in all three cases (data not shown) with reduced aggregometry to a standard panel of agonists and very low levels of platelet ADP documented by bioluminescent assay of nucleotide content in lysed platelets. A genetic analysis was performed by exome sequencing on the ThromboGenomics platform (more information see 4.8.1) that includes *HPS1*-9 and revealed that Patient 1 had compound heterozygosity for two single nucleotide deletions resulting in frameshifts and introducing premature stop codons in the *HPS1* gene (member of the BLOC-3 complex). Patient 2 had compound heterozygosity for two single nucleotide duplications resulting in frameshifts and introducing premature stop codons in the *HPS6* gene (member of the BLOC-2 complex). Patient 3 had homozygosity for a single nucleotide change introducing premature stop codons in the *HPS5* gene (member of the BLOC-2 complex), the controls were healthy volunteers.

Figure 45 Whole mount EM of Platelets

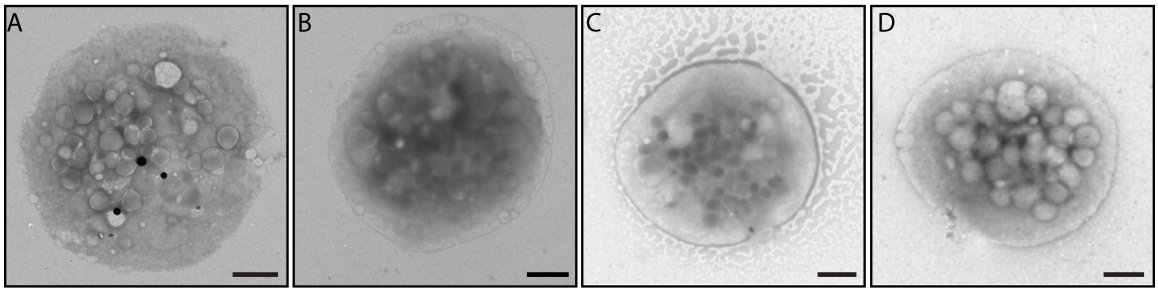

Analysis of dense granules by whole mount EM may be regarded as the "gold standard" for determining numbers of these organelles per platelet. Examples of single platelets from one of the 7 healthy volunteers (A) and from each HPS Patient 1, 2 and 3 (B,C,D) used in this study are shown. Note the lack of dense granules (black spots) seen in the HPS patients. The criteria for counting dense granules are described (see 4.4.2). Scale bars: 1 μm.

To compare with the current gold-standard technique, patient and control samples were processed for whole mount EM (Figure 45). A criteria was chosen to count dense granules (see 4.4.2) to reduce as much as possible the subjectivity in counting, the platelet images were taken by Jemima Burden (Head of EM facility LMCB) and the images randomised. Following this 1008 platelets were counted blindly by one person to remove any variation between analysts; a significant difference (99% confidence) was observed as very few of the patient

platelets had any dense granules when employing a strict methodology (Figure 46A).

An empirical cumulative distribution function (ECDF) plot (Figure 46B) of the number of dense granules per platelet demonstrates the clear distinction between the control and HPS patient populations. A Kruskal-Wallis (non-parametric) test was employed to compare the results from the two groups (due to the Poisson-like distribution of the dense granule counts), was used (Figure 46C). A significant difference was observed between the patient and control groups (99% confidence) and between each of the patients and all of the controls.

Figure 46 Whole mount EM analysis

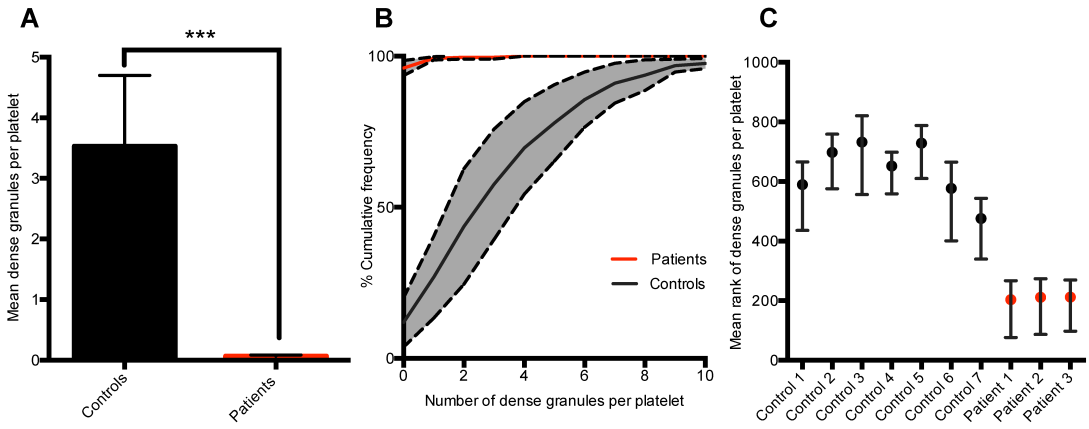

Dense granules were manually counted in 1008 platelets from randomised EM images of samples from seven healthy volunteers and three patients with HPS. There is a significant difference (99% confidence) between the mean number of dense granules per platelet between the seven controls and the three patients with HPS (A), when a strict counting protocol was employed (errors bars represent standard error of the mean). A cumulative frequency graph (B) reveals the spread of the data. A Kruskal Wallis Multiple Comparison Test (C) was used as the data had a Poisson-like distribution and thus a non-parametric test was needed. The mean rank of the three HPS patients was significantly different (99% confidence) from all of the controls. Figure from (*235*)

Having established that the three HPS patients lack dense granules as seen by EM, the same blood samples were analysed by SRM, co-labelling for CD63 and tubulin and counting the number of CD63-positive structures by SIM, using an automatic workflow (4.5.2) that did not rely on subjective counting methods.

Figure 47 SIM imaging of platelets from control and HPS patients

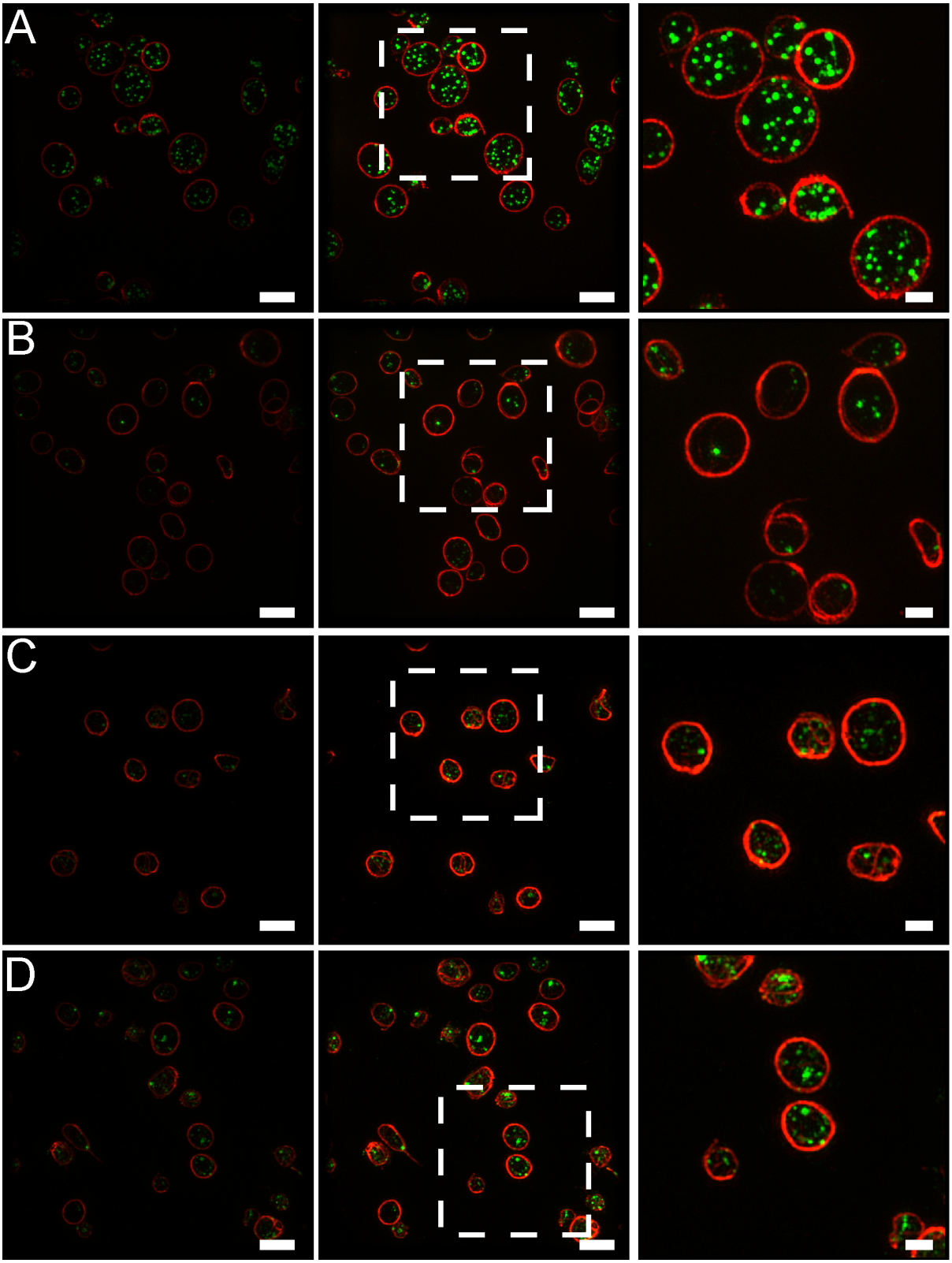

Example SIM images of platelets from one of the 7 healthy volunteers (A) and from each HPS Patient 1,2 and 3 (B,C,D) used. The images in the first column are an example of the raw SIM data as analysed (Figure 46), images in the second and third column have been similarly contrast enhanced for presentation. *z*-stacks are displayed as maximum intensity projections created using ImageJ. Scale bars: 4 µm for columns 1 and 2, 1.5 µm for column 3. Dashed boxes in column 2 highlight the area of the image displayed in column 3. CD63 (Green), Tubulin (Red).Figure from (*235*)

Figure 48 Analysis of SIM data

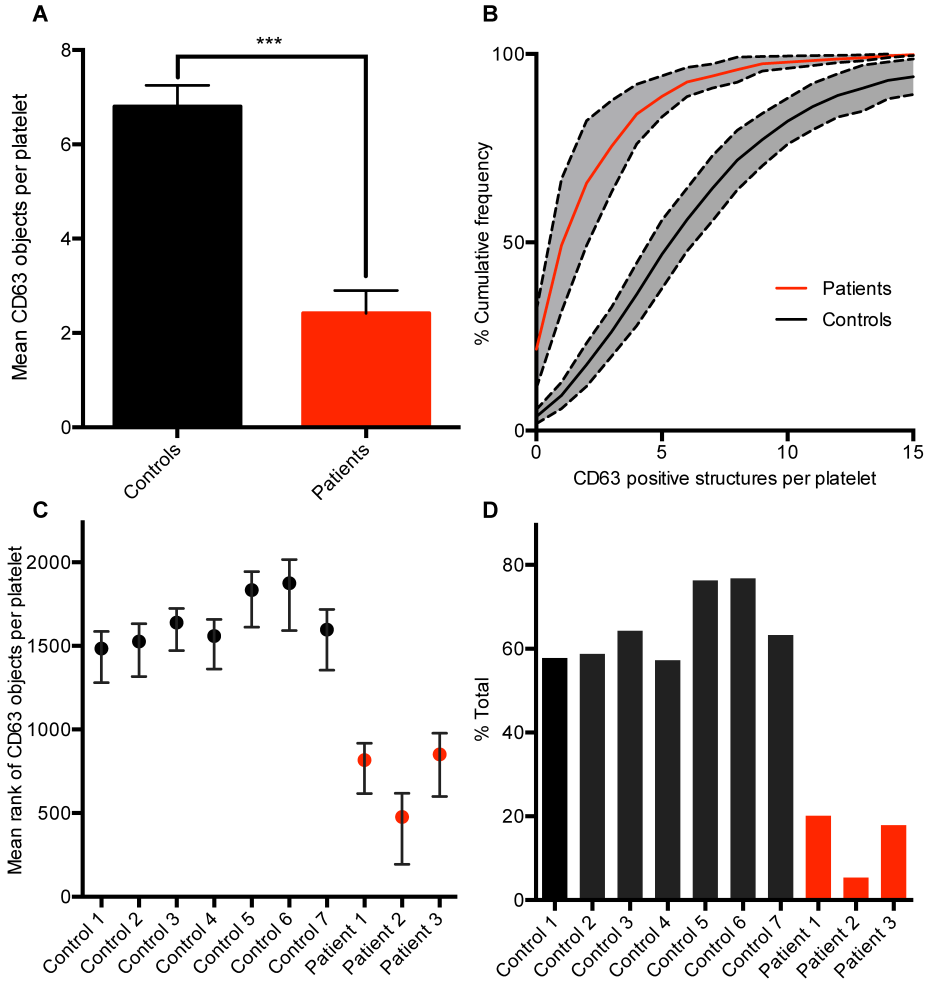

The number of CD63 objects per platelet was counted for 2812 platelets across 7 controls and 3 patients with HPS after segmentation. (A) A significant difference (99% confidence) was observed between the mean of the controls and the HPS patients (error bars represent standard error of the mean). A cumulative frequency graph (B) demonstrates the spread of the data. A Kruskal Wallis multiple comparison test (C) was used and the mean rank of the three HPS patients were significantly different (99% confidence) from all of the controls. An example of a potential readout for clinical use is displayed (D) in which the data is displayed as the percentage of platelets containing 4 or more CD63 positive structures.

The mean number of CD63-positive structures per platelet determined by SIM was 6.8 for controls, whereas for HPS patients it was 2.4 (Figure 48). A significant difference (99% confidence) was observed between the numbers of CD63 positive structures present in the platelets from the HPS patients compared to control (Figure 48A). An ECDF plot (Figure 48B) demonstrates a clear distinction between the control and HPS patient populations. As a non-parametric test was required to analyse significance (due to a Poisson- like distribution of the CD63 data), a Kruskal-Wallis multi comparison test was used to compare the results (Figure 48C) and a significant difference was seen between the controls and the patient groups (99% confidence) and between each of the patients and all of the controls, using a multiple comparison test

(99% confidence). To achieve a simplified readout that could be used as in a clinical context to rapidly assess the likelihood of a significant reduction in CD63-positive structures, a threshold of 4 or more CD63-positive structures per platelet was chosen and the proportion of platelets above this threshold was plotted in a bar chart (Figure 48D) this clearly demonstrates the differences between all the patients in the studies, and crucially, the significant difference between controls and patients.

During the SIM imaging of CD63 positive structures in platelets from both HPS patients and controls, an accumulation of CD63 fluorescent signal was observed close to the tubulin ring. This was not caused by bleed-through (fluorescence from a neighbouring channel incorrectly observed in the image of the channel of interest), evidenced by the fact that the tubulin signal did not always overlap with the CD63 signal at the surface. Interestingly, this phenomenon appeared only in the HPS patient data. This phenomenon aligns with other results observed in HPS studies where BLOC-1 deficient fibroblasts have been shown to present surface accumulation of CD63 (*114*) and AP-3 deficiency has also been shown to result in the increased surface expression of the lysosomal membrane proteins such as CD63 and therefore, this observation that CD63 appeared mislocalised was further investigated.

Together with William Grimes (PhD student Cutler Lab) a method to analyse the distribution of CD63 in patient and control platelets was created. The development of this technique did not require additional samples to be collected or more images to be taken as the images used to count CD63 positive structures could be re-analysed. To quantify the potential CD63 mislocalisation a number of factors were taken into consideration. As platelets can vary in size, it was important that the distance of the CD63 signal measured from the centre of each platelet was relative to the size of the platelet it was found. To achieve this the algorithm was designed so that each platelet was first segregated and given its own identity, the centre of the platelet plotted, a proportional length from centre to tubulin ring established (0 to 1, see Figure 49) and any pixels that displayed immunofluorescent signal representing CD63 were plotted according to where

this signal was found in along a series of concentric rings. This was repeated for every platelet in a set of images and the data displayed in a normalised radial distance plot (Figure 50E,F).

Figure 49 Schematic of Radial profile algorithm.

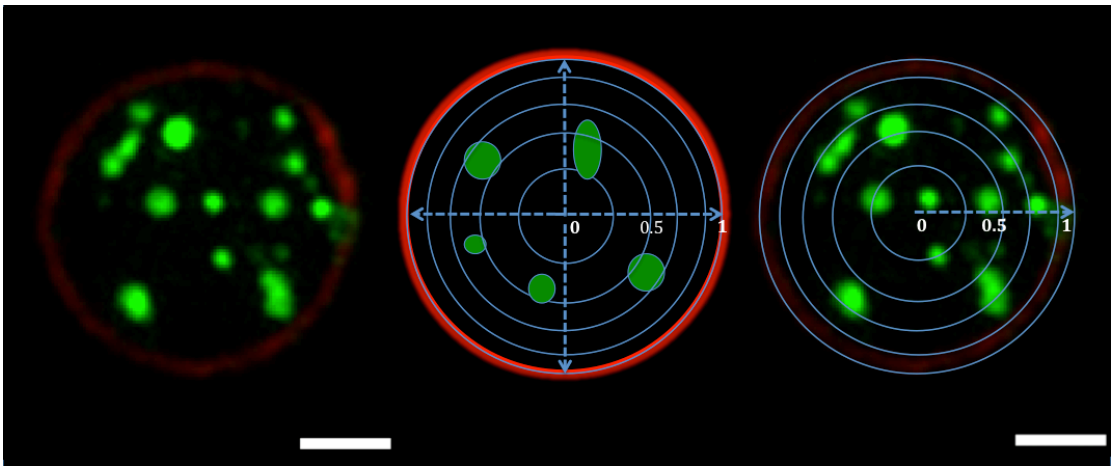

A SIM image of a Control platelet (left); the platelet perimeter (marginal band) was labelled (red) with anti-tubulin and the internal structures (green), largely dense granules, labelled with anti-CD63. The centre of the platelet is marked as 0 and the tubulin ring as 1. The platelet radius is defined as the distance from the centre of the platelet to the outer ring, where the outer ring is the maximum integrated intensity ring in the tubulin channel. The integrated intensity values are normalised for each concentric ring by division of the maximum integrated intensity ring of the platelet. Similarly, for each platelet, radial distances are normalised by division of the platelet radius. Normalization of both the radial distance and radial integrated intensity allows platelet distributions to be compared independent of the size of the platelet and the pixel intensities.

Figure 50 CD63 at the platelet surface in HPS platelets

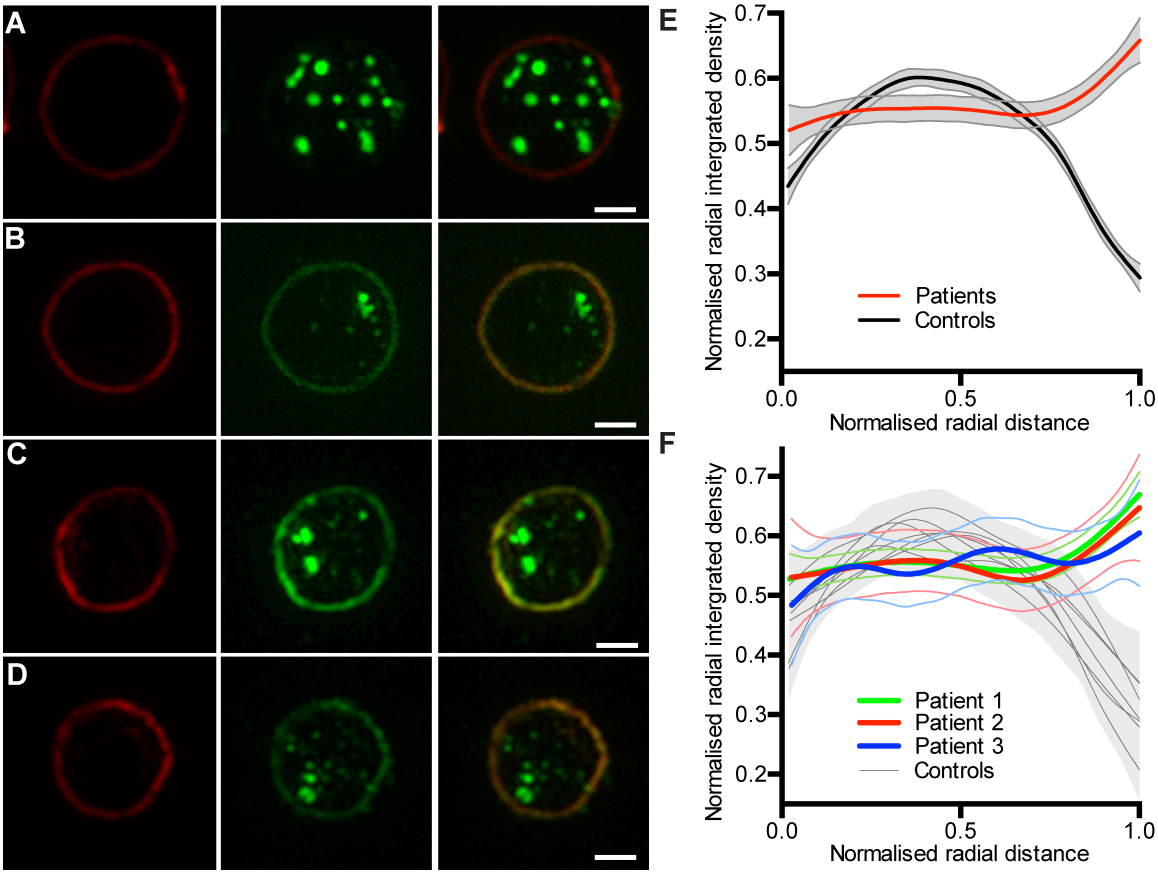

A platelet from Control 5 (A) and one from each of the HPS patients (B, C, D) imaged using SIM. Platelet perimeter (marginal band) labelled (red) with anti-tubulin in column 1 and the internal structures (green), largely dense granules, labelled with anti-CD63 in column 2. All CD63 images contrast enhanced to highlight surface staining. E represents the mean values of the controls and patients from F. All images were taken with identical settings for laser power, exposure time and background out-of focus light post-processing. Scale bars: 1 μm. Figure from (*235*)

A representative platelet is shown from the controls (Figure 50A) and each of the HPS patients (Figure 50B,C and D). The radial profile algorithm analysis, which calculates the normalised integrated intensity in a set of concentric rings (Figure 49), from the centre of each platelet (0 on the x axis in Figure 49e,f) to the platelet radius (1 on the X axis in Figure 50e,f), highlighted the difference in the location of CD63 in the HPS patients. Unlike the control, the three HPS patients have an accumulation of CD63 at the platelet surface, which had not previously been observed in platelets from HPS patients. This finding strengthens our overall conclusions and shows how a simple sample preparation imaged by SRM can provide two independent fully quantitative measures of a PSD such as HPS.

6.3 Discussion

The relationship between and roles of the different LROs and their biogenesis-associated complexes are still to be fully elucidated. This chapter focussed on the identification of LROs using different microscopy techniques with the aim of not only developing new techniques with which to study these organelles, but also to improve diagnosis in LRO related disorders. A new approach to define, identify and diagnose disorders that are related to both alpha and dense granules is required. In HPS, whilst it is well known that dense granules are reduced in number (*35*) there is no viable method of diagnosing a patient based on this fact, as all current techniques (including whole mount EM (limitations already discussed)) are difficult to standardise and/or require time consuming techniques (such as tomography, or serial section immuno-gold labelling cryosection TEM). Similarly, in GPS, the number of alpha granules is reduced (*88*); TEM of thin sections of fixed embedded platelets can be used to visualise alpha granules but sample preparation to achieve this is time-consuming and requires highly skilled technicians, and is therefore not practical to routinely implement in a clinical context. Recently, published FACs methods for diagnosing PSDs (*220*, *221*) do demonstrate additional ways to carry out functional tests of platelets, but as with all functional assays including LTA, can only be carried out immediately on site after the collection of samples. As discussed, LTA results are also difficult to interpret and often haematology centres will only trust their own results, making comparisons difficult. The aim in this chapter, therefore, was to improve the diagnosis of these disorders with the use of SRM.

The first technique employed was dSTORM. Despite this technique achieving the best resolution of the currently available SRM techniques, the imaging process has a number of caveats so that it would be difficult to automate and simplify in a clinical context. The development of this technique for platelet diagnostics was not sufficient to generate a data set large enough to quantify, however, a reduction in the punctate staining of these alpha granule markers was observed,

providing an indication that a SRM approach should be able to distinguish between patients and controls. The advanced imagine facility at NPL was used, which due to the distance from the lab at UCL and the Royal Free Hospital and the need to book time on the microscope weeks in advance, limited the amount of time available on the microscope. Although inconvenient, the lessons learnt from using dSTORM in this manner were invaluable for determining the conditions that were to be needed for a SRM technique to be transferred to a clinical setting. The complications found with sample transport, speed of acquisition, analysis and the variation seen in post-processing results were important considerations for designing a protocol more suitable for analysing a PSD that would be practical in a clinical setting. Firstly, to collect even a 2D image this method relies on localisation software to plot the average point spread functions of a large number of images (15,000 images typically in this study). Compared to other SRM techniques this reduces the speed of image acquisition possible, creates data-heavy results and introduces too many user-defined variables. Dependent on the density of the immuno-fluorescent labelling and the blink rate of the switching fluorophores, an experienced user will often change parameters such as the laser power and the time at which data is collected, depending on when the optimum blinking period is typically found. The time taken to acquire an image in this study was typically around 5-10 minutes which would create a bottle-neck in a clinical setting and require lab technicians to be trained to be reproducible in the imaging parameters that were changed between samples. As discussed, the main problems that are currently seen with PSD imaging techniques are reproducibility, variability in sample preparation and complexity of image acquisition; dSTORM seems unlikely to solve these issues. Samples prepared for dSTORM are also impractical to handle in a clinical setting as the glass bottom dishes or specially designed chambers required are relatively expensive compared to glass slides and coverslips, and the method relies on the sample being kept in liquid before the application of switching buffer, making the samples difficult to transport and store. Finally, and crucially, the resolution improvement gained by localisation microscopy techniques such as dSTORM, as compared to other SRM techniques such as SIM, is not required for the analysis of immunofluorescent antibodies that label

platelet granules; dense granules are around 150 nm and alpha granules 200-400 nm in diameter (*226*). The resolution achieved by the custom built SIM in NPL was typically around 100 nm. Therefore, despite promising early results seen with dSTORM analysing GPS (6.2.4), SIM was investigated as a possible tool for PSD disorder analysis.

From the currently available methods of SRM, SIM is the simplest of this class of instruments to use, as samples can be easily fixed in the same way that a typical sample would be prepared for fluorescent microscopy (see 4.3.3 for method). To acquire an image a Z-stack series of 20 images would typically take less than 10 seconds, allowing rapid acquisition of 3D images of platelets to be produced. Apart from bringing the platelets into focus (which can be automated), no user input was required before imaging. The samples could be 'dry' fixed on coverslips using Prolong Gold, which is inexpensive, requires no switching buffer and could be transported easily. In a clinical context, simply collecting PRP and mixing the platelets with fix for 15 mins before sending to a central facility for further processing would be possible. The resolution improvement seen using SIM was sufficient (Figure 38) to gain reproducible, significant results (Figure 48) that could be re-analysed at a later date for other variables (Figure 50). Further, it is more intuitive in a clinical context to acquire high resolution and high contrast data directly, rather than the user having to make decisions based on localisation and labelling efficiency to improve image quality and thus potentially altering the result seen.

The dense granule abnormalities caused by HPS were investigated using CD63 as a marker. CD63 is an itinerant integral membrane protein that traffics between post-Golgi organelles (*82*) and was selected as it has been shown to be present in dense granules and reported to have an altered distribution in HPS patients with a lower number of CD63-positive structures counted (*35*, *232*). However, the published data was achieved in a low throughput manner and performed with microscopy techniques that do not have the resolution to accurately count these structures, and this may help explain why, to date, immunofluorescent antibody labelling techniques have not been utilised for clinical diagnosis.

Using immunofluorescent antibodies to count alpha and dense granules does not come without caveats. The platelet granules are distinct but many markers that are claimed to label alpha granules and dense granules do not share the same structures when analysed by immunofluorescence. For example, Kamykowski et al. report that 15 different markers for alpha granules fail to show any significant co-clustering (*212*). Also CD63, a reported marker of dense granules can also label lysosomes and alpha granules (*25*). This could be seen as a weakness or strength of an immunofluorescent labelling approach. The platelet granules have historically been defined by their appearance in EM and for routine diagnostic purposes it could be argued that it is counter-productive to categorise granules as alpha and dense granules in this manner, as there is no efficient technique to analyse both within a large number of platelets and there are no techniques that are devoid of subjective identification. An unbiased, automated technique of counting structures that are positive for antibodies that are known to be reduced in a PSD, is potentially a more accurate and reproducible method for defining both PSD and granules themselves and this approach could improve the chances of detecting new markers of disease.

The sensitivity of this analysis by SIM is demonstrated by the ability of this technique to distinguish between three HPS patients and seven controls (99% confidence) in the number of CD63 positive structures and also in the distribution of CD63 within the platelets. After using a one-sample t-test for the two populations (patients versus controls) it was concluded that a sample size of just 25 platelets would be sufficient to give a similar probability of detection of HPS from the platelets analysed in this study. In this study an average of 281 platelets per person was analysed. HPS, however, is a very clearly differentiated defect, therefore, since sampling a large number of platelets does not affect the time, cost or sample size required, this method could potentially be used to detect much less severe phenotypes if needed. If required, it would also be relatively easy to analyse even larger numbers of platelets to further increase sensitivity for other disorders. The counting of CD63-positive structures by SIM on 2812 platelets (in total) was achieved in our study in less than 5% of the time

needed for the manual analysis of 1008 platelets (in total) by the gold standard whole mount EM technique, yet both gave a significant difference between the HPS patients and the controls. The mean number of CD63-positive structures for controls is roughly twice as many as for dense granules as counted by EM; 3.5 as opposed to 6.8. This may be in part due to the presence of CD63 on other organelles within the platelets, as expected for such an itinerant membrane protein, this could also be due to the criteria set to count dense granules in whole mount EM which was intentionally strict (4.4.2). However, despite this difference in baseline, the important conclusion is that either by whole mount EM or SIM, a highly significant difference between controls and patients was observed (Figure 46, Figure 48), and therefore SRM could replace whole mount EM as an effective determinant of a platelet dense granule disorder.

The improved resolution possible with SRM compared to other light microscopy techniques potentially allows subtle changes of morphology from large datasets to be detected; helping clinicians to diagnose patients with more certainty. This may also lead to the identification of novel symptoms within genetic subtypes of a disorder such as HPS, which until now have not been observed. To analyse the images an automated workflow was written as an ImageJ macro that allowed CD63 positive structures to be counted rapidly and without subjectivity. An automatic thresholding value set by 'Moments' in ImageJ (*169*) selected the parameters automatically and thus results could be easily compared between different analysts without any subjective analysis. The methodology detailed in this study could be further automated with a microscope capable of autofocusing and screening a number of samples at a time. An example of a simple readout, the percentage of platelets with 4 or more CD63 positive structures could be used as an initial detection of HPS (Figure 48). An improvement in the efficiency of platelet imaging was also explored, as centrifugation of fixed platelets onto poly-lysine coated coverslips reduced the amount of PRP required to produce 96 coverslips of platelets with a high density in each image, to less than 1 ml. As all patients with HPS have a bleeding disorder (*37*), it would therefore be an attractive proposition to potentially scale down the collection of blood to a simple pin prick.

The advantage of a high-throughput quantitative automated methodology is that it can be further extended by the addition of other marker-specific immuno-probes to simultaneously quantify other platelet structures if needed. Parameters such as size and the shape of organelles, as well as novel parameters that arise, such as the fraction of any membrane protein on the platelet surface, could also be easily extracted from the morphometric datasets. This would expand the number of disorder markers within one data set, without the need for a patient to revisit the clinic. An example of this was discovered during this study when a surface accumulation of CD63 was observed (Figure 50) and found to be significantly different in HPS patients compared to controls. The ability to be able to revisit the data and look for a different marker of HPS revealed a potential new disease phenotype of HPS that could help improve the sensitivity of detection. This is important as new approaches to PSD diagnostics are required, in 2013 it was reported that 76% of patients with HPS were initially misdiagnosed and 28% of patients had to see 4 to 6 specialists before receiving the correct diagnosis (*98*). Fixed platelets are stable for several months at 4^{o}C and could be sent to a central facility for diagnosis by SIM and imaged/re-analysed at a later date if required, relieving local hospitals of the burden of equipment acquisition and training.

Although SRM has not been used in a clinical setting, it is likely to become much more widely available as the benefits are demonstrated. Publications relating to SIM have increased rapidly (Figure 51) since the first demonstration of this technique by Gustaffson in 2000 (*147*), and therefore it is should not be considered a negative point that this technique has not yet been employed, but rather considered a matter of time.

Figure 51 Publications related to SIM

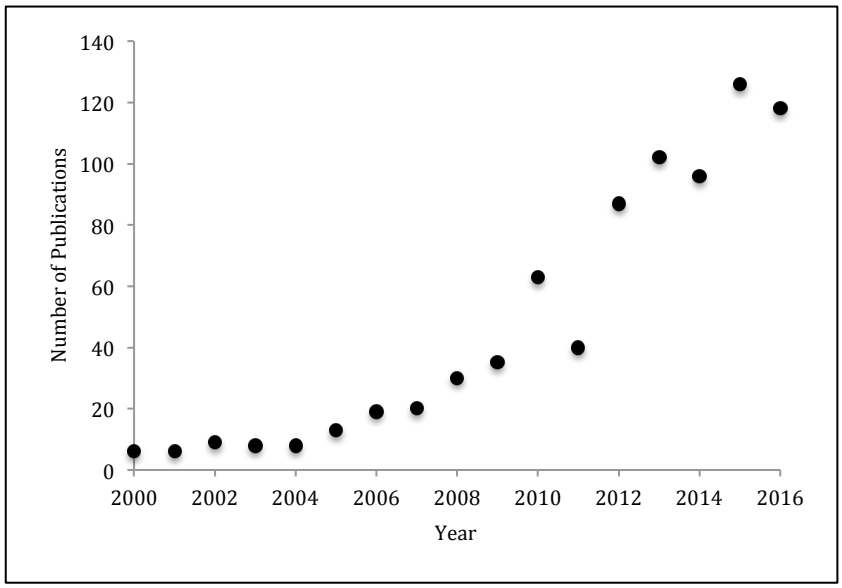

The frequency of publications per year related to SIM since 2000, data acquired from www.pubmed.gov

In this chapter two SRM techniques, STORM and SIM, were employed to analyse markers of platelet granules in patients with PSDs. Our results suggest that an immunofluorescent diagnosis using SIM could make a valuable addition to the diagnosis of patients with PSDs. The data in this chapter demonstrates that a SRM approach coupled to morphometric analyses could be an effective and rapid approach to differentiating between a patient with a platelet bleeding disorder and healthy volunteers.

7 Summary

Firstly, the roles of the proteins that are mutated in an LRO-related disorder, HPS, were further explored. There is little evidence in the literature of the function of HPS-related proteins and their complexes in human cells and no link between these and WPBs in endothelial cells. The secretion of vWF into the blood flow is one of the primary functions of WPBs and attempts were made to measure the effect of siRNA ablation on HPS related proteins on the regulated secretion of vWF in culture HUVECs. Initially, a KD of BLOC-1 by a siRNA targeted to *Pallidin* resulted in a significant increase in vWF secretion. A significant reduction in WPB feret diameter was also observed and preliminary experiments suggested that there was a reduction in high molecular weight multimers of vWF and an increase in vWF exocytic sites. However, when the secretion of vWF was further tested with other siRNAs targeted towards *Pallidin* the phenotype was not reproducible. As there is a lack of reliable antibodies to measure the efficiency of the BLOC-1 protein levels by a western blot, this meant that off-target effects could not be ruled out. Similarly a KD of BLOC-3, by a siRNA targeted towards *HPS1*, also resulted in an increase in vWF secretion. This phenotype was not reproducible when the secretion assays were performed with other *HPS1* siRNA sequences and as there is also a lack of reliable antibodies to measure the efficiency of BLOC-3 protein levels in the cell, this meant that off-target effects could not be ruled out. In conclusion, we were not able to confirm the role of HPS-related proteins in WPB formation and function.

In parallel a method to improve the detection, quantification and diagnosis of LRO-related disorders was undertaken. Current methodology does not allow the morphology or number of platelet alpha and dense granules to be reliably assessed in patients with a PSD. An automated, unbiased methodology was employed using SRM which allowed platelet granules to be resolved and in preliminary data demonstrated a difference in the localisation of platelet alpha granule markers vWF and P-selectin, between two patients with GPS and two controls using dSTORM. The methodology was improved when using SIM, as the

resolution improvement over SIM, achieved in dSTORM, was not required to resolve platelet granules and the simpler preparation and analysis of platelet samples would be more suitable in a clinical context. An analysis of SIM on the number of CD63 positive structures (a marker primarily of dense granules) in platelets from patients with HPS, concluded that a significant reduction in number of these structures per platelet was observed in three patients compared to seven controls. This result was comparable to that achieved with whole mount EM of dense granules and was achieved without subjective counting, in less time and was performed on fixed platelets that could be easily transported or re-analysed in a clinical setting. The ability to measure a PSD using immunofluorescence microscopy has many advantages and will hopefully lead to a more sensitive analysis, not only of HPS, but other PSDs where a change in the morphology, location or number of platelet granule markers could be used to diagnose patients. An example of the power of this analysis was provided when an observation that the location of CD63 within the platelet had altered in HPS patients was tested. Without the need to obtain further samples, an automated and unbiased methodology was developed to measure the location of CD63 within each platelet and from this a significant difference between the three patients and seven controls was observed. This new diagnostic method has the potential to improve PSD diagnosis; an automated SRM could aid the characterisation of HPS and other PSDs and also improve the sensitivity of diagnosis by enabling the detection of specific populations of granules and the localisation of markers that are affected by a given mutation.

The current literature has emphasised the similarities between LROs, yet despite this, the molecular and cellular basis for this group is still incomplete. To expand on this research, it will be necessary to continue to explore the effects of proteins mutated in LRO-related disorders in their host cells, to gain further information about their roles in intracellular trafficking. This will not only improve our understanding of LRO formation and function, but also facilitate in the categorisation of this group of organelles as whole. In parallel new diagnostic techniques are not only needed to improve the treatment of patients suffering

from these disorders but are also important for potentially improving the analysis of future LRO-related studies.

8 Bibliography

1. E. C. Dell'Angelica, Lysosome-related organelles. *FASEB J.* **14**, 1265–1278 (2000).
2. G. Raposo, M. S. Marks, D. F. Cutler, Lysosome-related organelles: driving post-Golgi compartments into specialisation. *Curr. Opin. Cell Biol.* **19**, 394–401 (2007).
3. M. Huizing, A. Helip-Wooley, W. Westbroek, M. Gunay-Aygun, W. A. Gahl, Disorders of Lysosome- Related Organelle Biogenesis: Clinical and Molecular Genetics *. *Annu. Rev. Genomics Hum. Genet*. **9**, 359–86 (2008).
4. R. T. SWANK *et al.*, Abnormal Vesicular Trafficking in Mouse Models of Hermansky-Pudlak Syndrome. *Pigment Cell Res.* **13**, 59–67 (2000).
5. W. K. Silvers, *The Coat Colors of Mice* (Springer-Verlag, 1979).
6. S. C. Birbeck, N. A. Barnicot, R. Cancer, the Structure and Formationofpigment Granules in Human Hair. *Exp. Cell Res.* **514**, 505–514 (1956).
7. A. H. Wei, X. He, W. Li, Hypopigmentation in Hermansky-Pudlak syndrome. *J. Dermatol.* **40**, 325–329 (2013).
8. A. Sitaram, M. S. Marks, Mechanisms of protein delivery to melanosomes in pigment cells. *Physiology (Bethesda).* **27**, 85–99 (2012).
9. M. S. Marks, H. F. G. Heijnen, G. Raposo, Lysosome-related organelles: Unusual compartments become mainstream. *Curr. Opin. Cell Biol.* **25**, 495–505 (2013).
10. A. R. Hellström *et al.*, Inactivation of PMEL alters melanosome shape but has only a subtle effect on visible pigmentation. *PLoS Genet.* **7**, e1002285 (2011).
11. C. E. Futter, D. F. Cutler, *J. Cell Biol.*, in press (available at http://jcb.rupress.org/content/214/3/245.abstract).
12. R. Sarangarajan, R. E. Boissy, Review : Pigment Gene Focus Tyrp1 and Oculocutaneous Albinism Type 3. *Pigment Cell Res.* **14**, 437–444 (2001).

13. R. A. Jani, L. K. Purushothaman, S. Rani, P. Bergam, S. R. G. Setty, STX13 regulates cargo delivery from recycling endosomes during melanosome biogenesis. *J. Cell Sci.* **128**, 3263–76 (2015).
14. C. Delevoye *et al.*, BLOC-1 Brings Together the Actin and Microtubule Cytoskeletons to Generate Recycling Endosomes. *Curr. Biol.* **26**, 1–13 (2016).
15. G. Raposo, M. S. Marks, Melanosomes — dark organelles enlighten endosomal membrane transport. *Nat. Rev. Mol. Cell Biol.* **8**, 786–797 (2007).
16. S. Vijayasaradhi, Y. Xu, B. Bouchard, A. N. Houghton, Intracellular sorting and targeting of melanosomal membrane proteins: Identification of signals for sorting of the human brown locus protein, GP75. *J. Cell Biol.* **130**, 807–820 (1995).
17. B. Bouchard, B. B. Fuller, S. Vijayasaradhi, a N. Houghton, Induction of pigmentation in mouse fibroblasts by expression of human tyrosinase cDNA. *J. Exp. Med.* **169**, 2029–42 (1989).
18. J. F. Berson, D. C. Harper, D. Tenza, G. Raposo, M. S. Marks, Pmel17 initiates premelanosome morphogenesis within multivesicular bodies. *Mol. Biol. Cell*. **12**, 3451–64 (2001).
19. H. H. Versteeg, J. W. M. Heemskerk, M. Levi, P. H. Reitsma, New fundamentals in hemostasis. *Physiol. Rev.* **93**, 327–58 (2013).
20. E. M. Golebiewska, A. W. Poole, Platelet secretion: From haemostasis to wound healing and beyond. *Blood Rev.* **29**, 153–162 (2015).
21. F. Storti, T. H. S. van Kempen, F. N. van de Vosse, A continuum model for platelet plug formation and growth. *Int. j. numer. method. biomed. eng.* **30**, 634–658 (2014).
22. H. Rasche, *Eur. Hear. Journal, Suppl.*, in press, doi:10.1016/S1520-765X(01)90034-3.
23. S. Falati, P. Gross, G. Merrill-Skoloff, B. C. Furie, B. Furie, Real-time in vivo imaging of platelets, tissue factor and fibrin during arterial thrombus formation in the mouse. *Nat Med*. **8**, 1175–1181 (2002).
24. A. J. Gale, Continuing education course #2: current understanding of hemostasis. *Toxicol. Pathol.* **39**, 273–80 (2011).

25. H. Van Nispen Tot Pannerden *et al.*, The platelet interior revisited: Electron tomography reveals tubular ??-granule subtypes. *Blood*. **116**, 1147–1156 (2010).
26. K. Freson, A. Wijgaerts, C. van Geet, Update on the causes of platelet disorders and functional consequences. *Int. J. Lab. Hematol.* **36**, 313–325 (2014).
27. J. E. Italiano, Unraveling mechanisms that control platelet production. *Semin. Thromb. Hemost.* **39**, 15–24 (2013).
28. P. Blair, R. Flaumenhaft, Platelet ??-granules: Basic biology and clinical correlates. *Blood Rev.* **23**, 177–189 (2009).
29. T. Youssefian, E. M. Cramer, Megakaryocyte dense granule components are sorted in multivesicular bodies. *Blood*. **95**, 4004–7 (2000).
30. H. F. Heijnen *et al.*, Multivesicular bodies are an intermediate stage in the formation of platelet alpha-granules. *Blood*. **91**, 2313–2325 (1998).
31. J. N. Thon *et al.*, T granules in human platelets function in TLR9 organization and signaling. *J. Cell Biol.* **198**, 561–574 (2012).
32. R. Meng *et al.*, Defective release of α granule and lysosome contents from platelets in mouse Hermansky-Pudlak syndrome models. *Blood*. **125**, 1623–32 (2015).
33. A. T. Nurden, P. Nurden, Congenital platelet disorders and understanding of platelet function. *Br. J. Haematol.* **165**, 165–178 (2014).
34. R. T. SWANK, E. K. NOVAK, M. P. McGARRY, M. E. RUSINIAK, L. FENG, Mouse Models of Hermansky Pudlak Syndrome: A Review. *Pigment Cell Res.* **11**, 60–80 (1998).
35. M. Nishibori *et al.*, The protein CD63 is in platelet dense granules, is deficient in a patient with hermansky-pudlak syndrome, and appears identical to granulophysin. *J. Clin. Invest.* **91**, 1775–1782 (1993).
36. C. J. Witkop, M. Krumwiede, H. Sedano, J. G. White, Reliability of absent platelet dense bodies as a diagnostic criterion for Hermansky-Pudlak syndrome. *Am. J. Hematol.* **26**, 305–11 (1987).
37. S. L. Seward, W. A. Gahl, Hermansky-Pudlak Syndrome: Health Care Throughout Life. *Pediatrics*. **132**, 153–160 (2013).
38. A. D. Michelson, Gray platelet syndrome. *Blood*. **121**, 250 (2013).

39. R. C. Becker, D. Voora, S. H. Shah, *Hemostasis and Thrombosis* (Lippincott Williams {&} Wilkins, 2013; http://www.amazon.es/Hemostasis-Thrombosis-Victor-J-Marder/dp/1608319067/ref=sr_1_1?ie=UTF8&qid=1412849658&sr=8-1&keywords=9781608319060), vol. 2 of *Basic Principles And Clinical Practice*.
40. S. W. Whiteheart, Platelet granules: surprise packages. *Blood*. **118**, 1190–1191 (2011).
41. K. R. Machlus, J. N. Thon, J. E. Italiano, Interpreting the developmental dance of the megakaryocyte: A review of the cellular and molecular processes mediating platelet formation. *Br. J. Haematol.* **165**, 227–236 (2014).
42. M. Gunay-Aygun *et al.*, NBEAL2 is mutated in gray platelet syndrome and is required for biogenesis of platelet alpha-granules. *Nat Genet*. **43**, 732–734 (2011).
43. H. P. Lorez *et al.*, Storage Pool Disease: Comparative Fluorescence Microscopical, Cytochemical and Biochemical Studies on Amine-Storing Organelles of Human Blood Platelets. *Br. J. Haematol.* **43**, 297–305 (1979).
44. E. G. Popov, A. G. Mejlumian, I. Y. Gavrilov, Z. A. Gabbasov, E. Y. Pozin, Evaluation of the ability of intact platelets to accumulate acridine organge. *Experientia*. **44**, 616–618 (1988).
45. G. Anfossi, M. Trovati, Role of catecholamines in platelet function: pathophysiological and clinical significance. *Eur.J Clin.Invest*. **26**, 353–370 (1996).
46. F. A. Ruiz, C. R. Lea, E. Oldfield, R. Docampo, Human platelet dense granules contain polyphosphate and are similar to acidocalcisomes of bacteria and unicellular eukaryotes. *J. Biol. Chem.* **279**, 44250–44257 (2004).
47. F. Rendu, B. Brohard-Bohn, The platelet release reaction: granules' constituents, secretion and functions. *Platelets*. **12**, 261–273 (2001).
48. R. Goggs, C. M. Williams, H. Mellor, A. W. Poole, Platelet Rho GTPases – a focus on novel players, roles and relationships. *Biochem. J*. **466**, 431–442 (2015).
49. A. D. Michelson, in *Platelets* (2007;

http://public.eblib.com/EBLPublic/PublicView.do?ptiID=1048862), pp. 825–830.

50. S. J. Israels *et al.*, Platelet dense granule membranes contain both granulophysin and P-selectin (GMP-140). *Blood*. **80**, 143–152 (1992).
51. R. Shirakawa *et al.*, Munc13-4 Is a GTP-Rab27-binding Protein Regulating Dense Core Granule Secretion in Platelets. *J. Biol. Chem.* **279**, 10730–10737 (2004).
52. T. Tolmachova, M. Abrink, C. E. Futter, K. S. Authi, M. C. Seabra, Rab27b regulates number and secretion of platelet dense granules. *Proc. Natl. Acad. Sci. U. S. A.* **104**, 5872–7 (2007).
53. D. C. Barral *et al.*, Functional redundancy of Rab27 proteins and the pathogenesis of Griscelli syndrome. *J. Clin. Invest.* **110**, 247–257 (2002).
54. D. J. Metcalf, T. D. Nightingale, H. L. Zenner, W. W. Lui-Roberts, D. F. Cutler, Formation and function of Weibel-Palade bodies. *J. Cell Sci.* **31**, 882–888 (2008).
55. E. R. WEIBEL, G. E. PALADE, New Cytoplasmic Components in Arterial Endothelia. *J. Cell Biol.* **23**, 101–112 (1964).
56. D. D. Wagner, J. B. Olmsted, V. J. Marder, Immunolocalization of von Willebrand protein in Weibel-Palade bodies of human endothelial cells. *J. Cell Biol.* **95**, 355–360 (1982).
57. National Heart Lung and Blood Institute, What Is Von Willebrand Disease? (2011), (available at http://www.nhlbi.nih.gov/health/health-topics/topics/vwd).
58. Y.-F. Zhou *et al.*, Sequence and structure relationships within von Willebrand factor. *Thombosis Hemost.* **120**, 449–458 (2012).
59. P. J. Lenting, O. D. Christophe, von Willebrand factor biosynthesis , secretion , and clearance : connecting the far ends. *Blood*. **125**, 2019–2029 (2016).
60. Y. F. Zhou, E. T. Eng, N. Nishida, C. Lu, T. Walz, A pH-regulated dimeric bouquet in the structure of von Willebrand factor. *EMBO*. **30**, 4098–4111 (2011).
61. L. A. Sporn, V. J. Marder, D. D. Wagner, Inducible secretion of large, biologically potent von Willebrand factor multimers. *Cell*. **46**, 185–190

(1986).

62. J. E. Sadler, Low von Willebrand factor: sometimes a risk factor and sometimes a disease. *Hematology Am. Soc. Hematol. Educ. Program*, 106–112 (2009).
63. F. Ferraro *et al.*, A two-tier golgi-based control of organelle size underpins the functional plasticity of endothelial cells. *Dev. Cell*. **29**, 292–304 (2014).
64. R.-H. Huang *et al.*, Assembly of Weibel-Palade body-like tubules from N-terminal domains of von Willebrand factor. *Proc. Natl. Acad. Sci. U. S. A.* **105**, 482–487 (2008).
65. J. E. Sadler, Biochemistry and Genetics of Von Willebrand Factor. *Annu. Rev. Biochem.* **67**, 395–424 (1998).
66. D. D. Wagner, T. Mayadas, M. Urban-Pickering, B. H. Lewis, V. J. Marder, Inhibition of disulfide bonding of von Willebrand protein by monensin results in small, functionally defective multimers. *J. Cell Biol.* **101**, 112–120 (1985).
67. G. Michaux *et al.*, The physiological function of von Willebrand's factor depends on its tubular storage in endothelial Weibel-Palade bodies. *Dev. Cell*. **10**, 223–232 (2006).
68. N. S. (LMCB/UCL), thesis (2013).
69. W. W. Y. Lui-Roberts, L. M. Collinson, L. J. Hewlett, G. Michaux, D. F. Cutler, An AP-1/clathrin coat plays a novel and essential role in forming the Weibel-Palade bodies of endothelial cells. *J. Cell Biol.* **170**, 627–636 (2005).
70. W. W. Y. Lui-Roberts, F. Ferraro, T. D. Nightingale, D. F. Cutler, Aftiphilin and gamma-synergin are required for secretagogue sensitivity of Weibel-Palade bodies in endothelial cells. *Mol. Biol. Cell*. **19**, 5072–81 (2008).
71. J.-B. Manneville *et al.*, Interaction of the actin cytoskeleton with microtubules regulates secretory organelle movement near the plasma membrane in human endothelial cells. *J. Cell Sci.* **116**, 3927–3938 (2003).
72. M. Erent *et al.*, Rate, extent and concentration dependence of histamine-evoked Weibel-Palade body exocytosis determined from individual fusion events in human endothelial cells. *J. Physiol.* **583**, 195–212 (2007).
73. K. M. Valentijn, J. E. Sadler, J. A. Valentijn, J. Voorberg, J. Eikenboom, Functional architecture of Weibel-Palade bodies. *Blood*. **117**, 5033–5043

(2011).

74. K. J. Harrison-Lavoie *et al.*, P-selectin and CD63 use different mechanisms for delivery to Weibel-Palade bodies. *Traffic*. **7**, 647–662 (2006).

75. M. Yamakuchi *et al.*, Antibody to human leukocyte antigen triggers endothelial exocytosis. *Proc. Natl. Acad. Sci. U. S. A.* **104**, 1301–1306 (2007).

76. U. Fiedler *et al.*, The Tie-2 ligand Angiopoietin-2 is stored in and rapidly released upon stimulation from endothelial cell Weibel-Palade bodies. *Blood*. **103**, 4150–4156 (2004).

77. C. V Denis, P. André, S. Saffaripour, D. D. Wagner, Defect in regulated secretion of P-selectin affects leukocyte recruitment in von Willebrand factor-deficient mice. *Proc. Natl. Acad. Sci. U. S. A.* **98**, 4072–7 (2001).

78. M. J. Hannah *et al.*, Weibel-Palade bodies recruit Rab27 by a content-driven, maturation-dependent mechanism that is independent of cell type. *J. Cell Sci.* **116**, 3939–3948 (2003).

79. D. Van Breevoort *et al.*, STXBP1 promotes Weibel-Palade body exocytosis through its interaction with the Rab27A effector Slp4-a. *Blood*. **123**, 3185–3194 (2014).

80. T. D. Nightingale, D. F. Cutler, L. P. Cramer, Actin coats and rings promote regulated exocytosis. *Trends Cell Biol.* **22**, 329–337 (2012).

81. T. D. Nightingale, K. Pattni, A. N. Hume, M. C. Seabra, D. F. Cutler, Rab27a and MyRIP regulate the amount and multimeric state of VWF released from endothelial cells. *Blood*. **113**, 5010–5018 (2009).

82. M. S. Pols, J. Klumperman, Trafficking and function of the tetrspanin CD63. *Exp. Cell Res.* **315**, 1584–1592 (2009).

83. S. J. Israels, E. M. McMillan-Ward, CD63 modulates spreading and tyrosine phosphorylation of platelets on immobilized fibrinogen. *Thromb. Haemost.* **93**, 311–318 (2005).

84. E. L. Doyle *et al.*, CD63 is an essential cofactor to leukocyte recruitment by endothelial P-selectin. *Blood*. **118**, 4265–4273 (2011).

85. A. T. Nurden, P. Nurden, Should any genetic defect affecting α-granules in platelets be classified as gray platelet syndrome? *Am. J. Hematol.* **91**, 714–718 (2016).

86. K. Mori *et al.*, Morphological changes of platelets during the process of platelet aggregation in gray platelet syndrome. *Tohoku J Exp Med*. **149**, 425–436 (1986).

87. K. Mori, S. Suzuki, K. Sugai, Electron microscopic and functional studies on platelets in gray platelet syndrome. *Tohoku J. Exp. Med.* **143**, 261–87 (1984).

88. J. G. White, Ultrastructural studies of the gray platelet syndrome. *Am. J. Pathol.* **95**, 445–62 (1979).

89. A. T. Nurden, P. Nurden, Inherited disorders of platelet function. *Platelets*. **13**, 1029–1050 (2007).

90. J. P. Rosa *et al.*, Gray platelet syndrome. Demonstration of alpha granule membranes that can fuse with the cell surface. *J. Clin. Invest.* **80**, 1138–1146 (1987).

91. C. Deppermann *et al.*, Gray platelet syndrome and defective thrombo-inflammation in Nbeal2-deficient mice. *J. Clin. Invest.* **123**, 3331–3342 (2013).

92. D. Urban *et al.*, The VPS33B-binding protein VPS16B is required in megakaryocyte and platelet ??-granule biogenesis. *Blood*. **120**, 5032–5040 (2012).

93. W. H. A. Kahr *et al.*, Abnormal megakaryocyte development and platelet function in Nbeal2-/- mice. *Blood*. **122**, 3349–58 (2013).

94. F. HERMANSKY, P. PUDLAK, Hermansky F, Pudlak P. Albinism associated with hemorrhagic diathesis and unusual pigmented reticular cells in the bone marrow: report of two cases with histochemical studies. Blood. 1959;14(2):162-169. *Blood*. **127**, 1731 (2016).

95. HPS network, (available at https://www.hpsnetwork.org/en/hps-information/characteristics).

96. J. Jung *et al.*, Identification of a homozygous deletion in the AP3B1 gene causing Hermansky-Pudlak syndrome, type 2. *Blood*. **108**, 362–369 (2006).

97. http://www.hpsnetwork.co.uk/misdiagnosis%20of%20hps%20and%20oca.html, (available at http://www.hpsnetwork.co.uk/misdiagnosis of hps

and oca.html).

98. L. Giannetti, The Misdiagnosis of a Rare Disease: The Journey to a Hermansky-Pudlak Syndrome Diagnosis (2014), (available at https://www.hpsnetwork.org/en/news/2014-12-11/results-from-road-to-diagnosis-hps-study-published).
99. M. Huizing, J. M. Parkes, A. Helip-Wooley, J. G. White, W. a Gahl, Platelet alpha granules in BLOC-2 and BLOC-3 subtypes of Hermansky-Pudlak syndrome. *Platelets*. **18**, 150–7 (2007).
100. S. Ammann *et al.*, Mutations in AP3D1 associated with immunodeficiency and seizures define a new type of Hermansky-Pudlak syndrome. *Blood*. **127**, 997–1006 (2016).
101. P. Jing, C. Schindler, J. Michal, B. Peter, Backlund and Juan S., Developmental Cell BORC , A Novel Multiprotein Complex that Regulates Lysosome Positioning. *Dev. Cell*. **33**, 176–188 (2015).
102. S. M. Wilson *et al.*, A mutation in Rab27a causes the vesicle transport defects observed in ashen mice. *Proc Natl Acad Sci U S A*. **97**, 7933–7938 (2000).
103. J. C. Detter *et al.*, Rab geranylgeranyl transferase alpha mutation in the gunmetal mouse reduces Rab prenylation and platelet synthesis. *Proc Natl Acad Sci U S A*. **97**, 4144–4149 (2000).
104. J. M. Falcón-Pérez, M. Starcevic, R. Gautam, E. C. Dell'Angelica, BLOC-1, a novel complex containing the pallidin and muted proteins involved in the biogenesis of melanosomes and platelet-dense granules. *J. Biol. Chem.* **277**, 28191–28199 (2002).
105. M. Starcevic, E. C. Dell'Angelica, Identification of Snapin and three novel proteins (BLOS1, BLOS2, and BLOS3/reduced pigmentation) as subunits of biogenesis of lysosome-related organelles complex-1 (BLOC-1). *J. Biol. Chem.* **279**, 28393–28401 (2004).
106. K. Moriyama, J. S. Bonifacino, Pallidin is a component of a multi-protein complex involved in the biogenesis of lysosome-related organelles. *Traffic*. **3**, 666–677 (2002).
107. H. H. Lee *et al.*, Assembly and architecture of Biogenesis of Lysosome-related Organelles Complex-1 (BLOC-1). *J. Biol. Chem.* **287**, 5882–5890

(2012).

108. A. T. J. Peter *et al.*, The BLOC-1 complex promotes endosomal maturation by recruiting the Rab5 gtpase-activating protein Msb3. *J. Cell Biol.* **201**, 97–111 (2013).
109. I. A. Rodriguez-Fernandez, E. C. Dell'Angelica, A data-mining approach to rank candidate protein-binding partners - The case of biogenesis of lysosome-related organelles complex-1 (BLOC-1). *J. Inherit. Metab. Dis.* **32**, 190–203 (2009).
110. E. C. Dell'Angelica, The building BLOC(k)s of lysosomes and related organelles. *Curr. Opin. Cell Biol.* **16**, 458–464 (2004).
111. S. M. Di Pietro, BLOC-1 Interacts with BLOC-2 and the AP-3 Complex to Facilitate Protein Trafficking on Endosomes. *Mol. Biol. Cell*. **17**, 4027–4038 (2006).
112. A. Chapel *et al.*, An Extended Proteome Map of the Lysosomal Membrane Reveals Novel Potential Transporters. *Mol. Cell. Proteomics*. **12**, 1572–1588 (2013).
113. S. R. G. Setty *et al.*, BLOC-1 Is Required for Cargo-specific Sorting from Vacuolar Early Endosomes toward Lysosome-related Organelles. *Mol. Biol. Cell*. **18**, 768–780 (2007).
114. G. Salazar, BLOC-1 Complex Deficiency Alters the Targeting of Adaptor Protein Complex-3 Cargoes. *Mol. Biol. Cell*. **17**, 4014–4026 (2006).
115. M. K. Dennis *et al.*, BLOC-2 targets recycling endosomal tubules to melanosomes for cargo delivery. *J. Cell Biol.* **209**, 563–577 (2015).
116. Y. Zhou *et al.*, Chitinase 3-like-1 and its receptors in Hermansky-Pudlak syndrome-associated lung disease. *J. Clin. Invest.* **125**, 3178–3192 (2015).
117. Q. Zhang *et al.*, Ru2 and Ru encode mouse orthologs of the genes mutated in human Hermansky-Pudlak syndrome types 5 and 6. *Nat. Genet.* **33**, 145–53 (2003).
118. A. Helip-Wooley *et al.*, Association of the Hermansky-Pudlak syndrome type-3 protein with clathrin. *BMC Cell Biol.* **6**, 33 (2005).
119. J. J. Bultema, A. L. Ambrosio, C. L. Burek, S. M. Di Pietro, BLOC-2, AP-3, and AP-1 proteins function in concert with Rab38 and Rab32 proteins to mediate protein trafficking to lysosome-related organelles. *J. Biol. Chem.*

287, 19550–19563 (2012).

120. G. Salazar *et al.*, Hermansky-pudlak syndrome protein complexes associate with phosphatidylinositol 4-kinase type II ?? in neuronal and non-neuronal cells. *J. Biol. Chem.* **284**, 1790–1802 (2009).
121. J. A. Martina, K. Moriyama, J. S. Bonifacino, BLOC-3, a protein complex containing the Hermansky-Pudlak syndrome gene products HPS1 and HPS4. *J. Biol. Chem.* **278**, 29376–29384 (2003).
122. A. L. Ambrosio, J. A. Boyle, S. M. Di Pietro, Mechanism of platelet dense granule biogenesis: Study of cargo transport and function of Rab32 and Rab38 in a model system. *Blood*. **120**, 4072–4081 (2012).
123. A. Gerondopoulos, L. Langemeyer, J. R. Liang, A. Linford, F. A. Barr, BLOC-3 mutated in Hermansky-Pudlak syndrome is a Rab32/38 guanine nucleotide exchange factor. *Curr. Biol.* **22**, 2135–2139 (2012).
124. D. P. Kloer *et al.*, Assembly of the biogenesis of lysosome-related organelles complex-3 (BLOC-3) and its interaction with Rab9. *J. Biol. Chem.* **285**, 7794–7804 (2010).
125. S. Y. Park, X. Guo, Adaptor protein complexes and intracellular transport. *Biosci. Rep.* **34**, 381–390 (2014).
126. J. Hirst, C. Irving, G. H. H. Borner, Adaptor Protein Complexes AP-4 and AP-5: New Players in Endosomal Trafficking and Progressive Spastic Paraplegia. *Traffic*. **14**, 153–164 (2013).
127. E. C. Dell'Angelica, V. Shotelersuk, R. C. Aguilar, W. A. Gahl, J. S. Bonifacino, Altered trafficking of lysosomal proteins in Hermansky-Pudlak syndrome due to mutations in the ??3A subunit of the AP-3 adaptor. *Mol. Cell*. **3**, 11–21 (1999).
128. G. W. Shotelersuk V, Dell'Angelica EC, Hartnell L, Bonifacino JS, A new variant of Hermansky-Pudlak syndrome due to mutations in a gene responsible for vesicle formation. *Am. J. Med.* **108**, 423–427 (2000).
129. A. A. Peden *et al.*, Localization of the AP-3 adaptor complex defines a novel endosomal exit site for lysosomal membrane proteins. *J. Cell Biol.* **164**, 1065–1076 (2004).
130. S. Kook *et al.*, Impaired lysosomal integral membrane protein 2-dependent peroxiredoxin 6 delivery to lamellar bodies accounts for altered alveolar

phospholipid content in adaptor protein-3-deficient pearl mice. *J. Biol. Chem.* **291**, 8414–8427 (2016).

131. U. M. Vischer, D. D. Wagner, CD63 is a component of Weibel-Palade bodies of human endothelial cells. *Blood*. **82**, 1184–1191 (1993).
132. D. Chen, J. Guo, T. Miki, M. Tachibana, W. a Gahl, Molecular cloning and characterization of rab27a and rab27b, novel human rab proteins shared by melanocytes and platelets. *Biochem. Mol. Med.* **60**, 27–37 (1997).
133. M. C. Seabra, Y. K. Ho, J. S. Anant, Deficient geranylgeranylation of Ram/Rab27 in choroideremia. *J. Biol. Chem.* **270**, 24420–24427 (1995).
134. J. C. Stinchcombe *et al.*, Rab27a is required for regulated secretion in cytotoxic T lymphocytes. *J. Cell Biol.* **152**, 825–833 (2001).
135. G. Griffiths, What's special about secretory lysosomes? *Semin. Cell Dev. Biol.* **13**, 279–284 (2002).
136. M. C. Seabra, E. H. Mules, A. N. Hume, Rab GTPases, intracellular traffic and disease. *Trends Mol. Med.* **8**, 23–30 (2002).
137. M. Fukuda, E. Kanno, C. Saegusa, Y. Ogata, T. S. Kuroda, Slp4-a/granuphilin-a regulates dense-core vesicle exocytosis in PC12 cells. *J. Biol. Chem.* **277**, 39673–39678 (2002).
138. Z. Yi *et al.*, The Rab27a / Granuphilin Complex Regulates the Exocytosis of Insulin-Containing Dense-Core Granules The Rab27a / Granuphilin Complex Regulates the Exocytosis of Insulin-Containing Dense-Core Granules. *Mol. Cell. Biol.* **6**, 1858–1867 (2002).
139. S. Zhao, S. Torii, H. Yokota-Hashimoto, T. Takeuchi, T. Izumi, Involvement of Rab27b in the regulated secretion of pituitary hormones. *Endocrinology*. **143**, 1817–1824 (2002).
140. E. K. Novak *et al.*, The regulation of platelet-dense granules by Rab27a in the ashen mouse, a model of Hermansky-Pudlak and Griscelli syndromes, is granule-specific and dependent on genetic background. *Blood*. **100**, 128–135 (2002).
141. Y. Hou, S. A. Ernst, E. L. Stuenkel, S. I. Lentz, J. A. Williams, Rab27A is present in mouse pancreatic acinar cells and is required for digestive enzyme secretion. *PLoS One*. **10**, e0125596 (2015).
142. E. K. Novak *et al.*, Inherited thrombocytopenia caused by reduced platelet

production in mice with the gunmetal pigment gene mutation. *Blood*. **85**, 1781–9 (1995).

143. R. T. Swank *et al.*, Inherited abnormalities in platelet organelles and platelet formation and associated altered expression of low molecular weight guanosine triphosphate-binding proteins in the mouse pigment mutant gunmetal. *Blood*. **81**, 2626–2635 (1993).
144. E. Abbe, Beiträge zur Theorie des Mikroskops und der mikroskopischen Wahrnehmung: I. Die Construction von Mikroskopen auf Grund der Theorie. *Arch. für mikroskopische Anat.* **9**, 413–418 (1873).
145. B. Huang, M. Bates, X. Zhuang, Super-Resolution Fluorescence Microscopy. *Annu. Rev. Biochem.* **78**, 993–1016 (2009).
146. T. a Klar, E. Engel, S. W. Hell, Breaking Abbe's diffraction resolution limit in fluorescence microscopy with stimulated emission depletion beams of various shapes. *Phys. Rev.* **64**, 66613 (2001).
147. M. G. L. Gustafsson, Surpassing the lateral resolution limit by a factor of two using structured illumination microscopy. *J. Microsc.* **198**, 82–87 (2000).
148. E. Betzig *et al.*, Imaging intracellular fluorescent proteins at nanometer resolution. *Science*. **313**, 1642–5 (2006).
149. S. T. Hess, T. P. K. Girirajan, M. D. Mason, Ultra-High Resolution Imaging by Fluorescence Photoactivation Localization Microscopy. *Biophys. J.* **91**, 4258–4272 (2006).
150. M. J. Rust, M. Bates, X. W. Zhuang, Sub-diffraction-limit imaging by stochastic optical reconstruction microscopy (STORM). *Nat Methods*. **3**, 793–795 (2006).
151. S. van de Linde *et al.*, Direct stochastic optical reconstruction microscopy with standard fluorescent probes. *Nat. Protoc.* **6**, 991–1009 (2011).
152. Super Resolution Imaging (2011) (available at http://www.super-resolution.biozentrum.uni-wuerzburg.de/research_topics/super_resolution_imaging/).
153. S. F. Imaging, C. Structures, C. Fluorophores, Super-Resolution Fluorescence Imaging of Cellular Structures and Dynamics with Conventional Fluorophores. *Imaging Microsc.* (2010), pp. 6–9.

154. M. G. L. Gustafsson *et al.*, Three-dimensional resolution doubling in wide-field fluorescence microscopy by structured illumination. *Biophys. J.* **94**, 4957–4970 (2008).
155. M. Heilemann, Fluorescence microscopy beyond the diffraction limit. *J. Biotechnol.* **149**, 243–251 (2010).
156. S. Cox, G. E. Jones, Imaging cells at the nanoscale. *Int. J. Biochem. Cell Biol.* **45**, 1669–1678 (2013).
157. D. J. Metcalf, R. Edwards, N. Kumarswami, A. E. Knight, Test samples for optimizing STORM super-resolution microscopy. *J. Vis. Exp.* **79**, e50579 (2013).
158. The Lasers Analytic Group Resource, (available at http://laser.ceb.cam.ac.uk/research/resources).
159. E. J. Rees *et al.*, Blind assessment of localisation microscope image resolution. *Opt. Nanoscopy*. **1**, 12 (2012).
160. M. Shaw, L. Zajiczek, K. O'Holleran, High speed structured illumination microscopy in optically thick samples. *Methods*. **88**, 11–19 (2015).
161. K. O'Holleran, M. Shaw, Optimized approaches for optical sectioning and resolution enhancement in 2D structured illumination microscopy. *Biomed. Opt. Express*. **5**, 2580 (2014).
162. C. P. M. Hayward *et al.*, Results of an external proficiency testing exercise on platelet dense-granule deficiency testing by whole mount electron microscopy. *Am. J. Clin. Pathol.* **131**, 671–675 (2009).
163. M. Lopes da Silva *et al.*, Type II PI4-kinases control Weibel-Palade body biogenesis and von Willebrand factor structure in human endothelial cells. *J. Cell Sci.* **129**, 2096–2105 (2016).
164. W. Grimes, thesis (2016).
165. S. R. Sternberg, Biomedical Image Processing. *Computer (Long. Beach. Calif).* **16** (1983), pp. 22–34.
166. J. Kittler, J. Illingworth, Minimum error thresholding - Kittler, Illingworth.pdf. *Pattern Recognit.* **19**, 41–47 (1986).
167. H. Christensen, W. H. A. Kahr, in *Diagnostic Electron Microscopy - A Practical Guide to Interpretation and Technique* (John Wiley & Sons, Ltd, 2013; http://dx.doi.org/10.1002/9781118452813.ch10), pp. 277–291.

168. M.-J. Kraus, H. Neeb, E. F. Strasser, Fractal and Euclidean descriptors of platelet shape. *Platelets*. **7104**, 1–11 (2013).
169. DuPont, in *International immunology*, L. O'Gorman, R. Kasturi, Eds. (IEEE Computer Society Press, Los Alamitos, CA, USA, 2014; http://www.ncbi.nlm.nih.gov/pubmed/24591353), vol. 26, p. NP.
170. P. Baggethun, Radial Profile Plot (2010), p. 2010.
171. S. V Costes *et al.*, Automatic and quantitative measurement of protein-protein colocalization in live cells. *Biophys. J.* **86**, 3993–4003 (2004).
172. K. J. Livak, T. D. Schmittgen, Analysis of relative gene expression data using real-time quantitative PCR and. *Methods*. **25**, 402–408 (2001).
173. G. J. Howell *et al.*, Endothelial cell confluence regulates Weibel-Palade body formation. *Mol. Membr. Biol.* **21**, 413–421 (2004).
174. Ensembl, (available at http://www.ensembl.org/index.html).
175. siRNA check, (available at http://projects.insilico.us/SpliceCenter/ArrayCheck.jsp).
176. J. P. Luzio, Y. Hackmann, N. M. G. Dieckmann, G. M. Griffiths, The biogenesis of lysosomes and lysosome-related organelles. *Cold Spring Harb. Perspect. Biol.* **6**, a016840 (2014).
177. D. F. Cutler, Introduction: lysosome-related organelles. *Semin. Cell Dev. Biol.* **13**, 261–262 (2002).
178. S. M. Di Pietro, E. C. Dell'Angelica, The cell biology of Hermansky-Pudlak syndrome: recent advances. *Traffic*. **6**, 525–33 (2005).
179. M. Huizing *et al.*, AP-3 mediates tyrosinase but not TRP-1 trafficking in human melanocytes. *Mol. Biol. Cell*. **12**, 2075–85 (2001).
180. A. R. Mantegazza *et al.*, Adaptor Protein-3 in Dendritic Cells Facilitates Phagosomal Toll-like Receptor Signaling and Antigen Presentation to CD4+ T Cells. *Immunity*. **36**, 782–794 (2012).
181. M. Sasai, M. M. Linehan, A. Iwasaki, Bifurcation of Toll-like receptor 9 signaling by adaptor protein 3. *Science*. **329**, 1530–4 (2010).
182. R. Meng *et al.*, SLC35D3 delivery from megakaryocyte early endosomes is required for platelet dense granule biogenesis and is differentially defective in Hermansky-Pudlak syndrome models. *Blood*. **120**, 404–414 (2012).

183. E. C. Dell'Angelica *et al.*, Molecular characterization of the protein encoded by the Hermansky-Pudlak syndrome type 1 gene. *J. Biol. Chem.* **275**, 1300–1306 (2000).
184. Albinism.org, (available at http://www.albinism.org/site/c.flKYIdOUIhJ4H/b.9260373/k.72A9/HermanskyPudlak_Syndrome.htm).
185. G. D'Andrea, M. Chetta, M. Margaglione, Inherited platelet disorders: Thrombocytopenias and thrombocytopathies. *Blood Transfus.* **7**, 278–292 (2009).
186. A. Delprato, S. Raghavan, T. A. Lyerla, An established light ear mutant (C57BL/6J-Pdeb(rd1) le) mouse cell line exhibits a block to secretion of lysosomal enzymes. *Exp. Cell Res.* **256**, 315–320 (2000).
187. E. K. Novak, S. W. Hui, R. T. Swank, Platelet storage pool deficiency in mouse pigment mutations associated with seven distinct genetic loci. *Blood*. **63**, 536–44 (1984).
188. S. H. Guttentag *et al.*, Defective surfactant secretion in a mouse model of Hermansky-Pudlak syndrome. *Am. J. Respir. Cell Mol. Biol.* **33**, 14–21 (2005).
189. R. H. Clark *et al.*, Adaptor protein 3-dependent microtubule-mediated movement of lytic granules to the immunological synapse. *Nat. Immunol.* **4**, 1111–1120 (2003).
190. A. R. Cullinane *et al.*, A BLOC-1 mutation screen reveals that PLDN is mutated in hermansky-pudlak syndrome type 9. *Am. J. Hum. Genet.* **88**, 778–787 (2011).
191. L. Huang, Y. M. Kuo, J. Gitschier, The pallid gene encodes a novel, syntaxin 13-interacting protein involved in platelet storage pool deficiency. *Nat. Genet.* **23**, 329–32 (1999).
192. R. Prekeris, J. Klumperman, Y. A. Chen, R. H. Scheller, Syntaxin 13 mediates cycling of plasma membrane proteins via tubulovesicular recycling endosomes. *J. Cell Biol.* **143**, 957–971 (1998).
193. M. J. Kean *et al.*, VAMP3, syntaxin-13 and SNAP23 are involved in secretion of matrix metalloproteinases, degradation of the extracellular matrix and cell invasion. *J. Cell Sci.* **122**, 4089–4098 (2009).

194. C. Wasmeier *et al.*, Rab38 and Rab32 control post-Golgi trafficking of melanogenic enzymes. *J. Cell Biol.* **175**, 271–281 (2006).
195. V. S. Lopes, C. Wasmeier, M. C. Seabra, C. E. Futter, Melanosome maturation defect in Rab38-deficient retinal pigment epithelium results in instability of immature melanosomes during transient melanogenesis. *Mol. Biol. Cell*. **18**, 3914–3927 (2007).
196. K. Osanai *et al.*, Altered lung surfactant system in a Rab38-deficient rat model of Hermansky-Pudlak syndrome. *Am. J. Physiol. Lung Cell. Mol. Physiol.* **298**, 243–51 (2010).
197. J. J. Bultema *et al.*, Myosin Vc interacts with Rab32 and Rab38 proteins and works in the biogenesis and secretion of melanosomes. *J. Biol. Chem.* **289**, 33513–33528 (2014).
198. M. K. Dennis *et al.*, BLOC-1 and BLOC-3 regulate VAMP7 cycling to and from melanosomes via distinct tubular transport carriers. *J. Cell Biol.* **214**, 293–308 (2016).
199. F. Ferraro *et al.*, Weibel-Palade body size modulates the adhesive activity of its von Willebrand Factor cargo in cultured endothelial cells. *Sci. Rep.* **6**, 32473 (2016).
200. a B. Federici *et al.*, Binding of von Willebrand factor to glycoproteins Ib and IIb/IIIa complex: affinity is related to multimeric size. *Br. J. Haematol.* **73**, 93–99 (1989).
201. A. Vincentelli *et al.*, Acquired von Willebrand Syndrome in Aortic Stenosis. *N. Engl. J. Med.* **349**, 343–349 (2003).
202. W. Gola, M. Lelonek, Clinical implication of gastrointestinal bleeding in degenerative aortic stenosis: An update. *Cardiol. J.* **17** (2010), pp. 330–334.
203. T. E. Warkentin, D. G. Morgan, J. C. Moore, Aortic stenosis and bleeding gastrointestinal angiodysplasia: is acquired von Willebrand's disease the link? *Lancet*. **340**, 35–37 (1992).
204. G. Michaux *et al.*, Analysis of intracellular storage and regulated secretion of 3 von Willebrand disease-causing variants of von Willebrand factor. *Blood*. **102**, 2452–2458 (2003).
205. P. Howlin, A continuing journey. *Psychologist*. **27**, 796–798 (2014).
206. K. M. Valentijn *et al.*, Multigranular exocytosis of Weibel-Palade bodies in

vascular endothelial cells. *Blood*. **116**, 1807–1816 (2010).

207. T. D. Nightingale *et al.*, Actomyosin II contractility expels von Willebrand factor from Weibel-Palade bodies during exocytosis. *J. Cell Biol.* **194**, 613–629 (2011).
208. D. R. Caffrey *et al.*, Sirna off-target effects can be reduced at concentrations that match their individual potency. *PLoS One*. **6** (2011), doi:10.1371/journal.pone.0021503.
209. L. Ramsay *et al.*, A simple sequence repeat-based linkage map of Barley. *Genetics*. **156**, 1997–2005 (2000).
210. M. L. Ormiston *et al.*, Generation and Culture of Blood Outgrowth Endothelial Cells from Human Peripheral Blood. *J. Vis. Exp.*, e53384 (2015).
211. A. Sharda *et al.*, Defective PDI release from platelets and endothelial cells impairs thrombus formation in Hermansky-Pudlak syndrome. *Blood*. **125**, 1633–1642 (2015).
212. J. Kamykowski, P. Carlton, S. Sehgal, B. Storrie, Quantitative immunofluorescence mapping reveals little functional coclustering of proteins within platelet ??-granules. *Blood*. **118**, 1370–1373 (2011).
213. H. Heijnen, P. van der Sluijs, Platelet secretory behaviour: As diverse as the granules... or not? *J. Thromb. Haemost.* **13**, 2141–2151 (2015).
214. S. Sehgal, B. Storrie, Evidence that differential packaging of the major platelet granule proteins von Willebrand factor and fibrinogen can support their differential release. *J. Thromb. Haemost.* **5**, 2009–2016 (2007).
215. A. McNicol, S. J. Israels, Platelet dense granules: Structure, function and implications for haemostasis. *Thromb. Res.* **95**, 1–18 (1999).
216. R. J. Skaer, R. J. Flemans, S. McQuilkan, Mepacrine stains the dense bodies of human platelets and not platelet lysosomes. *Br. J. Haematol.* **49**, 435–8 (1981).
217. T. Youssefian, J.-M. Massé, F. Rendu, J. Guichard, E. M. Cramer, Platelet and Megakaryocyte Dense Granules Contain Glycoproteins Ib and IIb-IIIa. *Blood*. **89**, 4047–4057 (1997).
218. M. L. Jones, M. T. Harper, E. W. Aitken, C. M. Williams, A. W. Poole, RGD-ligand mimetic antagonists of integrin αIIbβ3 paradoxically enhance GPVI-induced human platelet activation. *J. Thromb. Haemost.* **8**, 567–576 (2010).

219. J. G. White, Use of the electron microscope for diagnosis of platelet disorders. *Semin. Thromb. Hemost.* **24**, 163–168 (1998).
220. N. Dovlatova *et al.*, Evaluation of a whole blood remote platelet function test for the diagnosis of mild bleeding disorders. *J. Thromb. Haemost.* **12**, 660–665 (2014).
221. P. Rubak, P. H. Nissen, S. D. Kristensen, A. M. Hvas, Investigation of platelet function and platelet disorders using flow cytometry. *Platelets*. **7104**, 1–9 (2015).
222. G. V. R. Born, Aggregation of blood platelets by adenosine diphosphate and its reversal. *Nature*. **194**, 927–929 (1962).
223. J. R. O'BRIEN, The adhesiveness of native platelets and its prevention. *J. Clin. Pathol.* **14**, 140–9 (1961).
224. M. Cattaneo *et al.*, Recommendations for the standardization of light transmission aggregometry: A consensus of the working party from the platelet physiology subcommittee of SSC/ISTH. *J. Thromb. Haemost.* **11**, 1183–1189 (2013).
225. J. N. George, S. J. Shattil, The Clinical Importance of Acquired Abnormalities of Platelet Function. *N. Engl. J. Med.* **324**, 27–39 (1991).
226. R. E. Rumbaut, P. Thiagarajan, Platelet-Vessel Wall Interactions in Hemostasis and Thrombosis. *Colloq. Ser. Integr. Syst. Physiol. From Mol. to Funct.* **2**, 1–75 (2010).
227. N. Ji, H. Shroff, H. Zhong, E. Betzig, Advances in the speed and resolution of light microscopy. *Curr. Opin. Neurobiol.* **18**, 605–616 (2008).
228. B. Huang, Super-resolution optical microscopy: multiple choices. *Curr. Opin. Chem. Biol.* **14**, 10–14 (2010).
229. Electron Microscope of thin sections of a platelet, (available at http://www.medical-labs.net/gray-platelet-syndrome-gps-1256/electron-microscope-of-thin-sections-of-a-platelet/).
230. C. B. Uhl *et al.*, Platelet Storage Pool Deficiency: Establishment Of Reference Ranges For Platelet Dense Granule Count By Transmission Electron Microscopy. *Blood*. **122**, 3549 (2013).
231. C. Dunois-Lardé *et al.*, Exposure of human megakaryocytes to high shear rates accelerates platelet production. *Blood*. **114**, 1875–1883 (2009).

232. J. M. Gerrard *et al.*, Identification of a platelet dense granule membrane protein that is deficient in a patient with the Hermansky-Pudlak syndrome. *Blood*. **77**, 101–112 (1991).
233. B. Storrie, Defective platelet autocrine signaling in HPS. *Blood*. **125**, 1515–1516 (2015).
234. K. W. Dunn, M. M. Kamocka, J. H. McDonald, A practical guide to evaluating colocalization in biological microscopy. *AJP Cell Physiol.* **300**, C723–C742 (2011).
235. D. Westmoreland *et al.*, Super-resolution microscopy as a potential approach to diagnosis of platelet granule disorders. *J. Thromb. Haemost.* **14**, 839–849 (2016).

****